



University
of Glasgow

Pajak, Malgorzata Zofia (2016) *Investigation of 18F-Fluoro-L-Thymidine to monitor treatment response in murine models of pancreatic cancer: development of tools and validation*. PhD thesis.

<http://theses.gla.ac.uk/8023/>

Copyright and moral rights for this work are retained by the author

A copy can be downloaded for personal non-commercial research or study, without prior permission or charge

This work cannot be reproduced or quoted extensively from without first obtaining permission in writing from the author

The content must not be changed in any way or sold commercially in any format or medium without the formal permission of the author

When referring to this work, full bibliographic details including the author, title, awarding institution and date of the thesis must be given

Glasgow Theses Service

<http://theses.gla.ac.uk/>

theses@gla.ac.uk



University of Glasgow | College of Medical,
Veterinary & Life Sciences

Investigation of ^{18}F -Fluoro-L-Thymidine to Monitor Treatment Response in Murine Models of Pancreatic Cancer; Development of Tools and Validation

Malgorzata Zofia Pajak

B.Sc.

Submitted in the fulfilment of the requirements for the Degree of Doctor
of Philosophy at the College of Medical, Veterinary & Life Sciences,
University of Glasgow

College of Medical, Veterinary & Life Sciences

University of Glasgow

September 2016

Abstract

I characterised performance of the Positron Emission Tomography (PET) and the Computed Tomography (CT) modules of the 2-ring Albira PET/SPECT/CT, a small-animal imaging platform. The evaluation of PET was done in concordance with the National Electrical Manufacturer's Association (NEMA) NU4-2008 standard. The performance of the Albira CT was assessed using microCT phantom. As a way of verification of the results of the phantom studies, example images from the tri-modal PET/SPECT/CT experiment were analysed. Additionally, gamma counter was evaluated as a tool for measuring biodistribution of the radiolabelled probes *ex vivo*.

¹⁸F-Fluoro-L-Thymidine (¹⁸F-FLT) was used in the investigation of the treatment response in the mouse models of pancreatic ductal adenocarcinoma (PDAC). Results from the two studies using mTOR and TGF β inhibitors are reported. The mTOR inhibitor, rapamycin used ¹⁸F-FLT in the PET imaging to study, which aimed to compare the effects of the treatment on proliferation in two mouse models recapitulating the features of human PDAC, namely the KC Pten and KPC. TGF β inhibitor study characterised the acute impact the administered TGF β antibody has on proliferation in KPC mice in addition and as opposed to gemcitabine monotherapy, which is currently considered a golden standard in the treatment of pancreatic cancer. This study utilized gamma counting, autoradiography and Ki67 immunohistochemistry (IHC).

Table of Contents

PART I: PERFORMANCE EVALUATION of SMALL ANIMAL PET SCANNERS

1	Introduction	20
1.1	<i>NEMA Standard as an Assessment of PET</i>	20
1.2	<i>Performance of Other Modalities</i>	22
1.2.1	NEMA Standards for Other Modalities	22
1.2.2	Performance Testing	24
1.3	<i>Bruker Albira PET/SPECT/CT</i>	25
1.3.1	Landscape of Pre-clinical Tri-modal (PET/SPEC/CT) Scanners	25
1.3.2	Albira Features	26
1.3.2.1	PET	26
1.3.2.2	SPECT	30
1.3.2.3	CT	30
1.3.2.4	Animal Handling and Monitoring	32
1.3.2.5	Software	32
1.3.2.6	List-mode format	32
2	Aims and Objectives	34
2.1	<i>PET</i>	34
2.2	<i>CT</i>	35
3	Methods	36
3.1	<i>NEMA NU4-2008</i>	36
3.1.1	Spatial Resolution	36
3.1.1.1	Measurements	36
3.1.1.2	Data processing and analysis	37
3.1.2	Sensitivity	38
3.1.2.1	Measurements	38
3.1.2.2	Data processing and analysis	38
3.1.3	Count-rate Performance	40
3.1.3.1	Measurements	40

3.1.3.2	Data processing and analysis	41
3.1.4	Image Quality	43
3.1.4.1	Measurements	43
3.1.4.2	Data processing and analysis	44
3.1.5	Computation	46
3.1.5.1	Geometry transformation for sinogram generation	46
3.1.5.2	Sensitivity and count-rate performance calculations	48
3.2	<i>Assessment of CT</i>	48
3.2.1	Measurements	48
3.2.2	Data Processing and Analysis	51
3.3	<i>Basic Animal Studies</i>	52
3.3.1	Dual-tracer Bone Imaging Study	52
3.3.2	Data Processing and Analysis	53
4	Results	55
4.1	<i>NEMA Results for Albira PET</i>	55
4.1.1	Spatial Resolution	55
4.1.2	Sensitivity	59
4.1.3	Count-rate Performance	60
4.1.4	Image Quality	61
4.2	<i>CT Phantom Results</i>	63
4.2.1	Stability of the System and Basic Performance	63
4.2.2	Impact of Acquisition Settings on Image Quality	68
4.2.3	Impact of Reconstruction Settings on Image Quality	70
4.2.4	Example Animal Images	73
4.3	<i>Basic Animal Studies</i>	77
5	Discussion	80
5.1	<i>Performance Evaluation of 2-ring Albira PET</i>	80
5.1.1	NEMA NU4-2008 Overview	80
5.1.2	2-ring Albira PET vs. other small-animal PETs and 1- and 3-ring Albira PET	82
5.1.3	2-ring Albira PET vs. other tri-modal PET/SPECT/CT scanners	84

5.1.4 Albira PET vs. MAMMI PET	85
5.1.5 Albira PET Improvements	86
5.2 Albira CT Performance and Quality Assurance	87
5.3 PET/CT quality control	90
5.4 Multi-modal Animal Studies	92

PART II: USING ¹⁸F-FLT AND POSITRON EMISSION TOMOGRAPHY IN MONITORING TREATMENT RESPONSE IN MURINE PANCREATIC CANCER MODELS

6 Introduction	96
6.1 Anatomy, Morphology and Role of the Pancreas	96
6.2 Differences between Human and Murine Pancreas	97
6.3 Overview and Statistics for Pancreatic Cancer in UK	97
6.3.1 Types of Pancreatic Cancer and Epidemiology	97
6.3.2 Risk Factors	98
6.3.3 Clinical Signs and Symptoms	100
6.3.4 Diagnosis and clinical classification	101
6.3.5 Statistics for UK	102
6.4 Genetic Background of Pancreatic Ductal Adenocarcinoma	104
6.4.1 Mutated Genes and Pathways	104
6.4.2 Mouse Models of Pancreatic Ductal Adenocarcinoma	105
6.4.2.1 Rationale for Using Murine Models	105
6.4.2.2 KPC	106
6.4.2.3 KC Pten	107
6.4.2.4 Disease Onset, Clinical Signs and Necropsy Findings in Mouse Models	107
6.5 Current Treatment of Pancreatic Cancer	108
6.5.1 Potentially Curative Resection	109
6.5.1.1 Neoadjuvant and Adjuvant Treatment	110
6.5.2 Ablative or Embolization Therapy	110
6.5.3 Radiation Therapy	111
6.5.4 Palliative Treatment	112

6.5.5	Chemo- and Immunotherapy	112
6.5.5.1	Standard Treatment	112
6.5.5.2	Immunotherapy	113
6.5.5.3	Clinical Trials	114
6.6	TGF β	114
6.7	^{18}F -FLT	115
6.8	Research Questions	115
7	Aims and objectives	117
7.1	mTOR Inhibitor study	117
7.2	TGF β Study	117
8	Methods	118
8.1	mTOR Inhibitor Study	118
8.1.1	Study Design	118
8.1.2	Treatment Regime and Sampling	118
8.1.3	PET/CT Protocol	118
8.1.4	Data Analysis	119
8.2	Gamma counter experiments	120
8.2.1	Calibration	120
8.2.2	Sample volume experiment	120
8.3	TGF β Antibody	121
8.3.1	Study Design	121
8.3.2	Treatment Regime	122
8.3.3	Gamma Counting	123
8.3.4	Autoradiography	125
8.3.5	Ki67	128
8.3.6	Normalization	130
8.3.7	Statistical Data Analysis	130
9	Results	132
9.1	mTOR Inhibitor Study	132

9.2	<i>Gamma counter Calibration</i>	138
9.2.1	Calibration	138
9.2.2	Sample volume	139
9.3	<i>TGFβ Antibody Study</i>	140
9.3.1	Gross Anatomy	140
9.3.2	Autoradiography	149
9.3.3	Ki67	150
10	Discussion	156
10.1	<i>mTOR</i>	156
10.2	<i>Gamma Counter Experiments</i>	161
10.3	<i>TGFβ</i>	163
11	Conclusions	172
12	Appendix	173
13	References	174

List of figures

Figure 1 Bruker Albira PET/SPECT/CT _____	27
Figure 2 Side view of the two adjacent rings in Albira PET _____	27
Figure 3 Schematic diagram showing 2-ring Albira PET detector arrangement _	28
Figure 4 Deep Dose Equivalent as a function of time in Albira CT _____	31
Figure 5 Example output of the <i>ImViewer</i> _____	33
Figure 6 Schematic picture showing the ^{22}Na point-source _____	36
Figure 7 Definition of FWHM and FWTM _____	38
Figure 8 Schematic picture of CRP phantoms _____	40
Figure 9 Schematic picture of NEMA NU4 IQ phantom _____	44
Figure 10 A schematic picture of the micro-CT phantom _____	48
Figure 11 Timeline of the dual-radiotracer experiment _____	53
Figure 12 Images of a point source acquired by Albira _____	56
Figure 13 Spatial resolutions of the 2-ring Albira PET _____	57
Figure 14 Axial sensitivity profile of the 2-ring Albira PET _____	59
Figure 15 Count-rate performance of the 2-ring Bruker Albira PET _____	60
Figure 16 RCs for the 2-ring Albira PET vs number of MLEM iterations _____	62
Figure 17 SORs for the 2-ring Albira PET vs number of MLEM iterations _____	63
Figure 18 HUs for three current-voltage settings of Albira CT measured over three days using microCT phantom _____	65
Figure 19 HUs for all combinations of current-voltage settings of Albira CT measured over three days using microCT phantom _____	66

Figure 20 Spatial resolution of Albira CT measured using microCT phantom	67
Figure 21 Images of microCT phantom acquired using all combinations of current-voltage & number of projections of Albira CT	69
Figure 22 Images of microCT phantom acquired using 1000 projections and four current-voltage settings, reconstructed using different voxel sizes	71
Figure 23 Images of microCT phantom acquired using 250 projections and four current-voltage settings, reconstructed using different voxel sizes	72
Figure 24 Image of a cadaver acquired using 600 projections, 0.4 mA & 35 kV, reconstructed using different voxel sizes	74
Figure 25 Image of a cadaver acquired using 600 projections, 0.4 mA & 45 kV, reconstructed using different voxel sizes	75
Figure 26 Image of a cadaver acquired using 600 projections, 0.4 mA & 45 kV, reconstructed using different voxel sizes	76
Figure 27 MIPs in dual-tracer experiment	78
Figure 28 Summary of the 90 min dynamic ^{18}F -NaF PET acquisition	79
Figure 29 TACs for the mouse injected with ^{18}F -NaF	79
Figure 30 Cobra II Gamma Counter	124
Figure 31 An example autoradiography film with ROIs drawn	127
Figure 32 CT image of a tumour-bearing KC Pten mouse	133
Figure 33 Fused ^{18}F -FLT PET/CT image of a tumour-bearing KC Pten mouse	134
Figure 34 ^{18}F -FLT TACs for liver and tumour measured over 3h	135
Figure 35 PET/CT image of KC Pten mouse pre- and post- rapamacin	136
Figure 36 H&E staining of PDAC tumours pre- and post-rapamacin	136
Figure 37 Ki67 staining of PDAC tumours pre- and post-rapamacin	137

Figure 38 Tumour uptake of ^{18}F -FLT pre- and post-rapamacin for KPC and KC Pten mice_____	137
Figure 39 Gamma counter calibration curve _____	138
Figure 40 Sample volume vs. counts measured by the gamma counter_____	139
Figure 41 The ratio of counts in the energy window of 15 to 2000 keV to those in 311 to 711 keV depending on the volume of the sample_____	140
Figure 42 Large pancreatic cyst _____	141
Figure 43 Blocked bile duct_____	141
Figure 44 Tumour encapsulating enlarged spleen_____	142
Figure 45 Blocked bile duct and macroscopic liver metastases _____	142
Figure 46 Tumour cells blocking part of the duodenum _____	143
Figure 47 Biodistribution of ^{18}F -FLT and its metabolites 2h post-injection. ____	144
Figure 48 Ki67 expression: liver metastasis_____	150
Figure 49 Ki67 expression: large intestine_____	151
Figure 50 Ki67 expression: small intestine _____	151
Figure 51 Ki67 expression: PDAC tumour showing desmoplasia _____	152
Figure 52 Ki67 expression: untreated advanced PDAC tumour _____	152
Figure 53 Example output data of the automatic Tissue IA tool. _____	153
Figure 54 Summary of the acute effects of anti-TGFB on KPC mice _____	155

List of Tables

Table 1 List of the NEMA Test Standards _____	22
Table 2 Summary of the aims of each part of NEMA NU4-2008 protocol _____	34
Table 3 Summary of all available detector pairs for the 2-ring Albira PET _____	47
Table 4 MicroCT phantom specification _____	49
Table 5 Details of the CT protocol _____	50
Table 6 Spatial resolution results using 20 iterations MLEM and FBP _____	58
Table 7 RCs measured using NEMA NU4 IQ phantom for the 2-ring Albira PET ____	61
Table 8 SORs measured using NEMA NU4 IQ phantom for the 2-ring Albira PET _	61
Table 9 Example HUs for different types of tissue, air and water _____	88
Table 10 Size of cohorts in each experimental groups and test carried out ____	122
Table 11 Avg. age & weight of the mouse and administered dose of ^{18}F -FLT ____	122
Table 12 Details of the Leica Tissue IA automatic scoring protocol _____	129
Table 13 Live _____	145
Table 14 PDAC _____	145
Table 15 Blood _____	145
Table 16 Brain _____	146
Table 17 Heart _____	146
Table 18 Kidney _____	146
Table 19 Large intestine _____	147
Table 20 Lungs _____	147

Table 21 Muscle_____	147
Table 22 Small intestine_____	148
Table 23 Spleen_____	148
Table 24 Stomach _____	148
Table 25 Liver _____	149
Table 26 PDAC _____	149
Table 27 Liver _____	154
Table 28 PDAC _____	154

Acknowledgements

I would like to thank my supervisors, Prof. Kurt Anderson, Dr. Sally Pimlott and Dr. Jens Waldeck for putting up with me over the past four years. I'm aware that due to my challenging personal circumstances my postgraduate experience was rather not typical and a bumpy ride for us all. Without their patience and support I would have probably given up in the face of adversity. I owe a lot also to my research group, especially to Dr. Max Nobis, Dr. Juli Schwarz and Orchi Annanya, and my colleagues from BAIR, who helped at various stages of my biological project.

David Volgyes was a tremendous help in the NEMA part of my PhD project and I cannot thank him enough for it. I would like to acknowledge Dr. Antonio Soriano, Dr. Laura Moliner and Dr. Jose Maria Benlloch from I3M Institute and Carlos Correcher from Oncovision - all from Valencia, Spain, whom I learnt a lot from in terms of NEMA protocol and results analysis; Prof. W. Matthew Leevy and Sarah Chapman from Notre Dame University in the US deserve acknowledgement for their help with starting animal imaging using the Albira system.

I would like to extend my thanks to: Agata Mrowinska, who patiently taught me mouse dissection and assisted in the PET imaging in the mTOR inhibitor project; Tom Hamilton and Derek Miller, who trained me on other mouse procedures; Dr. Saadia Karim, who spent countless hours training me in KPC model; Dr. Jennifer Morton, who was a big source of fundamental knowledge about pancreatic cancer; Dr. Karen Blyth, who was always available to discuss mouse models; Viola Paulus-Hock, who shared her mice with me; Dr. Mike Olson and Dr. Jackie Beesley for their support in the last few months leading to the submission of this thesis.

Dr. Gerry Gillen, Clare McKeown and the rest of the team from West of Scotland PET Centre were vital in starting the Albira project and shared their expertise in clinical PET and nuclear imaging. I wouldn't be able to conduct my research without the help of Dr. Sue Champion, Dr. Jonathan Owens and their colleagues from the PET Radiopharmaceutical Production Unit in Gartnavel General Hospital in Glasgow, who synthesized the ^{18}F -FLT that I used; gentlemen from the

Beatson Stores, George Monteith, Michael McTaggart and Joe McFadden, who delivered ^{18}F -FLT and other radiopharmaceuticals whenever it was required.

My gratitude goes to Dr. Gaurav Malviya for his indispensable assistance in my TGFB experiments; Dr. Filip Zmuda for his help in the latter and all those many times, when I need a helping hand; Dr. Gabriela Kalna for conducting statistical analysis of my results from those experiments; Colin Nixon and Mark Hughes, and the rest of the Histology team for fast processing of my samples, staining and scanning of my slides.

My research couldn't take place without the support staff from BSU/BRU and Central Services in the CR UK: Beatson Institute. I would like also to acknowledge Robert McFarlane, Dr. Laura Bence and Richard Selkirk for making sure we all worked in safe environment.

I would like to acknowledge the financial support in the form of scholarship that was funded jointly by SINAPSE Collaboration (www.sinapse.ac.uk), a Pooling Initiative funded by the Scottish Funding Council and the Chief Scientist Office of the Scottish Executive, and Carestream/Bruker.

Two people, who deserve special acknowledgement, are Dr. Declan Diver and Prof. Andrew Smith, who both believed in me even when I did not believe in myself. Without their understanding and moral support, I may have given up just before the finish line.

In would like to thank my parents, Barbara and Ryszard, my two brothers, Adam and Michal and my cousin, Agnieszka for being proud of me long before I got to the conclusion of my studies; Aldona Michalska and Carol Ramsey for their compassion and gentle reminders that work is not everything; Piotr, Karo, Kasia, Kama, Filip and Ourania for their sympathetic ear, advice, a shoulder to cry on and generally - for keeping me sane; family Wierzbicki for looking after me in the last few weeks of the writing up process; my congregation, and finally and most of all to Jehovah God for giving me strength and perseverance to endure on this journey (*Philippians 4:13*).

*I would like to dedicate this thesis to the memory of two women,
who had profound impact on my life,
Malgorzata Sonntag and Aneta Michalska.*

Author's Declaration

This thesis represents original work of Malgorzata Zofia Pajak unless explicitly stated otherwise in the text. This thesis has not been submitted in any other form to any other University. Portions of the work described herein have been published elsewhere as listed below.

Signature: _____

Malgorzata Zofia Pajak

September 2016

List of papers:

Morran, Douglas C., Wu, Jianmin, Jamieson, Nigel B., Mrowinska, Agata, Kalna, Gabriela, Karim, Saadia A., Au, Amy Y. M., Scarlett, Christopher J., Chang, David K., Pajak, Malgorzata Z., *et al.* 2014. Targeting mTOR Dependency in Pancreatic Cancer. *Gut*, 63(9), pp. 1481-1490, DOI: 10.1136/gutjnl-2013-306202

Pajak, Malgorzata Z., Volgyes, David, Pimlott, Sally L., *et al.*, 2016. NEMA NU4-2008 Performance Evaluation of Albira: A Two-Ring Small-Animal PET System Using Continuous LYSO Crystals. *Open Medicine Journal*, 3, pp. 12-26, DOI: 10.2174/1874220301603010012

Abbreviations

APD	avalanche photodiode
CPU	computer processing unit
C_{r+s}	random and scattered counts
C_{TOT}	total coincidence counts
CT	(X-ray) computed tomography
GPU	graphics processing unit
HU	Hounsfield unit
FBP	filtered back-projection
FC	fold-change
FOV	field of view
FWHM	full width half maximum
FWTM	full width tenth maximum
IHC	immunohistochemistry
KC Pten	Pdx1-Cre; Kras ^{G12D} ; Pten ^{flox/flox}
KPC	Pdx1-Cre; Kras ^{G12D} ; Tp53 ^{R172H}
LGSO	lutetium gadolinium oxyorthosilicate
LSO	lutetium oxyorthosilicate
LYSO	lutetium-yttrium oxyorthosilicate
MA-PMT	multi-anode photomultiplier tube
MLEM	Maximum-Likelihood Expectation-Maximization

NEMA	National Electrical Manufacturer's Association
OSEM	Ordered Subset Expectation Maximisation
PDAC	pancreatic ductal adenocarcinoma
PET	Positron Emission Tomography
PSPMT	position sensitive photomultiplier tube
RC	recovery coefficient
R_{int}	intrinsic count rate
R_{NEC}	noise-equivalent count rate
R_r	random coincidence events count rate
R_s	scattered coincidence events count rate
R_t	true coincidence events count rate
R_{TOT}	total coincidence count rate
ROI	region of interest
SF	scatter fraction
SPECT	Single Photon Emission Computed Tomography
STD	standard deviation
TAC	time-activity curve
T_{acq}	acquisition time
TGFB	Transforming Growth Factor-beta
VOI	volume of interest

Part I: Performance Evaluation of Small-animal Scanners

1 Introduction

1.1 NEMA Standard as an Assessment of PET

From the end-user's point of view, the most important qualities of the PET scanner are:

- 1) stability and reliability reflected in high up-time and repeatability of the measurements;
- 2) technical parameters sufficient to detect the features of interest in the scanned subject;
- 3) quantifiability of the acquired images allowing for accurate characterisation and differentiation of the observed phenomena and processes.

Naturally, those criteria cover a variety of technical aspects and, depending on the potential scanning subject (e.g. human, small-animal, etc.) can be, to a different degree, satisfied by many commercially available and research instruments. Each of these devices utilises distinct technology and form factor, resulting in the particular performance characteristics. The question arises as to how one can describe the basic attributes of the PET scanner and its ability to produce an image that would: a) be applicable to all scanner geometries and detector technologies, and b) assess raw hardware capability without corrections and post-processing enhancements. In other words, the challenge is to devise a set of tests that would be applicable to all scanners and allow for their fair comparison.

This need was addressed by a consortium of manufacturers and researchers, who under the umbrella of the National Electrical Manufacturer's Association (NEMA) prepared a standard known as NU2, which was first issued in 1994 and updated in 2001, 2007 and lately in 2012. NU2 describes a set of standardised tests that aim at assessing a few basic parameters of the PET scanner, which depend mostly upon the employed hardware solutions. These parameters are:

- spatial resolution,
- sensitivity of the scanner,
- count-rate performance, and
- image quality.

NU2 is useful to assess most of clinical PET scanners. However, it cannot be applied, at least not without some adaptations, to a sub-class of PET devices called small-animal (micro) PET scanners or Positron Emission Mammographs (Lawrence MacDonald, 2009; Luo *et al.*, 2010). The main reasons for this are related much smaller fields of view of the scanners in question, which become apparent when one examines the sizes of the phantoms prescribed by the standard and the procedures described in, e.g. a spatial resolution test, which cannot be followed as stated for most of those scanners. For this reason 2008 saw a publication of another NEMA standard, an adaptation of the aforementioned NU2 for this group of imaging equipment and called NU4. Since then it has been successfully used by manufacturers and users of small animal PET scanners and became widely acknowledged to the extent that NEMA NU4-2008 tests:

- became a standard way of reporting performance parameters of newly developed equipment;
- lay down the foundation for acceptance testing for newly commissioned devices;
- have become a tool for benchmarking various scanner technologies.

It is, however, worth observing that the standard in its disclaimer states that its purpose is merely to provide guidelines for testing and not “to police or to enforce compliance with the contents of this document”.

(National Electrical Manufacturers Association, 2008) Therefore, even though not every camera on the market was evaluated following the standard to the letter, NEMA NU4 has still been a tremendous help in comparing different devices and making purchasing decisions based on the testing results for many research centres.

1.2 Performance of Other Modalities

1.2.1 NEMA Standards for Other Modalities

Apart from NU4-2008, NEMA has published a few other standards covering molecular imaging. They are summarised in Table 1 below.

Table 1 List of the NEMA Test Standards related to Molecular Imaging and X-Ray devices

Name	Title of the Standard	Status	Type of Device	Scope
NU1-2012	Performance Measurements of Gamma Cameras	Active	Gamma camera, SPECT	Clinical
NU2-2012	Performance Measurements of Positron Emission Tomographs (PETs)	Active	PET	Clinical
NU3-2004	Performance Measurements and Quality Control Guidelines for Non-Imaging Intraoperative Gamma Probes	Active	Gamma probe	Clinical
NU4-2008	Performance Measurements of Small Animal Positron Emission Tomographs (PETs)	Active	PET	Pre-clinical
XR10-1986 (R1992, 1998, 2003)	Measurement of the Maximum Symmetrical Radiation Field from a Rotating Anode X-Ray Tube Used for Medical Diagnosis	Rescinded	X-ray	Clinical
XR11-1993 (R1999)	Test Standard for the Determination of the Limiting Spatial Resolution of X-Ray Image Intensifier Systems	Rescinded	X-ray	Clinical
XR15-1991 (R1996, 2001)	Test Standard for the Determination of the Visible Entrance Field Size of an X-Ray Image Intensifier (XRII) System	Active	X-ray	Clinical

XR16-1991 (R1996, 2001)	Test Standard for the Determination of the System Contrast Ratio (SCR) and the System Veiling Glare Index (SVGI) of an X-Ray Image Intensifier (XRII) System	Active	X-ray	Clinical
XR17-1993 (R1999)	Test Standard for the Measurement of the Image Signal Uniformity of an X-Ray Image Intensifier (XRII) System	Rescinded	X-ray	Clinical
XR18-1993 (R1999)	Test Standard for the Determination of the Radial Image Distortion of an X-Ray Image Intensifier (XRII) System	Rescinded	X-ray	Clinical
XR19-1993 (R1999)	Electrical, Thermal and Loading Characteristics of X-Ray Tubes Used for Medical Diagnosis	Rescinded	X-ray	Clinical
XR21-2000	Characteristics of and Test Procedures for a Phantom to Benchmark Cardiac Fluoroscopic and Photographic Performance	Rescinded	X-ray	Clinical
XR22-2006	Quality Control Manual Template for Manufacturers of Displays and Workstations Labelled for Final Interpretation in Full-Field Digital Mammography (FFDM)	Active	X-ray Mammograph	Clinical
XR23-2006	Quality Control Manual Template for Manufacturers of Hardcopy Output Devices Labelled for Final Interpretation in Full-Field Digital Mammography (FFDM)	Active	X-ray Mammograph	Clinical
XR5-1992 (R1999)	Measurement of Dimensions and Properties of Focal Spots of Diagnostic X-Ray Tubes	Rescinded	X-Ray	Clinical

However, as of 2016, NEMA has not published a standard that would cover any modality within the realm of small-animal scanners other than PET. Works have started on pre-clinical gamma camera performance testing guidelines and it is expected that the new standard will be published within the next few years. In terms of X-Ray devices, out of 17 different standards (called “XR” standards) listed on the NEMA website (National Electrical Manufacturers Association, 2015), 11 were rescinded. It is worth noting that the active standards cover quality control guidelines for mammography, intraoperative or interventional

(e.g. angiography) X-Ray equipment, but not performance evaluation like NU1, NU2, NU3 or NU4.

1.2.2 Performance Testing

Since there are no published guidelines for SPECT or CT testing, manufacturers and users tend to use custom protocols adapted from what was published for clinical devices. It should be no surprise that literature and published specifications list a wide variety of custom tests, which on most occasions can be reduced to common denominators. Kachelriess notes the most basic parameters of micro-CT scanners, which may not provide enough details for benchmarking, but allow at least a comparison between various imaging protocols. (Kachelriess, 2008) Those parameters are:

- spatial resolution,
- image noise,
- dose given to subject.

The latter is certainly of great importance in small-animal imaging. Boone, Valazquez and Cherry estimate typical dose received by a mouse scanned using micro-CT to be between 100 and 300 mGy, which is 10 times higher than doses delivered to human during an analogous scan. (Boone *et al.*, 2004) This is not lethal, although may be sufficient to alter biological pathways and immune response in an animal (Boyd *et al.*, 2006), affecting experimental outcome. (Willekens *et al.*, 2010) It is particularly important to limit the radiation exposure from CT imaging when conducting longitudinal studies involving this modality. A cumulative absorbed whole-body dose of 5 to 7.6 Gy (depending on the strain) is estimated to be lethal to mice (it is the LD_{50/30} dose, which means that within 30 days, half of the exposed population will die). (Funk *et al.*, 2004; Willekens *et al.*, 2010) But even smaller doses can cause an unintended, “therapeutic” effect on tumours in oncological studies. Therefore, it is vital to use imaging parameters that would provide sufficient image quality, but would limit the exposure to ionizing radiation. The dose received from a CT scan is proportional to the current on the lamp, but the proportionality changes with

the voltage on the X-ray lamp. (Kachelriess, 2008) It will also be higher if more projections are taken, which is usually a function of the scan duration.

Certainly, the variety of phantoms and protocols used makes it impossible to compare performance of emerging micro-CT devices. It is another matter if an objective comparison is as crucial for those devices as it is for micro-PET or SPECT scanners. In dual or tri-modal scanners CT serves usually as a mean to provide an anatomical reference, which aids with an interpretation of the functional (PET or SPECT) information that it is being overlaid upon. Because the level of detail they provide is usually sufficient for dual-modality imaging, the technology they use is not a focus of major improvements and can be considered mature, unlike the realm of small animal PET or SPECT, which are still developing fields. Therefore, in case of micro-CT users often rely on the information provided by the manufacturer for the choice of the most suitable imaging parameters and the quality control protocols, which means they may vary greatly between different sites.

1.3 Bruker Albira PET/SPECT/CT

1.3.1 Landscape of Pre-clinical Tri-modal (PET/SPECT/CT) Scanners

Albira (Bruker Biospin Corp., Billerica, MA, USA) is one of few commercial tri-modal, PET/SPECT/CT small-animal platforms. It is a modular device, which means it can be bought as a stand-alone PET, SPECT or CT, as a dual-modality or tri-modal system. Furthermore, PET is available in 1, 2 or 3-ring configuration and SPECT can use two models of gamma camera. The image of a two-ring Albira PET/SPECT/CT is shown on Figure 1. The features of all of those sub-systems are provided in Section 1.3.2. Multi-modal scanning in Albira is facilitated by sequential scanning with an imaging bed moving between PET and SPECT/CT gantries. Because of this setup, i.e. physical separation of those two gantries, it is not possible to select PET and SPECT acquisition protocols as part of the same

study. Radionuclide imaging is always performed first with CT (if selected) being performed as second.

Some of the following text and figures in the reminder of Introduction come from my review on the evaluation of the Albira PET system using the NEMA NU4-2008 standard. (Pajak *et al.*, 2016)

1.3.2 Albira Features

1.3.2.1 *PET*

Most small animal PET scanners use discreet crystal detector technologies, which utilize an array of crystals in a detector block. A unique feature of the Albira PET scanner is that it implements continuous lutetium yttrium orthosilicate (LYSO) crystals. Each crystal has a shape of a 10 mm- thick, truncated pyramid with 50×50 mm² base and 40×40 mm² top. Behind the crystal lies a position-sensitive photomultiplier (PS-PMT, H8500 Hamamatsu) and electronics using Anger logic to provide depth-of-interaction (DOI) information for each detected annihilation photon. (Balcerzyk *et al.*, 2009) Each crystal is painted black to prevent internal reflection and every detector is covered with tungsten. Together such an assembly constitutes a single detector block.

Eight detectors form a ring and up to three rings can be stacked next to each other. An interesting feature of the two- or three-ring configuration is the 14.4 mm gap between the rings (shown on Figure 2), which is the result of the crystal shape.

The geometry of two-ring Albira PET system is shown on Figure 3.



Figure 1 (a) A two-ring Bruker Albira PET/SPECT/CT, (b) an animal imaging bed, (c) inside of the scanner (*) showing the stationary PET module and gamma cameras on the rotating SPECT gantry (**).

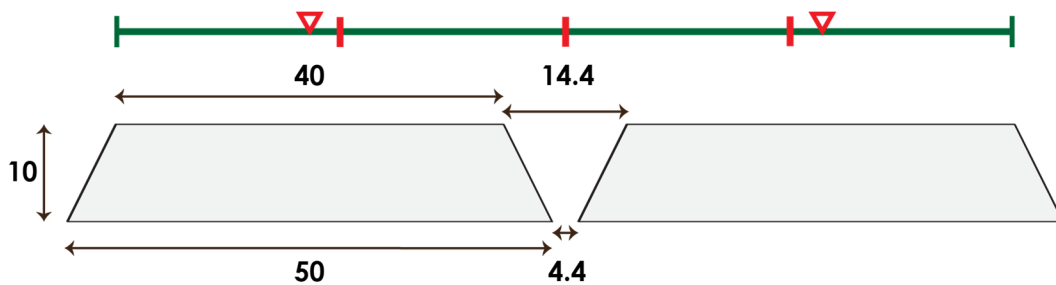


Figure 2 Side view of the two adjacent rings in Albira PET emphasising the gap between the front of the detector crystals and the relevant dimensions given in mm. The green line indicates the full axial field of view and the short red lines indicate the axial positions at which spatial resolution measurements are taken. The red triangles mark the centre of each crystal. (Pajak *et al.*, 2016)

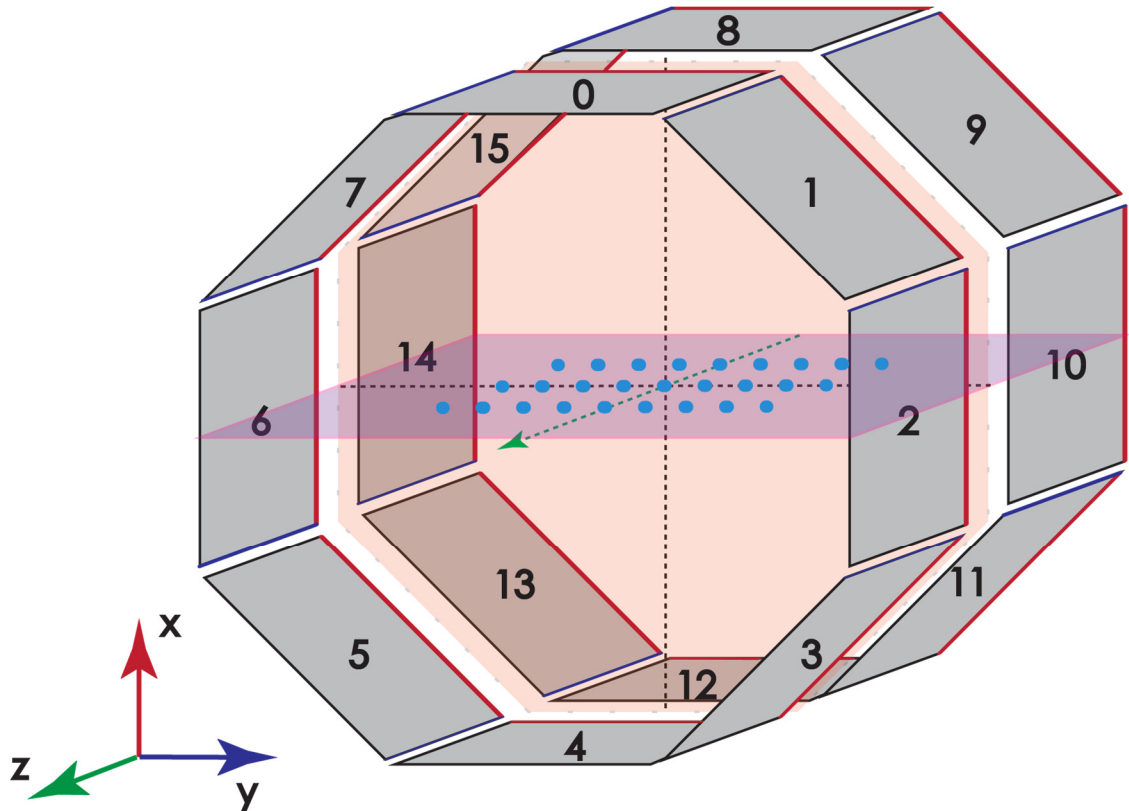


Figure 3 Schematic diagram showing 2-ring Albira PET with octagonal detector arrangement in each ring and the gap between the rings. Blue dots show the measurement points for spatial resolution in NEMA NU4 test. (Pajak *et al.*, 2016)

The distance between the faces of two crystals lying opposite each other is 121.5 mm, but the physical aperture is 105 mm due to the tungsten shielding around the detectors. (Sanchez *et al.*, 2012) Coincidences are detected in 1-to-3 mode, which means that for example detector 0 may detect coincidence in pair with detectors 3, 4 or 5 in ring 1 or 11, 12, 13 in ring 2 or 19, 20 and 21 in a 3-ring configuration. This arrangement provides $80 \times 80 \text{ mm}^2$ trans-axial field of view (FOV). The axial FOV depends on the number of rings and can be 40 mm (one ring), 94.4 mm (two rings) or 148.8 mm (three rings).

The timing window for detecting coincidences is set to 5 ns. The energy window for accepted events is pre-defined by the user in Albira software (Albira Manager tool). It is set as a percentage of the annihilation photon energy, 511 keV. 30% energy window (358-664 keV) is recommended by the manufacturer for the

routine animal imaging, but a 50% energy window (255-767 keV) can also be used for the performance testing. Other values can also be set.

The Albira PET has the ability to acquire images in static or dynamic studies. The imaging time (or a sequence of frames of certain duration) has to be pre-defined in a study protocol. As of the Albira software ver. 5.6, once a dynamic study is acquired using given frame durations, the only adjustment permitted is splitting longer acquisitions into a sequence of shorter ones. However, there is no option to merge shorter frames into longer.

In general, the reconstruction software for the Albira is available in two configurations: as central processing unit (CPU)-powered or graphics processing unit (GPU)-aided one. The GPU-powered reconstruction software takes advantage of high-performance parallel computing algorithms and works on computer architectures featuring up to 8 graphics cards. This offers robustness and substantially shortens reconstruction times, allows smaller reconstructed voxel sizes and the CT-based attenuation correction (for PET). However, the price of the GPU-powered reconstruction workstations may mean that it will need to be subjected to a cost-benefit analysis prior purchase.

The reconstruction software and workstation used in the following study is the CPU-based version. Its default reconstruction algorithm is the maximum likelihood expectation maximisation (MLEM) with 12 iterations and $1 \times 1 \times 0.944 \text{ mm}^3$ voxel size. The number of iterations can be freely changed by the user. Few other options, for example reconstructed FOV, the crystal pixellation and the voxel sizes of the reconstructed image are pre-set, but can be changed by the manufacturer at request. The smallest reconstructed voxel size a CPU-powered software option offers is $0.5 \times 0.5 \times 0.5 \text{ mm}^3$ as opposed to $0.3 \times 0.3 \times 0.3 \text{ mm}^3$ available in the GPU-aided one.

Albira PET is additionally capable of gating triggered by the signal from the cardiac or respiratory animal monitoring system.

1.3.2.2 SPECT

The Albira SPECT consists of two gamma cameras positioned 180° apart. Each camera consists of a 4 mm-thick monolithic caesium iodide CsI(Na) crystal behind which lies a position sensitive photo-multiplier tube (PS-PMT) and electronics. (Sanchez *et al.*, 2013) At the moment there are two models of the available camera: S108 (100×100 mm² crystal) and older and smaller S102 (50×50 mm²). Both cameras come with a single pinhole collimator (SPH) and a multi pinhole collimator - S108 with 9 pinholes and S102 with 5 pinholes all of which are made of tungsten and need to be changed manually. According to manufacturer specification, at a 140 keV photo-peak the energy discrimination is 14%, however, the energy ranges differ and are 30 to 400 keV for S108 and 40 to 250 keV for S102. Depending on their proximity, both cameras provide a variable FOV (axial and trans-axial), S108 30 to 140 mm (pre-set values of 25, 50, 80 and 120 mm) (Spinks *et al.*, 2014) and S102 20 to 80 mm (pre-set values of 20, 40, 60 and 80 mm). According to the manufacturer, the minimum resolution for S108 is 0.6 mm and for S102 is 0.8 mm. Cameras are mounted on a rotating gantry and during a scan obtain 60 projections over 180° or 360°, every 6°. The Albira SPECT comes equipped with special narrow bed for 20 mm FOV high-resolution imaging, additionally to the mouse and rat imaging beds used in the larger FOV imaging and utilised also in the PET and CT imaging. (Bruker BioSpin, 2012)

1.3.2.3 CT

Albira CT consists of the x-ray lamp and detector that are rotating around the subject in the step-and-shoot mode. The x-ray source and detector are mounted on the same gantry as SPECT cameras. The nominal focal spot size of the generated x-ray beams is 35µm. (Bruker BioSpin, 2012) The potential difference between cathode and anode can be regulated between 4 and 50 kV with 35 kV and 45 kV being the two settings available to the end user as pre-sets. The current on the cathode can be adjusted between 0 and 1 mA and the pre-sets available to the user by default are 200µA and 400µA. The current on the lamp is responsible for the dose received by the subject being scanned. The current on

the lamp versus deep dose equivalent, as measured by the manufacturer, is shown in Figure 4. The dose is a function of the scan length, which is proportional to the number of projections.

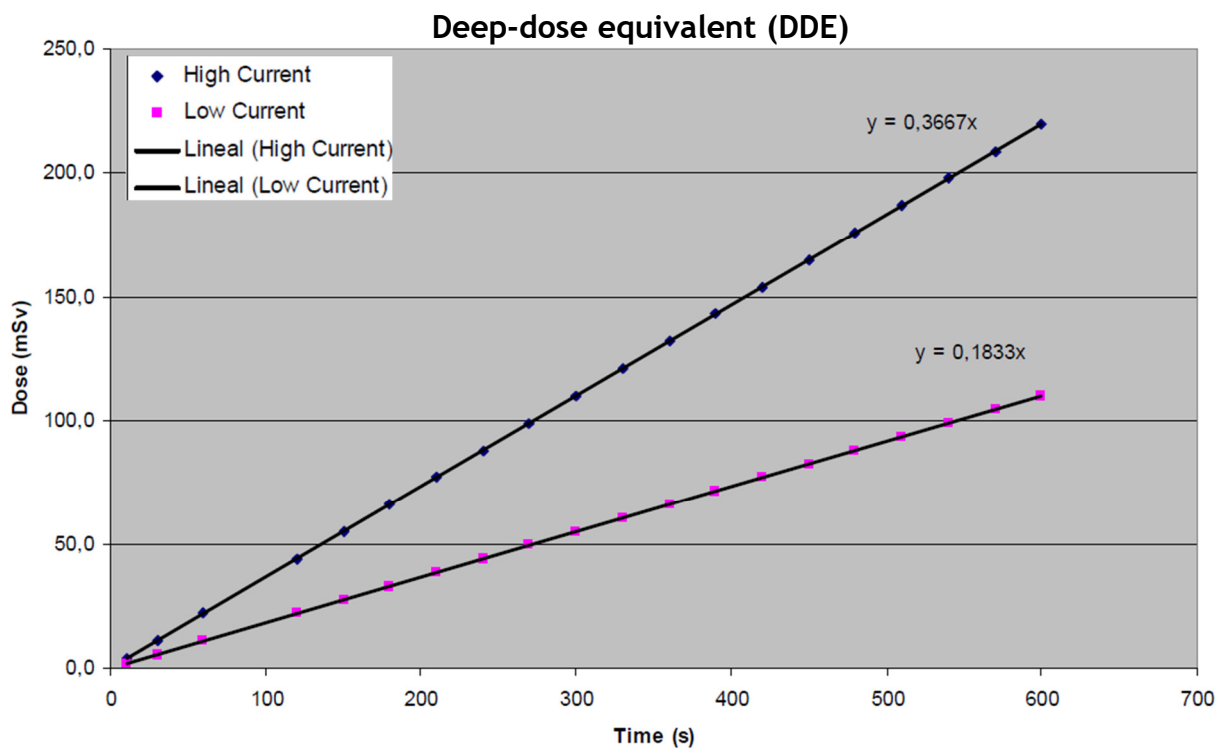


Figure 4 Deep Dose Equivalent as a function of time in the Albira CT, courtesy of Carlos Correcher (Oncovision).

1.3.2.4 *Animal Handling and Monitoring*

The Albira comes with two types of animal imaging beds: for a mouse and for a rat, which differ in size, but otherwise look alike. Both are fit with a tooth-bar, which allows for stretching an animal on the bed and have a nose cone, which feeds anaesthesia. Anaesthesia is fed through the tubing, which runs from the face mask, along the bed, imaging arm and then to the panel below imaging bed. From there it can be connected with a supply using a luer connector.

The Albira is compatible with BIOPAC animal monitoring system (BIOPAC Systems, Inc., Goleta, CA, USA), which can be purchased with the scanner as an option. When purchased together, it connects with the Albira through a panel below the imaging arm. Exact implementation depends on the chosen modules. All versions of the Albira come also with a camera at the back of the imaging gantry, which feeds an image into the acquisition screen at the computer. This allows for the real-time observation of the animal during the study.

1.3.2.5 *Software*

The Albira software suite contains acquisition and reconstructions software along with a supervision module used for regular quality checks. It has also the options to manage some study information the tracer used, researcher IDs, radionuclides and energy windows (PET and SPECT), and acquisition settings for the all three modalities.

1.3.2.6 *List-mode format*

The Albira PET saves all the acquired data in list-mode (LM) format. Each LM file is binary and consists of 176-bit long header and then the list of all the registered events. Each event is described by the detector pair that registered it and a timestamp. In addition, the xy co-ordinates on each detector where the detection of the coincidence photon took place and its energy are given. When only one photon was detected within the timing window (set to 5 ns), the event

contains a “single flag”, which has a hex value of “0x100”. In this instance information from only one of the detectors is then available. The last value registered for each single or coincidence event is the “amount”, which is the floating-point value greater than 1 coming from the Q-factor correction. The latter is a correction, which compensates for the dead time, i.e. the loss of the linearity in the detector’s response as activity increases. It is calculated during the periodical calibration conducted by the vendor.

An example of the data in list-mode format is shown in Figure 5 and was generated using *lmViewer* command-line utility supplied by the manufacturer.

```
E:\programming\lmViewer\Release\bin>lmViewer.exe e:\programming\sample.lm -print
Header info:
Version: 5.0      time: 60.015000 M: 8      R: 2      Ring distance: 14.400000
-----
Pair  Amout  Time   X1     Y1     E1     X2     Y2     E2     G
-----
005  1.00047  19.085  030    281    340.43  000    000    0.00
005  1.00607  19.087  121    097    565.19  000    000    0.00
005  1.00500  19.089  266    195    674.49  000    000    0.00
006  1.00773  19.085  129    060    322.22  055    233    435.62
000  1.00510  19.086  193    260    323.27  000    000    0.00
000  1.01120  19.089  273    019    339.76  172    004    448.86
011  1.00000  19.087  001    276    331.91  000    000    0.00
042  1.00750  19.088  041    283    580.17  077    044    517.95
042  1.00750  19.088  224    077    404.20  261    223    434.54
010  1.00249  19.088  048    257    611.31  000    000    0.00
031  1.00506  19.087  261    118    496.79  273    187    624.92
031  1.00506  19.088  073    009    608.26  014    272    586.36
045  1.00081  19.088  214    023    596.94  233    091    287.32
031  1.00506  19.088  070    235    625.07  089    060    386.82
029  1.00330  19.088  192    138    660.09  210    125    698.96
031  1.00506  19.088  155    047    593.19  269    197    623.19
029  1.00330  19.088  015    268    602.65  023    270    381.22
029  1.00330  19.088  002    168    437.89  131    085    562.40
031  1.00506  19.088  054    016    375.12  017    296    546.18
029  1.00330  19.089  089    213    632.90  041    046    626.16
Press Any Key to continue
```

Figure 5 Example output of the *lmViewer* utility showing the format of Albira PET list-mode files

2 Aims and Objectives

2.1 PET

The aim of the following series of experiments is to evaluate Bruker Albira 2-ring PET according to NEMA NU4-2008 standard, which has not been previously conducted. The following table (Table 2) summarises all parts of the NU4 standard and their individual aims.

Table 2 Summary of the aims of each part of NEMA NU4-2008 protocol.

Part	Aim
Spatial resolution	To assess the ability of the scanner to resolve very small features of the subject, i.e. what is the distance at which two points at the image can be distinguished from each other.
Sensitivity	To assess how sensitivity of the instrument changes along the scanner's axis.
Count-rate performance	To assess the range of radioactivity doses within which the scanner's response is linear and the value at which the detectors saturation occurs; estimation of the contribution to the measured signal coming from: true coincidence events, scattered events and random events.
Image Quality	To determine how well the instrument (and reconstruction software) deals with partial volume effect, level of noise and how well it resolves small structures under typical conditions occurring during small animal imaging.

This assessment is meant to establish some of the basic hardware characteristics of the PET component of the Albira PET/SPECT/CT system and ascertain its suitability for mouse imaging.

2.2 CT

Since no standard analogues to NEMA NU4 exist for micro-CT, the CT sub-system of the Albira is assessed in terms of its temporal stability, spatial resolution and contrast recovery using custom protocol. The goal is to establish the optimal settings for mouse imaging using data obtained by imaging mouse-like microCT phantom and verify those settings by conducting cadaver imaging. Additionally, the impact of the available reconstruction settings on the image quality is also investigated.

3 Methods

3.1 NEMA NU4-2008

Most of the methods described below were published before in (Pajak *et al.*, 2016).

3.1.1 Spatial Resolution

3.1.1.1 Measurements

A ^{22}Na point source of nominal activity of 370 kBq (0.25 mm active sphere diameter, embedded in the middle of the acrylic cube 10 mm in each extent; Eckert & Ziegler Isotope Products, Valencia, CA, USA; shown schematically in Figure 6) was first positioned on the thin cardboard support at the axial and trans-axial centre of the FOV.

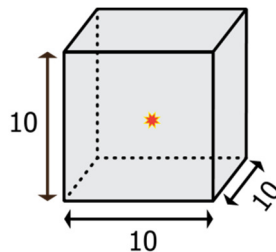


Figure 6 Schematic picture showing the ^{22}Na point-source used in spatial resolution and sensitivity measurements. (Pajak *et al.*, 2016)

60 second acquisitions were then taken at the radial offsets of: 0, 5, 10, 15, 20 and 25 mm. The same procedure was repeated for a quarter of the axial FOV (23.6 mm from the axial centre of the FOV). The energy window was set to 50% (255-767 keV).

All measurement points were marked as blue dots and are shown on Figure 3 in the Introduction above.

3.1.1.2 *Data processing and analysis*

Using a customised program (explained in more detail in section 3.1.5 Computation) data were filtered to include only events within 30% energy window (i.e 358-664 keV). Then all data-points for both, 50% (255-767 keV) and 30% energy windows were reconstructed using reconstruction software provided by the manufacturer (MLEM, 20 iterations, $0.5 \times 0.5 \times 0.5$ mm³ voxel size, no corrections apart from built-in normalisation correction applied) and using STIR: Software for Tomographic Image Reconstruction (Thielemans *et al.*, 2006). The algorithms used were single slice re-binning (SSRB) and 2D FBP (filtered back projection) with $0.33 \times 0.33 \times 0.33$ mm³ voxel size and no corrections applied. It is worth noting that since the Albira's list-mode format is proprietary, it could only be used in STIR after conversion into one of the supported formats, namely COMPET list-mode format. The appropriate patch interpreting COMPET list mode format in STIR was provided by Mr David Volgyes. Normalization to correct for variations in the detector efficiency was not applied for either energy window setting when using STIR. In order to analyse point spread functions (PSF) of the reconstructed images, AMIDE: Amide's a Medical Imaging Data Examiner software (Loening & Gambhir, 2003) was used. Profiles were generated into: radial, tangential and axial directions and spatial resolution was measured as Full Width at Half Maximum (FWHM) and Full Width at Tenth Maximum (FWTM), which are defined as shown in Figure 7.

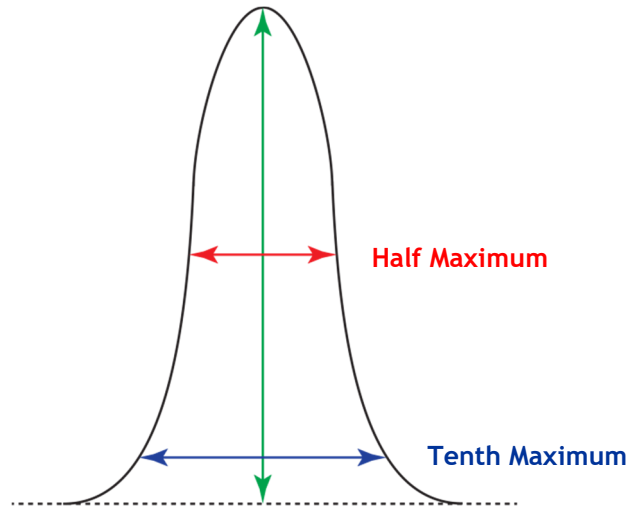


Figure 7 Definition of the Full Width at Half Maximum (FWHM) and Full Width at Tenth Maximum (FWTM). The peak denotes a point spread function (PSF) measured in a given image plane.

3.1.2 Sensitivity

3.1.2.1 *Measurements*

The same source as the one used in section 3.1.1 Spatial Resolution was placed on the thin cardboard support at the trans-axial centre of the FOV, at the edge of the axial FOV. A series of 60 second acquisitions were then taken (sufficient to acquire at least 10^4 of prompt counts). Imaging bed was used to move the source along the scanner's axis in 1 mm steps from one edge of the axial field of view to the other. Because the LYSO crystals, which are part of the detector assembly, are mildly radioactive, a background acquisition was acquired for 5 minutes without any source inside the scanner in order to establish an intrinsic counts contribution from the crystals.

3.1.2.2 *Data processing and analysis*

A customised program described in the section 3.1.5 Computation was used to decode the list mode files, create sinograms and to perform the required calculations on them.

All oblique lines of response were assigned to the appropriate axial slices using SSRB and sinograms (trans-axial bin size of 1 mm, slice distance 1 mm) were constructed. In every slice, for every angle in the sinogram, the pixel of the maximum intensity was found and all counts outside 10 mm from that pixel were set to 0. All the remaining counts in every slice of the sinogram were summed and all constructed sinograms added together. Finally, background counts masked in the same manner and normalised to the scan duration were subtracted from each slice.

The system sensitivity S_i (in cps per Bq) was computed as follows:

$$S_i = \left(\frac{R_i - R_{B,i}}{A_{cal}} \right),$$

where R_i denoted a count rate in the slice i , $R_{B,i}$ is a normalised background count rate in that slice (both in cps) and A_{cal} is the source activity expressed in Bq.

Considering the branching ratio of ^{22}Na (fraction of the total radiation of the radionuclide that comes from positrons), which is 0.906, the absolute system sensitivity $S_{A,i}$ in the slice i expressed as a percentage can be calculated as:

$$S_{A,i} = \frac{S_i}{0.906} \times 100,$$

where S_i is system sensitivity in the slice i .

NEMA NU4 defines the mouse-region as the central 7 cm of the instrument's axial FOV and the rat-region as the central 15 cm. Both lengths are meant to be the approximate sizes of the average rodent of these species. Therefore, the system and the absolute system sensitivity over the mouse-region were obtained by summing the slices S_i and $S_{A,i}$ over the central 7 cm of the axial FOV, respectively. Because the total axial FOV of 2-ring Albira PET is less than 15 cm, the sensitivity (system and absolute) over the rat-region and the total sensitivity are equal, and were calculated by summing the counts over all slices.

3.1.3 Count-rate Performance

Mouse Phantom

The mouse-like phantom (Oncovision, Valencia, Spain) conformed to the NEMA NU4-2008 standard. The phantom was made of high density polyethylene ($0.96 \pm 0.1 \text{ g/cm}^3$) in the shape of a cylinder $70 \pm 0.5 \text{ mm}$ long and $25 \pm 0.5 \text{ mm}$ in diameter. A cylindrical hole of 3.2 mm diameter was drilled parallel to the central axis and at the radial distance of 10 mm to it. A schematic of the phantom is shown in Figure 8.

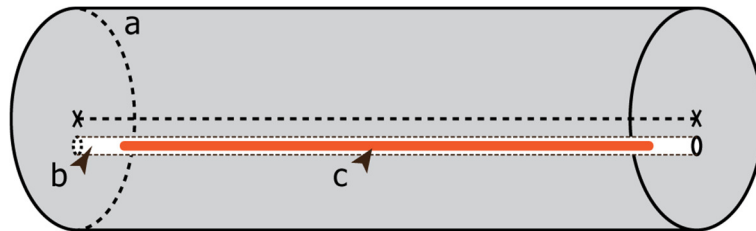


Figure 8 Schematic figure showing phantoms used in count-rate performance part of the NEMA NU4 protocol, where a) denotes the body of the phantom, b) the hole drilled off-centre, and c) inserted radioactive line-source. (Pajak *et al.*, 2016)

Rat-like Phantom

The dimensions of the rat-like phantom conformed to the NEMA NU4-2008 standard. Briefly, the phantom was made of the same material as the mouse-like phantom and had a shape of cylinder $150 \pm 0.5 \text{ mm}$ long and $50 \pm 0.5 \text{ mm}$ in diameter. A cylindrical hole of 3.2 mm in diameter was drilled along the central axis at 17.5 mm radial offset. A schematic of the phantom is shown in Figure 8.

3.1.3.1 *Measurements*

Mouse-like phantom

The tubing of 2.5 mm external diameter was filled with 143 MBq of ^{18}F over 60 mm and threaded through the hole in the phantom, so the activity in the tubing

was aligned with the central 60 mm of the phantom. The phantom was positioned in the middle of the FOV and a series of 20 min acquisitions were taken over several half-lives until the activity decayed to 44.8 kBq.

Rat-like phantom

Tubing of 2.5 mm external diameter was filled with 233 MBq of ^{18}F over 140 mm and threaded through the rat-like phantom (Oncovision, Valencia, Spain), so the activity in the tubing was aligned with the central 140 mm of the phantom. After positioning the phantom in the centre of the FOV, a series of 20 minute acquisitions was taken until the activity decayed to 115.6 kBq.

3.1.3.2 Data processing and analysis

Acquisition files were read and processed using a customised program described in section 3.1.5 Computation. First, using SSRB the data were re-binned into a stack of 2D sinograms with 1 mm pixel size and slice distance of 1 mm. All sinograms were masked so that only the pixels located within a band 16 mm wider than the diameter of the phantom were kept and the rest set to 0. Then for every row in a sinogram, the pixel with the greatest intensity was identified as representing the centre of the line source. Projections were shifted so these pixels coincided with the centre of the projection. After this alignment, the sum projection was produced by summing all vertical pixels for every radial offset. The counts within the central 14 mm of the summed projections represented the sum of true, random and scattered events while the counts outside this strip are considered to contain only random and scattered events. Using linear interpolation, the pixel values at the borders of the above strip were calculated and their average multiplied by the number of pixels between them. The product of this multiplication was assumed to represent random and scattered events within the strip and by subtracting this from all events within the strip, the true counts were found. The total counts were found as a sum of all events in the sum projection. By subtracting the true counts from total counts, random and scattered events were calculated.

Event count-rates (R) for slice i of the acquisition j were calculated by dividing respective counts (C) by the duration of acquisition ($T_{acq,j}$):

$$R_{i,j} = \frac{C_{i,j}}{T_{acq,j}}$$

Using acquisition taken at low activity, when count losses and random events were less than 1.0% of total events rate, scatter fraction (SF) was calculated as:

$$SF = \frac{R_s}{R_t + R_s},$$

where R_s is scattered- and R_t a true-event rate.

Next, for slice i of acquisition j , the noise-equivalent-rate ($R_{NEC,i,j}$) was computed as:

$$R_{NEC,i,j} = \frac{R_{t,i,j}^2}{R_{TOT,i,j}},$$

where $R_{TOT,i,j}$ denotes total event rate and $R_{t,i,j}$ - true event rate for slice i of acquisition j .

The true event rate ($R_{t,i,j}$) within the ± 7 mm band from the edge of the line source in every slice i of the acquisition j was computed as:

$$R_{t,i,j} = \frac{(C_{TOT,i,j} - C_{r+s,i,j})}{T_{acq,j}},$$

where $C_{TOT,i,j}$ is the total number of coincidences in the slice i of the acquisition j , $C_{r+s,i,j}$ - the number of random and scattered coincidence events in slice i of the acquisition j and $T_{acq,j}$ - the duration of the acquisition j .

Random event rate ($R_{r,i,j}$) was estimated as follows:

$$R_{r,i,j} = R_{TOT,i,j} - \left(\frac{R_{t,i,j}}{1-SF_i} \right),$$

where $R_{TOT,i,j}$ is the total count-rate in the slice i of the acquisition j , $R_{t,i,j}$ is the true coincidence events count-rate and SF_i is the scattered events fraction.

Scattered event rate ($R_{s,i,j}$) was then calculated as:

$$R_{s,i,j} = R_{TOT,i,j} - R_{t,i,j} - R_{r,i,j} - R_{int,i}$$

where $R_{TOT,i,j}$ is a total coincidence event rate, $R_{t,i,j}$ - rate of true events, $R_{r,i,j}$ - rate of random events, $R_{int,i}$ - intrinsic event rate derived from a scan of each phantom without any activity in the tubing, and finally, i is a slice and j denotes an acquisition.

Summing over all slices i for every acquisition j the scatter fraction (SF_j) was calculated as:

$$SF_j = \frac{R_{s,j}}{R_{t,j} + R_{s,j}}$$

where $R_{s,j}$ is the rate of scattered events and $R_{t,j}$ - true event rate.

3.1.4 Image Quality

3.1.4.1 *Measurements*

An image quality phantom (QRM Quality Assurance in Radiology and Medicine GmbH, Moherendorf, Germany) conformed to NEMA NU4-2008 specification. Briefly, it had a shape of a cylinder 50 mm long and 30 mm in diameter (as measured on the inside). It was made of polymethylmethacrylate and comprised of three parts:

- a) two cylindrical chambers having 1 mm-thick walls, each 15 mm in length, 8 mm in diameter (internal dimensions), where one was filled with non-radioactive water and the other contained air;
- b) a region containing five rods of: 5, 4, 3, 2 and 1 mm in diameter and 20 mm long, which were filled with a radioactive solution;
- c) an uniformity region, 30 mm long, which contained a radioactive solution.

A schematic of the phantom is shown in Figure 9.

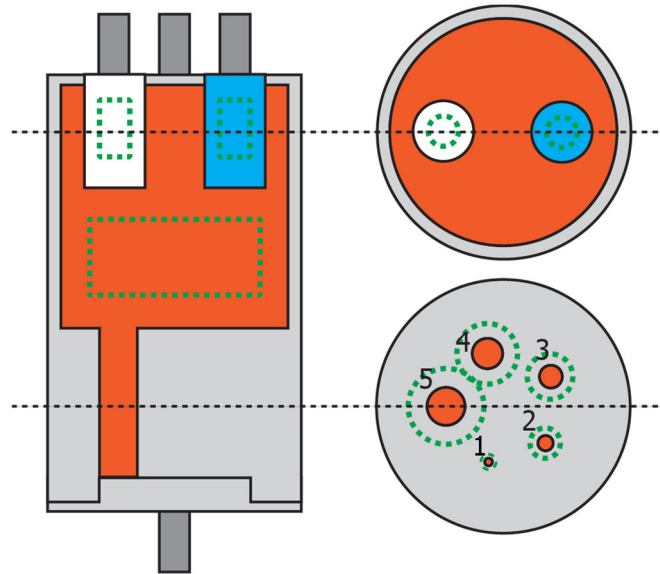


Figure 9 Schematic picture showing NEMA NU4-2008 Image Quality phantom. Grey colour denotes the body of the phantom. White colour denotes the air-filled (non-radioactive) chamber, blue the water-filled one and orange shows the water solution of the ^{18}F . Green dashed lines indicate the regions and volumes of interest that were drawn within the image. (Pajak *et al.*, 2016)

The phantom was filled with 3.55 MBq of the solution of ^{18}F , positioned centrally within the scanner's FOV and imaged for 20 min.

3.1.4.2 *Data processing and analysis*

The image was then reconstructed using Albira built-in reconstruction software with a $0.5 \times 0.5 \times 0.5 \text{ mm}^3$ voxel size (the smallest available) and MLEM algorithm using variable number of iterations: from 2 to 100. Scatter, randoms and decay corrections were applied for every reconstruction.

Using PMOD (PMOD Technologies Ltd., Zurich, Switzerland), a cylindrical volume of interest (VOI) (22.5 mm diameter and 10 mm length) was drawn over the centre of the homogenous region (as shown in green dashed line on Figure 9). Maximum, minimum, mean and standard deviation values were noted. Next, a cuboid VOI was drawn over the rods region, covering the slices over the central 10 mm of their length. The image was cropped to this VOI and slices averaged to lower the noise. Circular ROIs, twice the physical size of each rod (Figure 9),

were drawn around them and the maximum intensity pixel within each ROI was identified. Using transverse co-ordinates of the maximum intensity pixels, line profiles through all rods were generated. The recovery coefficients (RC) for every rod were calculated as the ratio of the average counts ($Mean_{lineprofile}$) for the rod along the generated profile to the average counts in the uniformity region ($Mean_{uniform}$). The error on this value ($\%STD_{RC}$) was calculated as:

$$\%STD_{RC} = 100 \cdot \sqrt{\left(\frac{STD_{lineprofile}}{Mean_{lineprofile}}\right)^2 + \left(\frac{STD_{uniform}}{Mean_{uniform}}\right)^2},$$

where $STD_{lineprofile}$ and $STD_{uniform}$ refer to the standard deviations calculated for the line profile and the uniformity region, respectively.

To estimate the accuracy of corrections, two cylindrical VOIs, each 4 mm in diameter (half of diameter of each chamber) and 7.5 mm long, were drawn centrally over air- and water-filled chambers (white and blue cylinders on Figure 9). Spill-over ratios (SOR) were calculated as the ratio of the mean activity concentration within the VOIs to the mean counts within the uniformity region ($Mean_{uniform}$):

$$SOR_{water} = \frac{Mean_{water}}{Mean_{uniform}},$$

$$SOR_{air} = \frac{Mean_{air}}{Mean_{uniform}}.$$

The errors on the SOR values, $\%STD_{water}$ and $\%STD_{air}$ were calculated similarly to those for rods region:

$$\%STD_{water} = 100 \cdot \sqrt{\left(\frac{STD_{water}}{Mean_{water}}\right)^2 + \left(\frac{STD_{uniform}}{Mean_{uniform}}\right)^2},$$

$$\%STD_{air} = 100 \cdot \sqrt{\left(\frac{STD_{air}}{Mean_{air}}\right)^2 + \left(\frac{STD_{uniform}}{Mean_{uniform}}\right)^2},$$

where $STD_{uniform}$ denotes the standard deviation within the uniformity region and STD_{water} , and STD_{air} are the standard deviations within the water and air chamber VOI, respectively.

3.1.5 Computation

3.1.5.1 *Geometry transformation for sinogram generation*

The sensitivity and count-rate performance parts of the NEMA protocol required processing of the sinograms generated from data acquired containing only the coincidence events (single events were discounted). To build a sinogram the detector geometry had to be transformed into the scanner geometry (Figure 3) using a customised program.

Section 1.3.2.6 List-mode format describes the structure of Albira PET list-mode file. To describe the transformation between the detector and scanner geometry, capital letters XY denote the detector plane co-ordinates and small letters xyz denote the detector co-ordinates in the scanner space. As mentioned previously, each detector crystal is virtually pixelated into 300×300 grid. Hence, every event could be detected in one of 9×10^4 detection positions giving the virtual pixel a size of $0.1333 \times 0.1333 \text{ mm}^2$ (40 mm/300). In the list-mode file, this position is already corrected for the DOI.

The initial step required loading the list-mode file using custom-written C++ application. First the header (initial 176 bytes) was read and then every 40 bytes, which is the amount of memory used to save information about one coincidence event. Within each coincidence event the detector pair number assigned to that event was read. Table 3 lists all 48 detector pairs available in 2-ring Albira PET.

Table 3 Summary of all available detector (det.) pairs for the 2-ring Albira PET

Pair no	0	1	2	3	4	5	6	7	8	9	10	11	12	13	14	15
Det. 1	0	1	2	3	0	0	1	1	2	2	3	4	8	9	10	11
Det. 2	4	5	6	7	3	5	4	6	5	7	6	7	12	13	14	15
Pair no	16	17	18	19	20	21	22	23	24	25	26	27	28	29	30	31
Det. 1	8	8	9	9	10	10	11	12	0	4	1	5	2	6	3	7
Det. 2	11	13	12	14	13	15	14	15	12	8	13	9	14	10	15	11
Pair no	32	33	34	35	36	37	38	39	40	41	42	43	44	45	46	47
Det. 1	0	0	3	5	1	1	4	6	2	2	5	7	3	6	4	7
Det. 2	11	13	8	8	12	14	9	9	13	15	10	10	14	11	15	12

Next, the two detectors involved in the coincidence event were considered separately. Taking into account the scanner geometry, the Y co-ordinate corresponded to $z \pm$ half of the gap between the rings, depending which ring the detector was based in. The X co-ordinate on the other hand corresponded to x and y multiplied by the translational matrix that took into account fact that there are 8 detectors in each ring. The transition from one detector to the adjacent in the same ring required a rotation by 45° . Using the fact that the 300×300 detector matrix covers the physical area of 40×40 mm and using the transformation described above, the co-ordinates of a pair of events were determined. Determination of the co-ordinates of each pair of coincidence events allowed for determination of co-ordinates of a line of response (LOR). These LORs were used to construct the sinograms.

Taking the centre of the axial and trans-axial FOV as a centre of the co-ordinate system, a sinogram was generated calculating for every LOR the radial distance from the centre of the co-ordinate system and the angle between the LOR and X-axis ($0-180^\circ$). The Z co-ordinate, which is the slice the sinogram was assigned to, was found using SSRB.

3.1.5.2 Sensitivity and count-rate performance calculations

A customised program was needed to calculate sensitivity and count-rate performance results. For the sensitivity test, a text file was generated containing absolute system sensitivity for each slice corresponding to an axial co-ordinate. For the count-rate performance test a text file, which contained true, random, scatter events and scatter fraction for every acquisition file was obtained, which in turn related to decaying activity in the line source over time. In both cases the output files were then used to generate the required plots.

3.2 Assessment of CT

3.2.1 Measurements

A schematic picture of micro-CT mouse-like phantom (Computerized Imaging Reference Systems Inc., Norfolk, Virginia, USA) is shown in Figure 10.

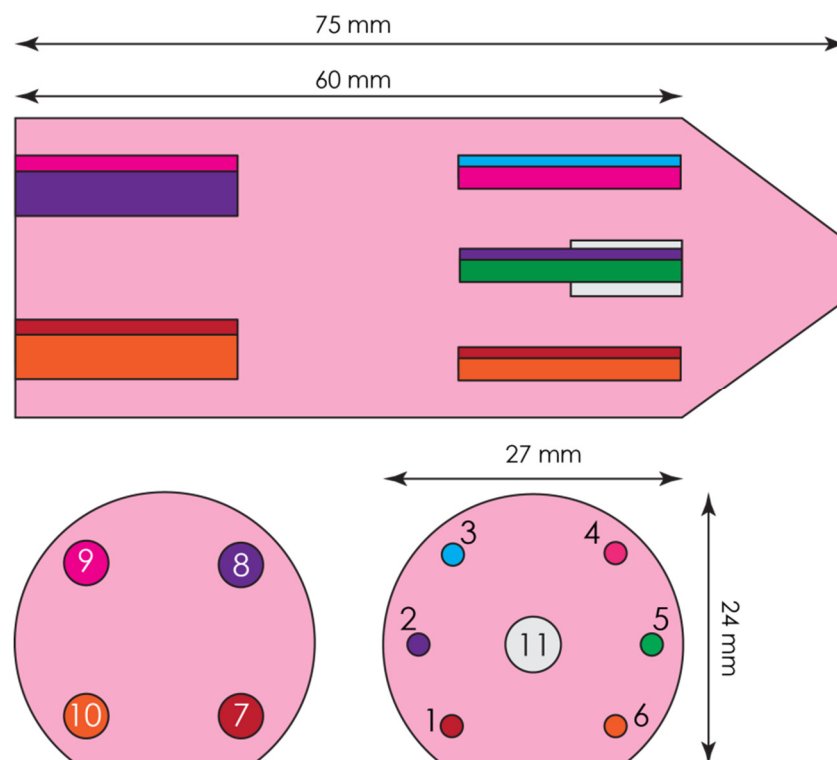


Figure 10 A schematic picture describing the geometry and the dimensions of the micro-CT phantom. The exact densities and sizes of the individual rods are given in Table 4 Micro-CT phantom specification (courtesy of CIRS Inc.)

It was made of a blend of soft-tissue equivalent polymer and hydroxyapatite (HA), the mineral found in the teeth and bones of mammals. The phantom consisted of the body (polymer equivalent to muscle tissue) and 11 rods of different sizes and densities, described in Table 4.

Table 4 Micro-CT phantom specification (courtesy of CIRS Inc.)

Feature	Tissue-like or HA Density [mg/cm ³]	Physical density [g/cm ³]	Electron density per cm ³ , ×10 ²³	Relative electron density (RED) to water	Size of the structure [mm]
Body	Muscle	1.063	3.483	1.043	60 × Ø 27
Rod 1	0	1.083	3.562	1.066	20 × Ø 2
Rod 2	50	1.115	3.655	1.094	
Rod 3	100	1.148	3.747	1.122	
Rod 4	250	1.245	4.024	1.205	
Rod 5	500	1.408	4.486	1.343	
Rod 6	750	1.571	4.948	1.481	
Rod 7	0	1.083	3.562	1.066	20 × Ø 4
Rod 8	50	1.115	3.655	1.094	
Rod 9	250	1.245	4.024	1.205	
Rod 10	750	1.571	4.948	1.481	
Rod 11	Lung (low density, inhale)	0.205	0.681	0.204	10 × Ø 5

The phantom was placed on the imaging bed and imaged according to the protocol summarised in Table 5. It consisted of all combinations of settings a user may choose before starting a CT scan: four different “quality” pre-sets, which define the number of acquired projections (“high resolution”, 1000 projections; “best”, 600; “good”, 400; “standard”, 250), two different

settings for voltage (“high”, 45 kV and “low”, 35 kV) and two settings for lamp current (called also a “dose” in the Albira software, “high”, 400 μ A and “low”, 200 μ A) . All acquisitions within a protocol were taken sequentially as described in Table 5, with no breaks between the acquisitions.

The protocol was repeated over three consecutive days. Every day then 16 images were acquired, corresponding to one of the 16 combinations of possible CT settings. Therefore, 48 images were acquired in total.

Table 5 Details of the CT protocol

Frame no	Quality	No of projections	Voltage [kV]	Current [mA]
1	Standard	250	35	0.2
2			45	0.2
3			35	0.4
4			45	0.4
5	Good	400	35	0.2
6			45	0.2
7			35	0.4
8			45	0.4
9	Best	600	35	0.2
10			45	0.2
11			35	0.4
12			45	0.4
13	High resolution	1000	35	0.2
14			45	0.2
15			35	0.4
16			45	0.4

A mouse cadaver was imaged using standard, best and high resolution quality and low voltage-high dose, high voltage-low dose and high voltage-high dose settings.

3.2.2 Data Processing and Analysis

Images were reconstructed using the Albira Reconstructor software and using FBP and three voxel sizes: $0.5 \times 0.5 \times 0.5 \text{ mm}^3$ (image matrix of $128 \times 128 \times 128 \text{ px}$), $0.25 \times 0.25 \times 0.25 \text{ mm}^3$ (image matrix of $256 \times 256 \times 256 \text{ px}$) and $0.125 \times 0.125 \times 0.125 \text{ mm}^3$ (image matrix of $512 \times 512 \times 512 \text{ px}$) giving 144 images in total for the data acquired over three days. Each image was loaded into PMOD (PMOD Technologies Ltd., Zurich, Switzerland) and 12 VOIs drawn:

- $\text{Ø}16 \text{ mm} \times 12.5 \text{ mm}$ within the body of the phantom, centrally, between the front and back rods,
- $\text{Ø}1 \text{ mm} \times 12.5 \text{ mm}$ within rods 1-6, covering the central portion of the rod,
- $\text{Ø}2 \text{ mm} \times 12.5 \text{ mm}$ within rods 7-10, positioned like above,
- $\text{Ø}2.5 \text{ mm} \times 10 \text{ mm}$ within rod 11, positioned like above.

All images were analysed using exactly the same VOIs and in the same positions.

Statistics for each VOI were obtained using PMOD. Because the densities of rods 1 and 7, 2 and 8, 4 and 9, and 6 and 10 are the same, the results for each pair were averaged. For every acquisition file each density was assigned the mean value of Hounsfield Unit (HU) measured over the three images reconstructed using different voxel sizes. All images were grouped first with respect to the day they were acquired and then with respect to distinct four current-voltage setting (i.e. 35 kV-0.2 mA, 45 kV-0.2 mA, 35 kV-0.4 mA and 45 kV-0.4 mA), regardless of how many projections were taken in order to acquire them (i.e. 250, 400, 600 or 1000).

Next, all high resolution images (i.e. acquired at “high resolution” setting and reconstructed using the smallest available voxel size, $0.125 \times 0.125 \times 0.125 \text{ mm}^3$) were loaded into AMIDE software (Loening & Gambhir, 2003). At the transverse slice positioned mid-length of the front, 2 mm rods, middle of each rod was identified and line profile in the transverse direction was generated. Similarly to

3.1.1.2 Data processing and analysis section, FWHM was noted for each rod. This was done for the images acquired at the last day.

Cadaver images were reconstructed similarly and analysed qualitatively with the attention paid to soft tissue features visible in the mouse's abdominal cavity.

3.3 Basic Animal Studies

3.3.1 Dual-tracer Bone Imaging Study

A conscious, healthy, 5-week-old male wild type mouse (22.7 g) was injected intravenously with 25.4 MBq of ^{99m}Tc -MDP (^{99m}Tc -Medronate) in 70 μl . After a 30 min uptake period the animal was anaesthetised using a mixture of isoflurane and medical air (5% upon induction and 3% thereafter). The tail vein was cannulated and secured using tissue glue. The mouse was placed on the imaging bed and the SPECT acquisition was started (two beds, single-pinhole collimator, 45 s per projection and 60 mm FOV). After the SPECT scan was finished, 3.90 MBq of ^{18}F -NaF was administered intravenously using the cannula and a 120 min dynamic PET scan was started (8 \times 15 s, 2 \times 30 s, 2 \times 60 s, 1 \times 120 s, 1 \times 180 s, 10 \times 5 min, 6 \times 10 min). A two bed CT scan followed immediately after the PET scan (400 projections, high current, low voltage). The timeline of the study is shown in Figure 11. The animal remained anaesthetised from the time of cannulation until the end of CT scan, i.e. for 4 hours and recovered without problems.

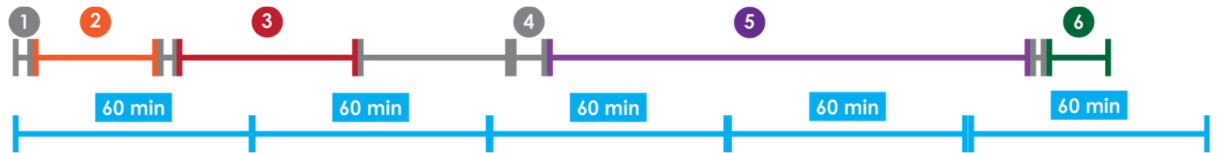


Figure 11 Timeline of the dual-radiotracer (^{99m}Tc -MDP and ^{18}F -NaF) experiment: 1) i.v. dose of ^{99m}Tc -MDP; 2) uptake of ^{99m}Tc -MDP; 3) SPECT scan; 4) i.v. dose of ^{18}F -NaF; 5) dynamic PET scan; 6) CT scan. Animal was anaesthetised from the beginning of SPECT scan until the end of CT scan (total of 4 hours) and recovered without problems.

A second mouse study was performed on a healthy, 15-week-old male wild type mouse (37.4 g), using a similar protocol as above however the mouse was anaesthetised and cannulated prior to an i.v. injection of 54.84 MBq of ^{99m}Tc -MDP and remained anaesthetised throughout the whole study. After 38 min uptake SPECT scan commenced (FOV 80, 22.5 min per bed, 2 beds). Dynamic PET acquisition started right after the SPECT scan and following an injection of 3.50 MBq of ^{18}F -NaF. Compared to previous study, the protocol was shortened to 90 min (5×1 min, 5×3 min, 4×5 min, 5×10 min). Upon the end of PET scan, CT acquisition started (400 projections, high current, low voltage, 2 beds).

3.3.2 Data Processing and Analysis

In both cases:

- the frames of dynamic PET scan were reconstructed using MLEM algorithm, 12 iterations, $0.6 \times 0.6 \times 0.8 \text{ mm}^3$ voxel size, $130 \times 130 \times 100$ px image matrix size;
- SPECT image was reconstructed using OSEM algorithm, sub-set 4, 3 iterations, $0.65 \times 0.65 \times 0.65 \text{ mm}^3$ voxel size, $100 \times 100 \times 165$ px image matrix size;
- CT image was reconstructed using FBP algorithm, $0.25 \times 0.25 \times 0.25 \text{ mm}^3$ voxel size, $256 \times 256 \times 474$ px image matrix size.

Images were loaded into PMOD. For the first mouse, the last three frames of the PET scan were averaged. Then all images from the experiment were aligned

manually in the Fusion tool. Each image was rotated by 30° around the z-axis and the maximum intensity projections (MIPs) were generated.

For the second mouse, the reconstructed dynamic PET image was loaded into the View tool in PMOD. Next, using automatic 3D hot pixel selection tool volumes of interests (VOIs) were drawn around major joints (patellae and clavicles), kidneys, skull and spinal column. Time-activity curves were generated. Additionally, MIPs were produced for different times through the PET scan.

4 Results

4.1 NEMA Results for Albira PET

Results in this section, including some of the text and figures, were published in (Pajak *et al.*, 2016).

4.1.1 Spatial Resolution

Figure 12 presents example images of the point source acquired at the axial centre and at quarter of the axial field of view reconstructed using prescribed by the NEMA standard, SSRB and FBP algorithms. Using these, in the dual-ring configuration it was not possible to reconstruct images of a point source positioned along the axial centre of the FOV, because the centre of the FOV corresponds to the 14.4 mm gap between the two detection rings. This highlights the challenges of 2D FBP when it's applied to images acquired on PET systems implementing non-standard geometry. For this reason, in this part of the evaluation MLEM reconstruction algorithm (default in the Albira's reconstruction software) was used.

The comparison between 30 and 50% energy window (measured as Full Width at Half Maximum, FWHM and Full Width at Tenth Maximum, FWTM - as defined in Figure 7) is shown in Figure 13. Spatial resolution as the function of radial offset for both energy windows remained nearly the same at both axial offsets and the differences between the values acquired at both energy windows were minimal. One can also observe that the spatial resolution was better at the quarter of the FOV, which is due to the proximity of the ring centre as opposed to the centre of the scanner, which overlaps with the gap between the rings.

The best spatial resolution was measured at $\frac{1}{4}$ of the axial FOV, at 5 mm radial offset and was 1.55, 1.60 and 1.42 mm in radial, tangential and axial direction, respectively.

The detailed spatial resolution results for both, SSRB+FBP and MLEM reconstruction methods for the 30% energy window are gathered in Table 6. This

table highlights the portion of results that cannot be derived following NEMA-prescribed algorithms.

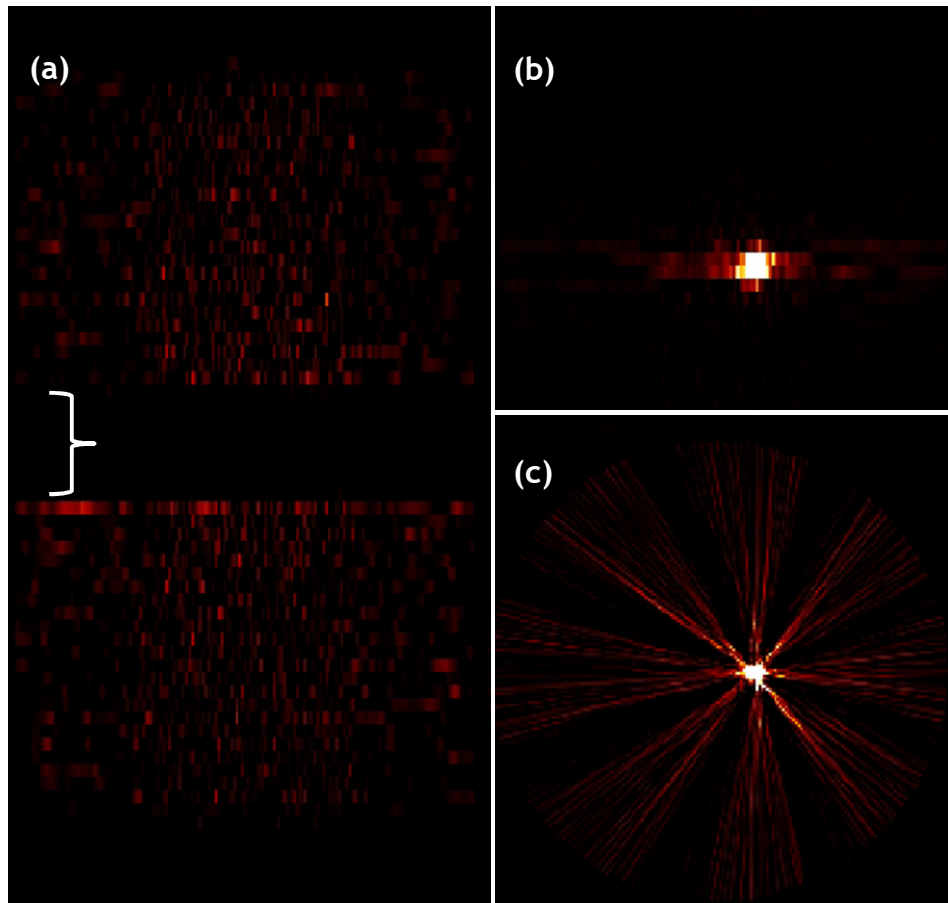


Figure 12 Images of a point source acquired by the Albira at the 5 mm radial offset and: the centre (a) and quarter (b, c) of the axial field of view. All images are reconstructed using SSRB and FBP. a) The gap between the rings (denoted with a curly brace) is clearly visible on the coronal slice; b) at quarter of the axial field of view, the image of the point is visible; c) octagonal geometry causes streak artifacts on images reconstructed using FBP.

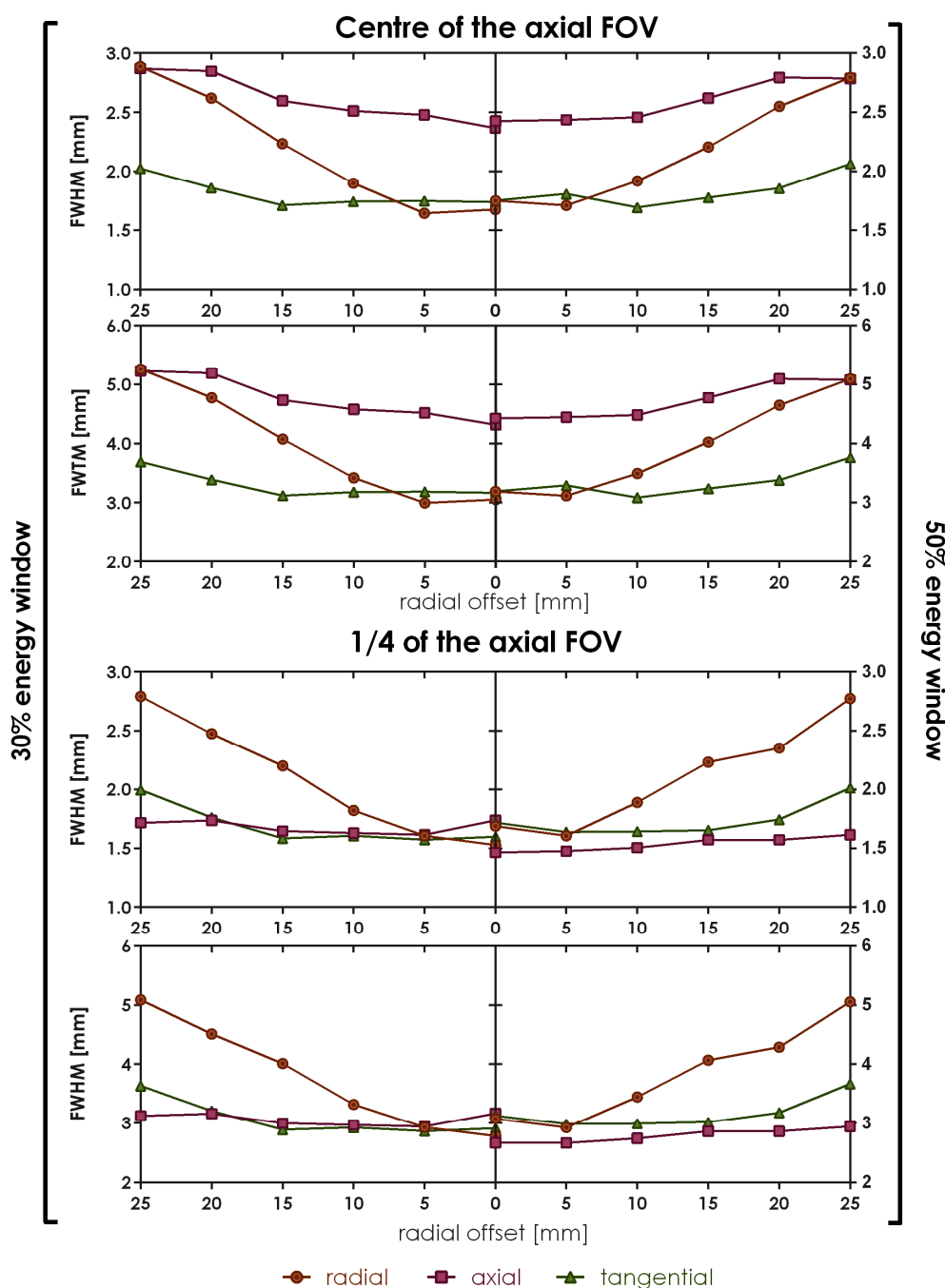


Figure 13 Spatial resolutions obtained on the 2-ring Albira PET system shown as Full Width at Half or Tenth Maximum in radial, axial and tangential directions measured at the axial centre and quarter of the field of view (FOV) expressed as a function of radial offset. Graphs on the left represent 50% energy window (255-767 keV) and on the right, the 30% one (358-664 keV).

Table 6 Spatial resolution results using 20 iterations MLEM and FBP along with the pixel sizes and slice thicknesses used for both algorithms (Pajak *et al.*, 2016)

Reconstructed image pixel size (mm): 0.5 (MLEM) / 0.33 (FBP)													
Slice thickness (mm): 0.5 (MLEM) / 0.33 (FBP)													
At axial centre													
		0 mm		5 mm		10 mm		15 mm		20 mm		25 mm	
Algorithm		FWHM	FWTM	FWHM	FWTM	FWHM	FWTM	FWHM	FWTM	FWHM	FWTM	FWHM	FWTM
Radial	MLEM	1.72	3.13	1.68	3.06	1.93	3.52	2.24	4.08	2.58	4.71	2.81	5.12
	FBP	N/A											
Tangential	MLEM	1.70	3.10	1.75	3.19	1.63	2.97	1.68	3.07	1.74	3.17	1.95	3.55
	FBP	N/A											
Axial	MLEM	2.45	4.47	2.44	4.44	2.44	4.45	2.62	4.78	2.81	5.11	2.77	5.05
	FBP	N/A											
At ¼ axial FOV from centre													
Radial	MLEM	1.52	2.78	1.55	2.83	1.86	3.39	2.13	3.89	2.33	4.25	2.79	5.08
	FBP	1.78	3.24	1.92	3.50	2.59	4.73	5.14	9.37	6.81	12.42	7.91	14.41
Tangential	MLEM	1.69	3.07	1.60	2.91	1.58	2.8	1.65	3.01	1.66	3.02	1.95	3.55
	FBP	1.72	3.13	1.31	2.38	1.57	2.87	1.14	2.07	0.90	1.63	1.01	1.84
Axial	MLEM	1.45	2.64	1.42	2.59	1.48	2.69	1.55	2.83	1.52	2.78	1.62	2.96
	FBP	2.47	4.51	2.59	4.72	2.69	4.89	2.59	4.72	3.26	5.95	3.06	5.57

4.1.2 Sensitivity

Figure 14 presents the axial absolute sensitivity profile for the 2-ring Albira PET for two energy windows: 50% (255-767 keV) and 30% (358-664 keV).

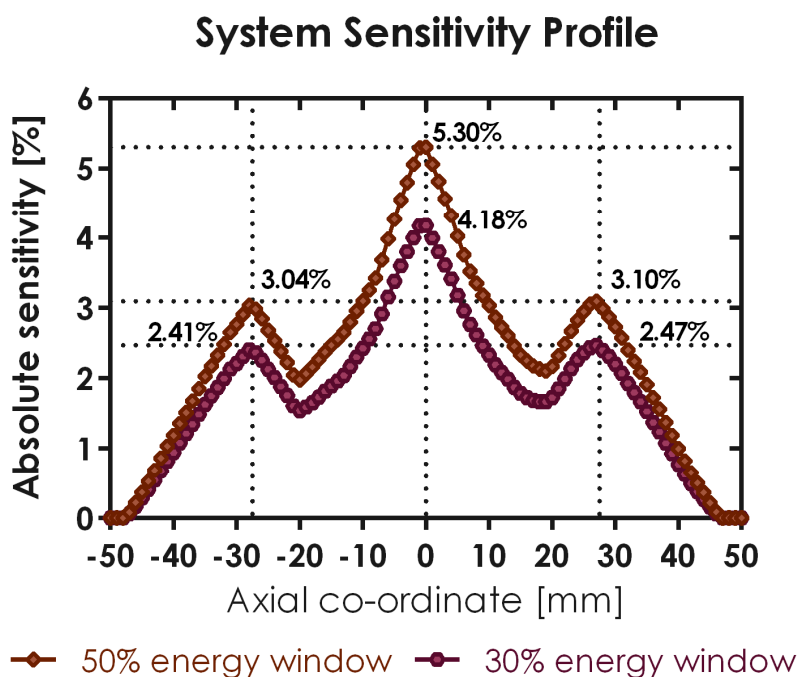


Figure 14 Axial sensitivity profile of the 2-ring Albira PET scanner measured using two energy windows: 255-767 keV (50%) and 358-664 keV (30%).

The peak absolute sensitivity was 5.30% and was measured in the axial centre of the scanner and at the wider, 50% energy window. Two smaller peaks can be seen marking the position of the middle of each ring on both sides of the central peak. Over the central 7 cm, which NEMA describes as a “mouse region”, the average absolute sensitivity was 3.0%. The “rat region” encompasses 15 cm, which is more than the axial FOV of 2-ring Albira PET and therefore the average absolute sensitivity over this region (and over the whole FOV) was 2.33%.

4.1.3 Count-rate Performance

The scatter fraction for the mouse- and rat-like phantom was 9.9% and 22%, respectively. The overall count rate performance for both phantoms is presented on Figure 15. The maximum noise-equivalent count rate, $R_{NEC, peak}$ was 72 kcps and was measured at 205.4 kBq/ml for the mouse-like phantom. For rat-like phantom this value was equal to 42 kcps at 39.9 kBq/ml.

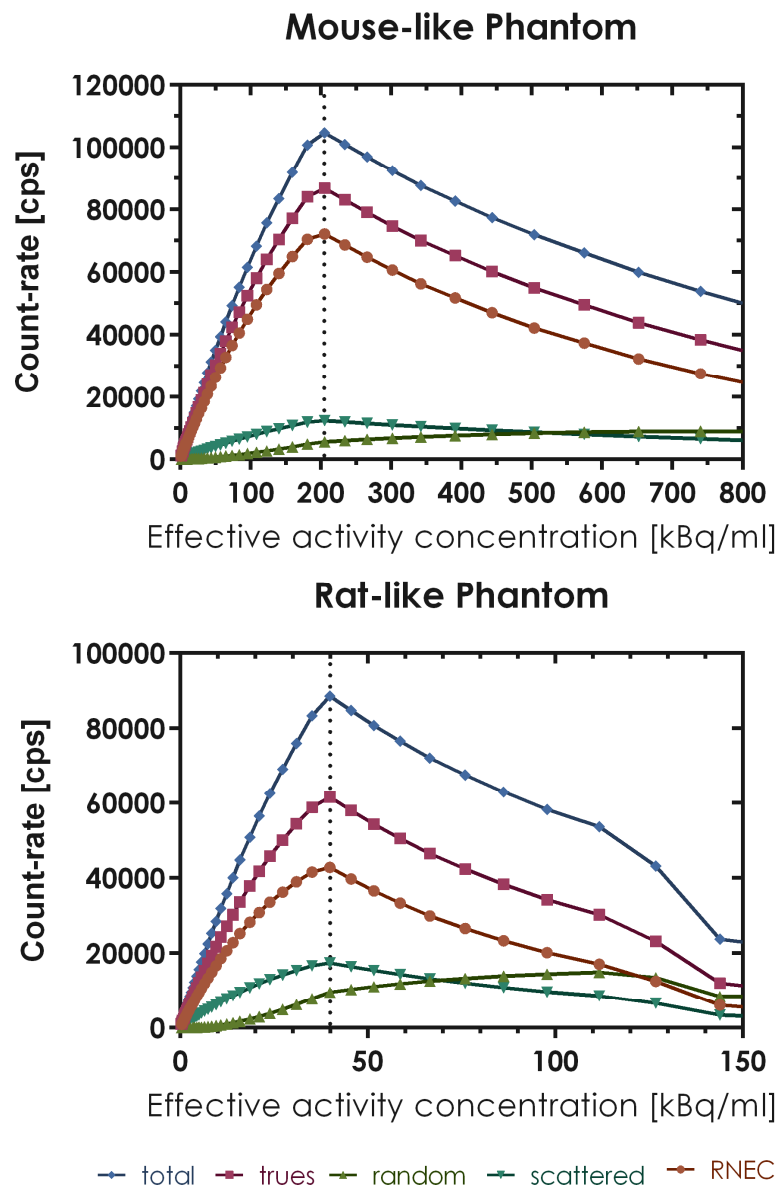


Figure 15 Count-rate performance measured on the 2-ring Bruker Albira PET system using mouse- and rat-like phantoms filled with ^{18}F .

4.1.4 Image Quality

The results of the analysis of the image quality phantom study reconstructed with 20 iterations of MLEM are given in

Table 7 and Table 8.

Table 7 Recovery Coefficients (RCs) for rods of different diameters measured using NEMA Image Quality phantom and the 2-ring Bruker Albira PET system (Pajak *et al.*, 2016)

Rod diameter	Recovery co-efficient	%STD
1 mm	0.05	29.0
2 mm	0.30	14.5
3 mm	0.66	14.8
4 mm	0.77	10.2
5 mm	0.90	8.5

Table 8 Accuracy of corrections calculated for the 2-ring Bruker Albira PET system for water- and air-filled chambers in the NEMA Image Quality phantom (Pajak *et al.*, 2016)

Region	Spill-over ratio	%STD
Water-filled cylinder	0.219	12.3
Air-filled cylinder	0.139	14.1

The recovery co-efficients (RCs) for the rods of different diameters ranged from 0.05 to 0.90 and the %STD within the uniformity region was 4.9%. The relation between the reconstruction parameters (namely the number of iterations used) and RCs and spill-over ratios (SORs) is shown on Figure 16 and Figure 17, respectively. For rods with a diameter of 3 mm or more, the maximum RCs were reached at 16 iterations. The RC for the 2 mm rod reached a plateau of approx. 0.45 at around 40 iterations, while for the 1 mm rod the RC slowly increased with increasing number of iterations and eventually approached 0.2 at 100 iterations. SORs for air- and water-filled chambers improved with increasing numbers of iterations, although the decrease was quicker for air-filled chamber. 12 iterations were required to achieve maximum RC for the biggest rod, while 20 iterations seem to give good balance between the RCs for all the rods and improved (i.e. lower) SORs. However, to maximise RCs for the two smallest rods and to improve SORs even further 40-60 iterations would be required.

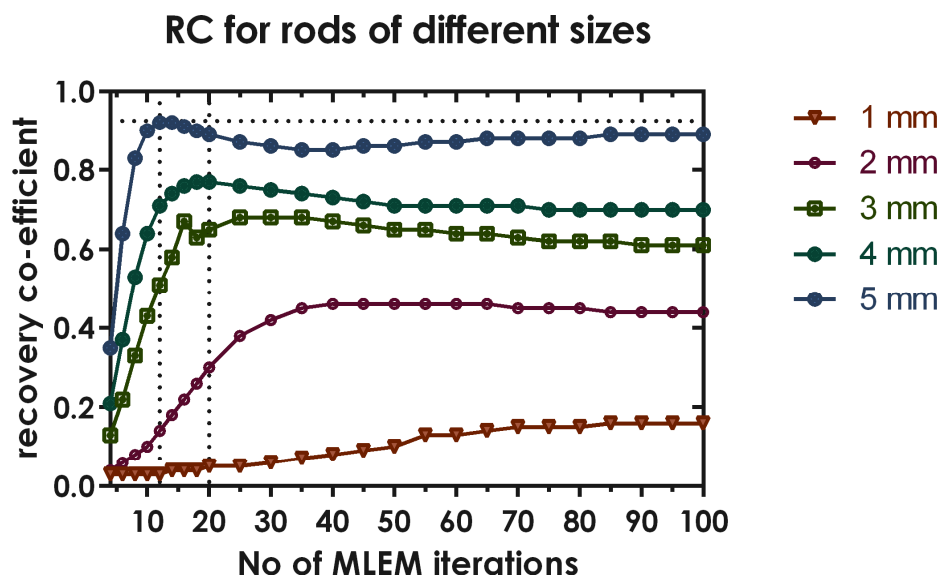


Figure 16 RCs determined for the 2-ring Albira PET for all rods as a function of the number of MLEM iterations. Marked are 12 and 20 iterations.

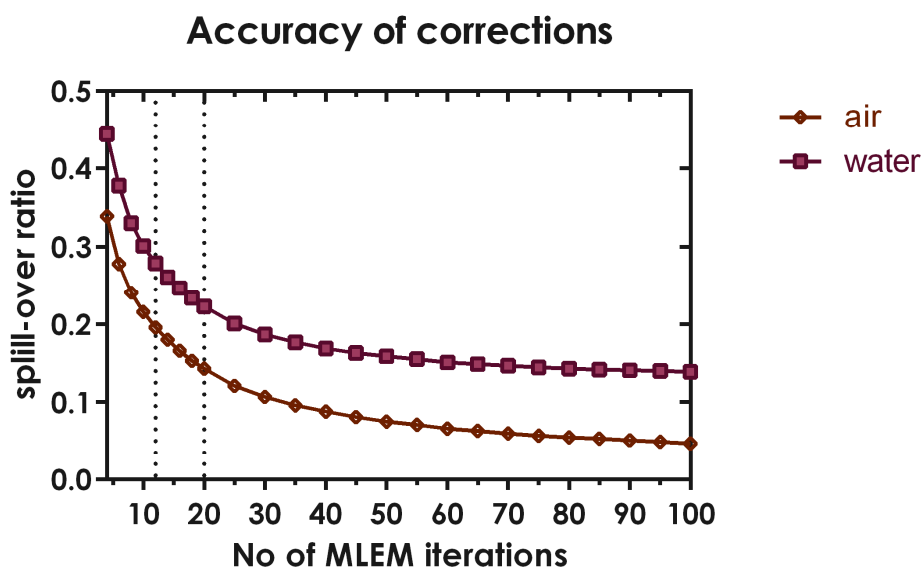


Figure 17 Accuracy of corrections for water- and air-filled chambers using the 2-ring Bruker Albira PET as a function of the number of MLEM iterations. Marked are 12 and 20 iterations.

4.2 CT Phantom Results

4.2.1 Stability of the System and Basic Performance

Figure 18 presents the results for three out of three out of four available voltage-current settings, which share common characteristics

By comparing data obtained over three subsequent days of acquisitions there was no difference between the Hounsfield units (HU) measured for images acquired using different number of projections between day 2 and day 3. On Day 1, the high voltage-low current setting showed significant variation between the HUs measured for different image quality settings. Over all three days, the low density (lung-like) structure within the phantom produced similar HU values for low voltage-high current and high voltage-low current settings (-579 HU and 555 HU, respectively averaged over three days), while the measured HU values for high

voltage-high current settings were about half of the low voltage-high current and high voltage-low current setting measurements (-291 HU).

Another way of looking at system stability is to group the data by the voltage-current settings combinations shown on Figure 19. The low voltage-low current (35 kV - 0.2 mA) setting produced a negative contrast for bone structures leading to very high negative (over -10 000 HU) measured values. Hounsfield numbers for dense bone (rod 7, 750 mg/cc HA) for high voltage-low current (45 kV - 0.2 mA) setting were almost twice as high as low voltage-high current (35 kV - 0.4 mA) and high voltage-high current (45 kV - 0.4 mA) settings: 1790 HU vs. 1051 HU and 1139 HU, respectively. This highlights that measurements for day 1 had the biggest variation not only within the certain voltage-current settings but also when using different reconstruction settings. The variation attributed to different reconstruction settings was more prominent as the density of the structure in the phantom increases, especially for the low current settings.

Since the rods (1-6) were of a known diameter (2 mm), it is possible to determine the spatial resolution of the scanner. Figure 20 summarises the FWHM, as a measure of spatial resolution of the images acquired on day 3 of the experiment and reconstructed on high resolution FBP setting (0.125×0.125×0.125 mm³ voxel size). Rod 1, which contained no hydroxyapatite (HA) and rod 3, showed of the biggest variation of measured FWHM values. Rod 2 (50 mg/cc of HA) was hardly (if at all) distinguishable from the body of the phantom. In most cases, it was impossible to measure its apparent diameter and hence it is omitted from the summary below. The remaining rods had FWHM values of between 2.1 mm down to 1.7 mm for rod 6.

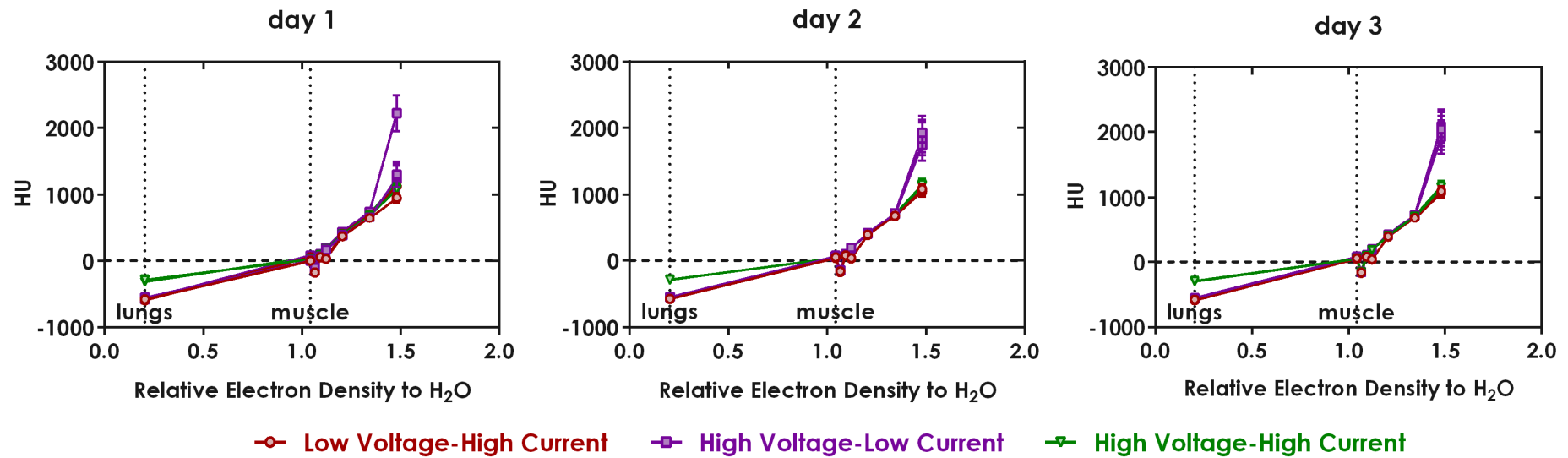


Figure 18 Three lamp settings (low voltage-high current, high current-low voltage and high voltage-high current) over the period of three days. For each voltage-current combination, image of the phantom was acquired using different numbers of projections (250, 400, 600 or 1000). These are superimposed on the graph and are represented with points and lines, which colour corresponds to the voltage-current setting used. Each acquired image was reconstructed using high, medium and low FBP settings. Therefore, for each voltage-current-number of projection combination of settings, three measurements were obtained. This value is shown as individual points on the graphs. The error bars represent the standard error of the mean of this value.

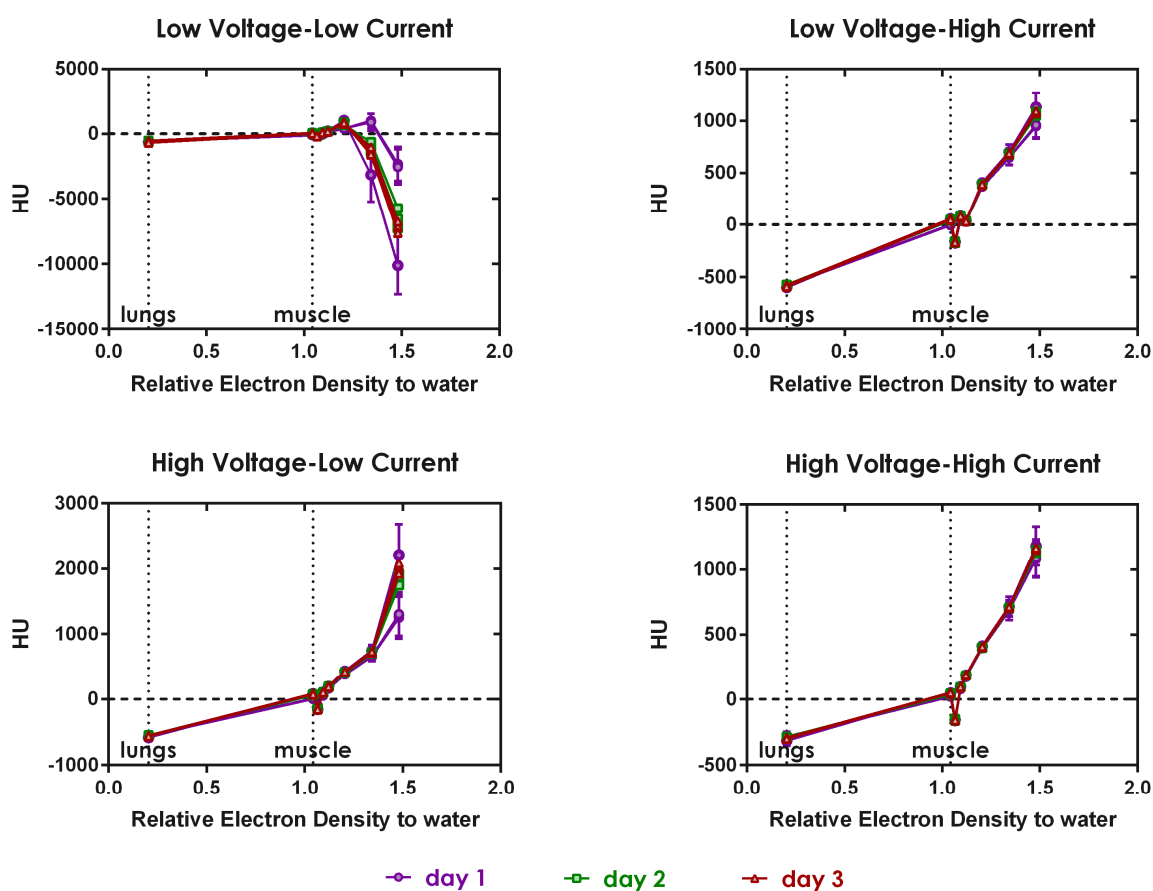


Figure 19 Summary of the results for all combinations of voltage and current settings for the data acquired over three consecutive days. Lines are colour coded for measurement taken on a different day. Every individual line represents the measurements for a different image quality setting and is an average of the measurements for the same setting that was reconstructed using three different FBP settings. An individual point represents a mean and standard error of the mean.

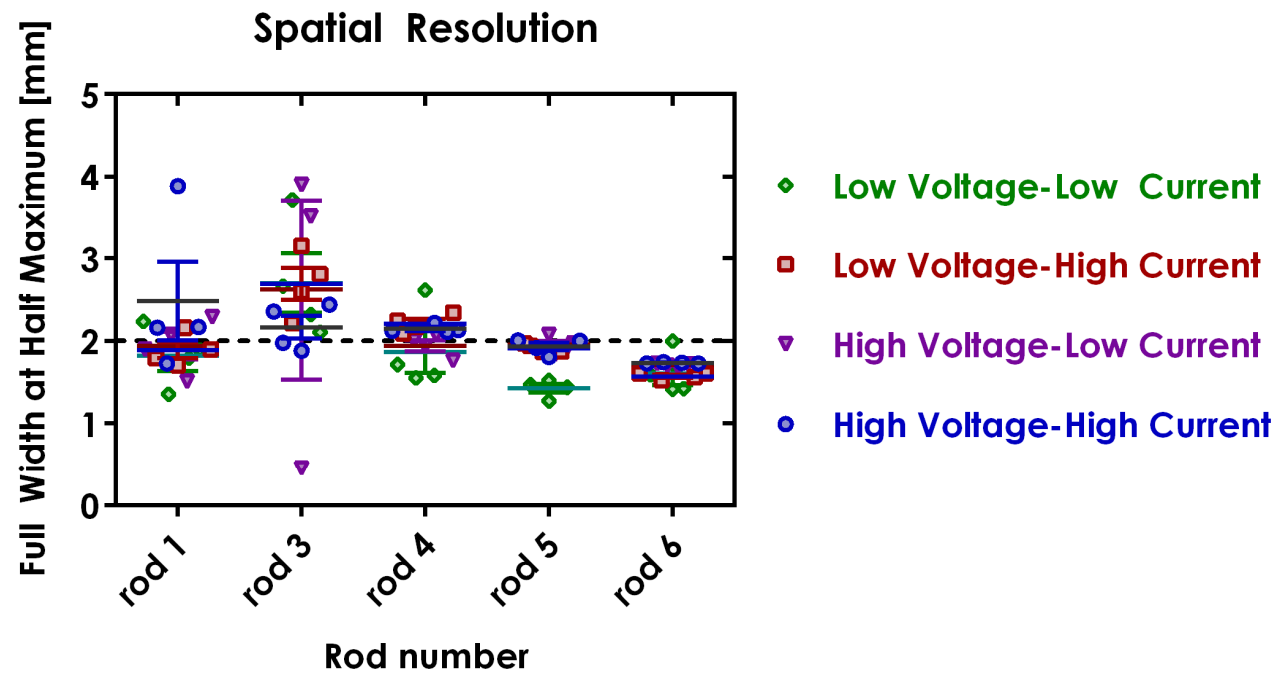


Figure 20 The spatial resolution measured as a Full Width at Half Maximum on transverse slice in the middle of the front rods region. The data were obtained using images acquired at day 3 and reconstructed using the smallest available voxel size (0.125×0.125×0.125 mm³). The known physical diameter of rods 1-6 is 2 mm. The contrast between the body of the phantom and rod 2 was too poor for the rod to be clearly distinguished; therefore, is omitted in the above summary.

4.2.2 Impact of Acquisition Settings on Image Quality

Figure 21 shows a transverse slice through the middle of the region of the phantom (the same one in every case) containing rods 1-6 and rod 11 reconstructed on the medium FBP settings ($0.25 \times 0.25 \times 0.25$ mm³ voxel size). Images were acquired on day 1 using all possible combinations of the available CT settings.

The low voltage-low current setting (35 kV - 0.2 mA), including the high-resolution setting (1000 projections), showed a strong beam hardening. On the other end, high voltage-high current setting (45 kV - 0.4 mA) also showed some beam hardening around rod 11, but even using the standard quality (250 projections) setting one can delineate all the rods (although rod 2 was hardly distinguishable). The low voltage-high current and high voltage-low current settings produced similar images, however, the low voltage-high current resulted in better contrast between rods 1 and 3 (0 vs. 100 mg/cc HA). Three out of four quality settings (“standard”, “good” and “best”) for the low voltage-high current and high voltage-low current settings suffered nearly equally from ring artefacts visible around rod 3. This feature seemed to disappear on the high-resolution setting. Out of all combinations, the low voltage-high current and high resolution setting produced the most uniform-looking body of the phantom with all rods (except for rod 2) clearly delineated.

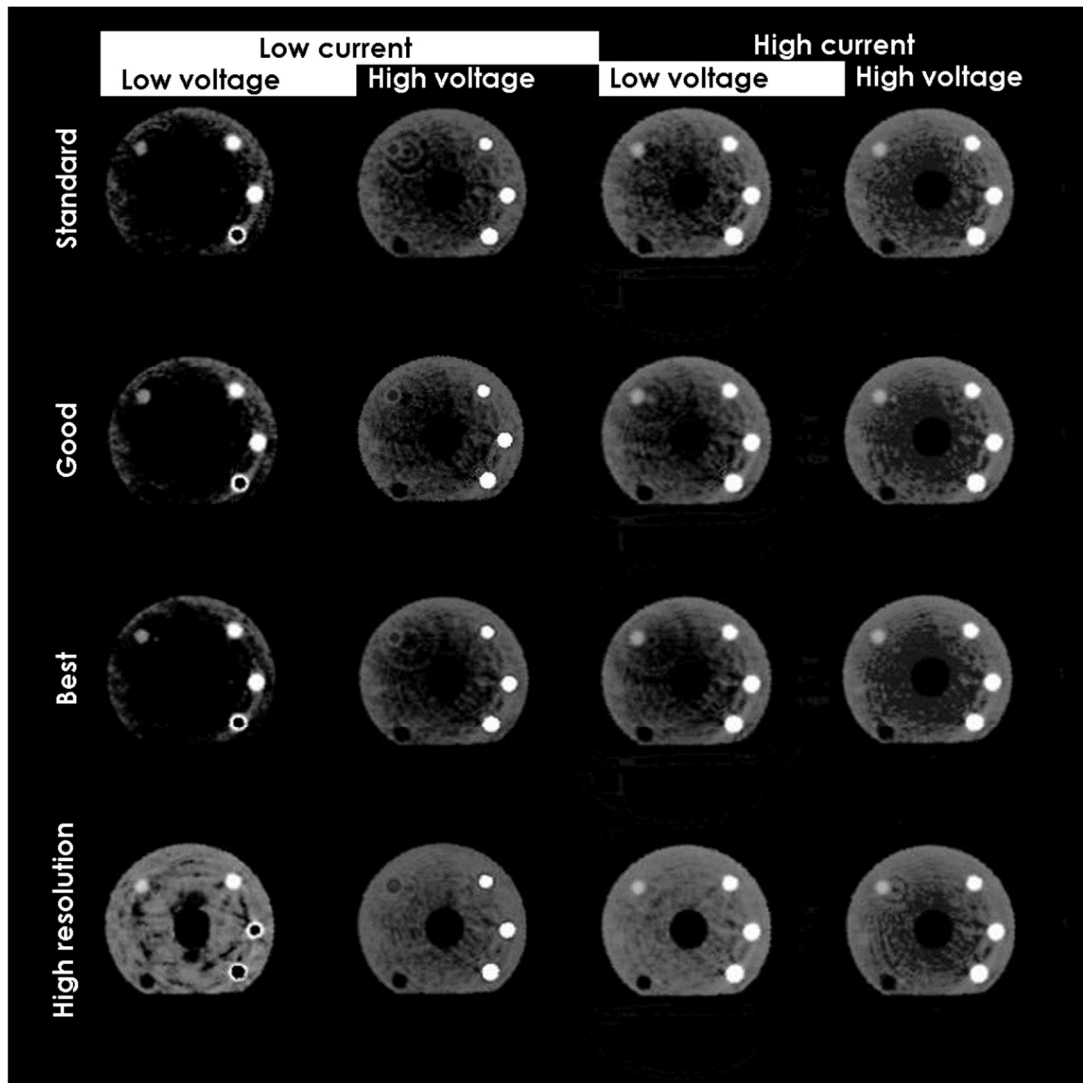


Figure 21 Representative transverse slices through the region of the phantom containing rods 1-6 and 11. Each image was acquired using one of the 16 available settings combinations and reconstructed using FBP and $0.25 \times 0.25 \times 0.25 \text{ mm}^3$ voxel size. The orientation of the rods on the slice is consistent with the one shown on Figure 10, i.e. rod 1 is positioned at the bottom-left part of the slice and the rods are numbered clockwise. Rod 11 is in the centre. The scale used is -30 to 300 HU.

4.2.3 Impact of Reconstruction Settings on Image Quality

Figure 22 and Figure 23 present the summary of the investigation of how the chosen reconstruction settings impacted the apparent image quality. In both figures the images presented were acquired during day 3 of experiment. They both present all available voltage and current combinations and show the same transverse slice through the middle of rods 1-6 and 11 against three available FBP settings (i.e. different voxel sizes) used during the reconstruction. The difference between Figure 22 and Figure 23 is the image quality setting used, the former being acquired using high resolution setting (1000 projections) and the latter the standard quality (250 projections). The scale used is from -30 to 300 HU.

When comparing the images above it can be seen that there is hardly any difference in image quality whether using 250 or 1000 projections when reconstructing images using medium or high FBP settings. However, beam hardening was slightly less prominent when using a higher number of projections and to certain degree this image artefact gets compensated for when using high FBP settings at reconstruction. Again, the images acquired using the low voltage-high current settings produced images that were the most accurate representation of the phantom.

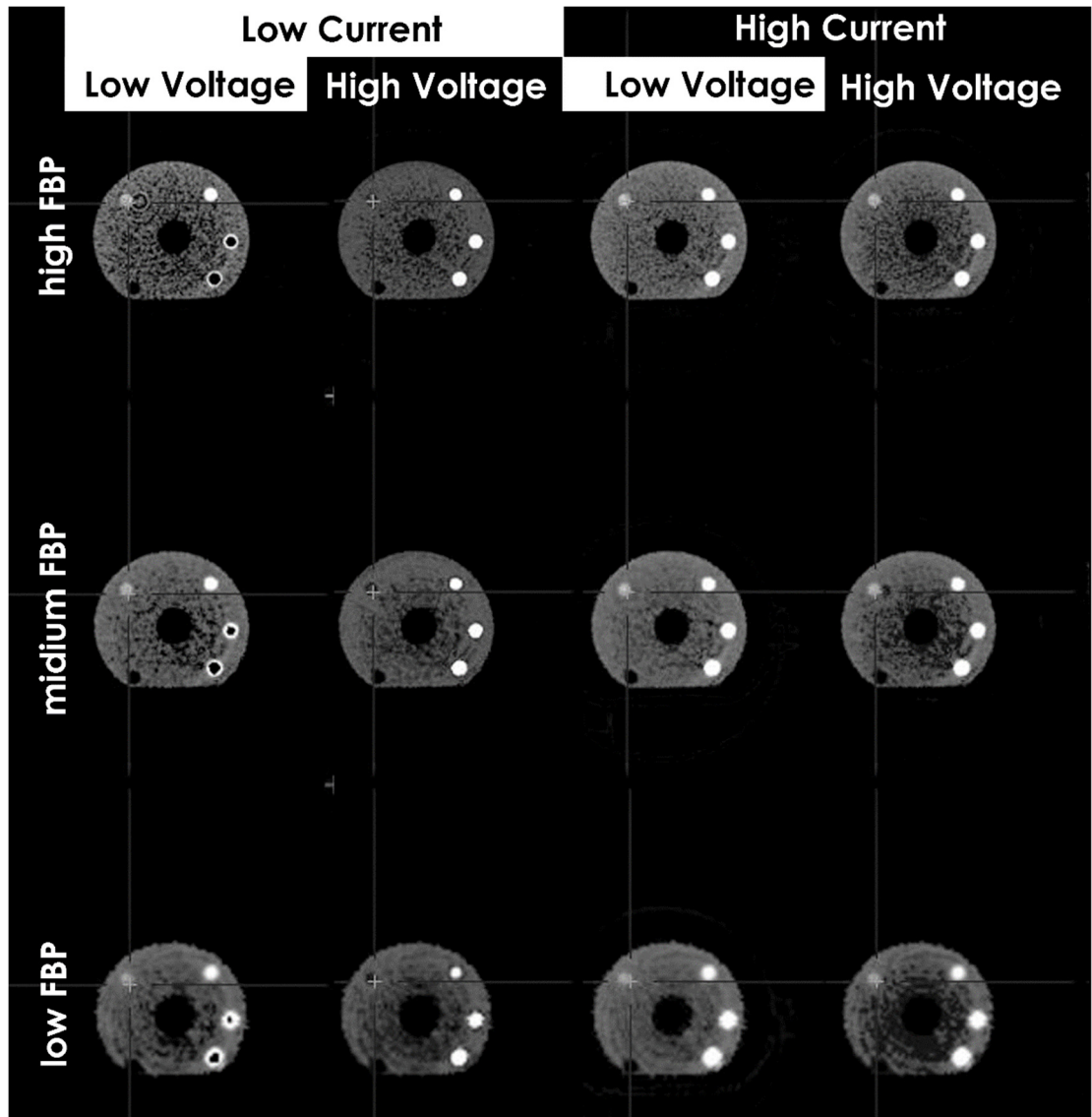


Figure 22 Images acquired using the high-resolution setting (1000 projections) and four available combinations of current and voltage settings. Rows from top to bottom present the same transverse slice through rods 1-6 and rod 11 reconstructed using: high, medium and low FBP settings corresponding to $0.125 \times 0.125 \times 0.125 \text{ mm}^3$, $0.25 \times 0.25 \times 0.25 \text{ mm}^3$ and $0.5 \times 0.5 \times 0.5 \text{ mm}^3$ voxel size, respectively.

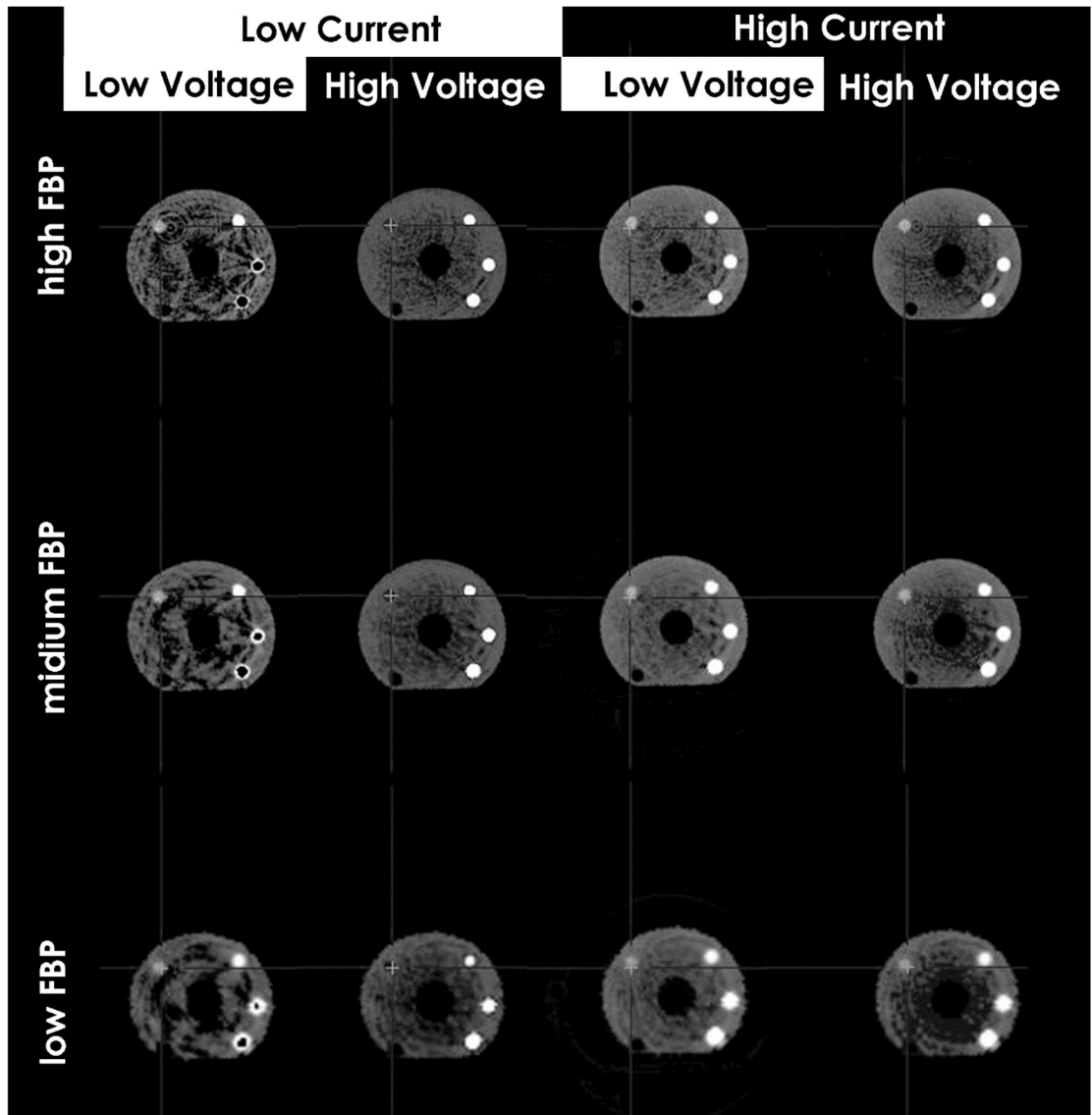


Figure 23 Images acquired using the standard quality setting (250 projections) and four available combinations of current and voltage settings. Rows from top to bottom present the same transverse slice through rods 1-6 and rod 11 reconstructed using: high, medium and low FBP settings corresponding to $0.125 \times 0.125 \times 0.125 \text{ mm}^3$, $0.25 \times 0.25 \times 0.25 \text{ mm}^3$ and $0.5 \times 0.5 \times 0.5 \text{ mm}^3$ voxel size, respectively.

4.2.4 Example Animal Images

Representative images of a cadaver acquired using the best quality setting (600 projections) using either high current (0.4 mA) and low voltage (35 kV), high current and high voltage (45 kV) or low current and high voltage are shown in Figure 24, Figure 25 and Figure 26, respectively. The data were reconstructed using the three FBP settings ($0.5 \times 0.5 \times 0.5 \text{ mm}^3$, $0.25 \times 0.25 \times 0.25 \text{ mm}^3$ and $0.125 \times 0.125 \times 0.125 \text{ mm}^3$ voxel sizes), from top to bottom of the image, respectively. The display window was set to -30 to 300 HU to show soft tissue as well as bone structures.

There was little difference between high and medium FBP setting ($0.125 \times 0.125 \times 0.125 \text{ mm}^3$ vs. $0.25 \times 0.25 \times 0.25 \text{ mm}^3$ voxel size). Furthermore, low voltage-high current setting produced the best representation of the soft tissue out of the three settings presented, although delineation of different organs was not possible in most cases.

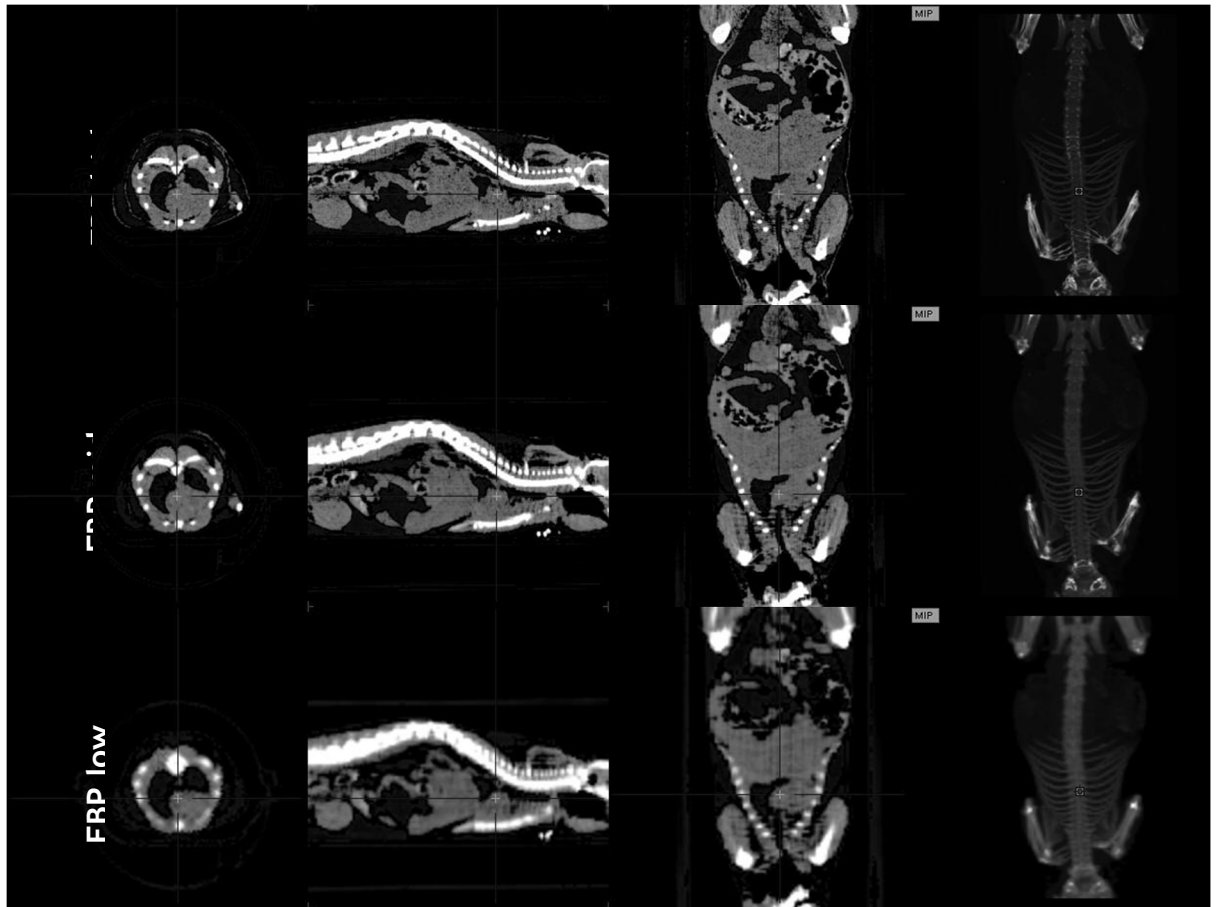


Figure 24 Representative image of a cadaver acquired using the Best quality setting (600 projections), the high current (0.4 mA) and low voltage (35 kV) setting and reconstructed using 3 different FBP settings. The display window was set from -30 to 300 HU, so soft tissue is visible. The images in columns from left to right show: transvers, sagittal and coronal slices and the last column shows maximum intensity projection (MIP).

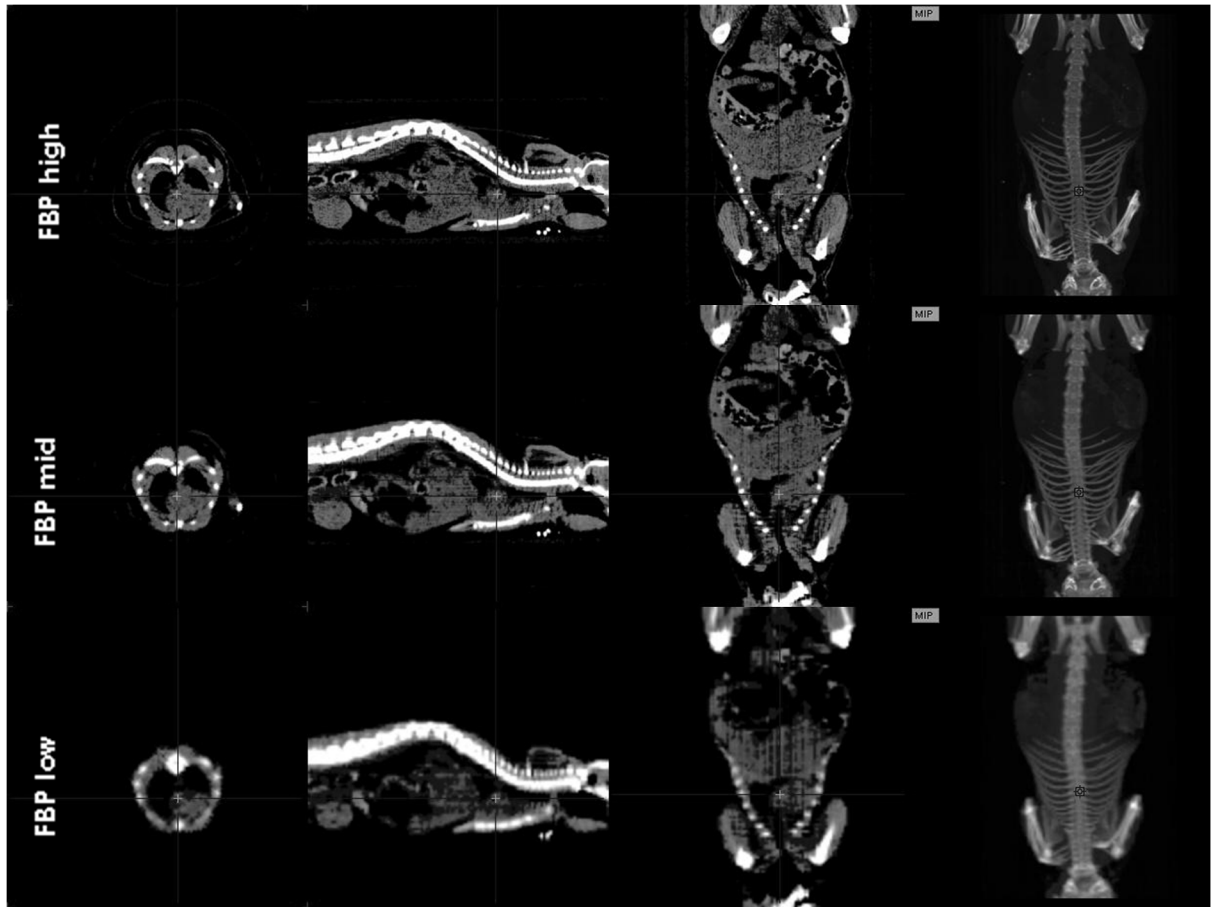


Figure 25 Representative image of a cadaver acquired using the Best quality setting (600 projections), high current (0.4 mA) and high voltage (45 kV) setting and reconstructed using 3 different FBP settings. The display window was set from -30 to 300 HU. The images in columns from left to right show: transverse, sagittal and coronal slices and the last column shows maximum intensity projection (MIP).

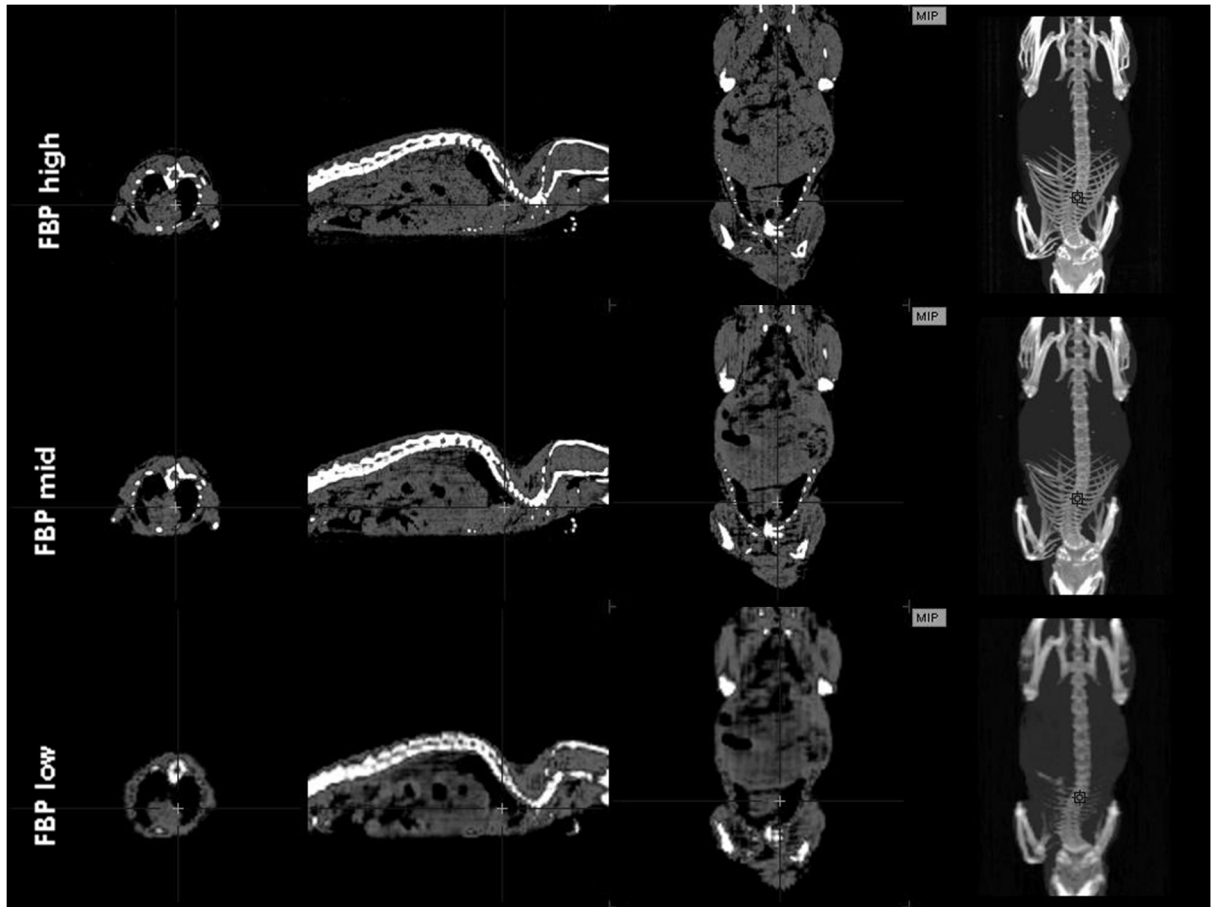


Figure 26 Representative image of a cadaver acquired using the Best quality setting (600 projections), low current (0.2 mA) and high voltage (45 kV) setting and reconstructed using 3 different FBP settings. The display window was set from -30 to 300 HU. The images in columns from left to right show: transvers, sagittal and coronal slices and the last column shows maximum intensity projection (MIP).

4.3 Basic Animal Studies

The ability of the Albira scanner to perform a dual tracer imaging study is highlighted in Figure 27, showing the maximum intensity projection images for both PET and SPECT bone imaging modalities obtained from a mouse (conscious during ^{99m}Tc -MDP uptake period). The CT image provided anatomical co-registration for the nuclear imaging modalities. PET images obtained at different time points of the dynamic scan are summarised in Figure 28, highlighting the ability to perform dynamic imaging and determination of the optimal imaging period for a given radiopharmaceutical. As an example, Figure 29 presents a time-activity curve for the ^{18}F -NaF dynamic study of the second mouse.

PET and SPECT images in Figure 27 demonstrated the similar retention of the ^{18}F -throughout the body, although the SPECT image appeared to show more vertebrae and ribs). Both images showed smaller joints in front and hind limbs. Additionally, the PET image showed the hip and mandibular joints and sternum with improved delineation than the SPECT image. When compared with the CT image, both the PET and SPECT images accurately represented the skeletal structure of the mouse. The three images are shown in a slightly different axial field of view and a small gap was seen in the SPECT image corresponding to the split between two separate acquisitions at two beds positions. This was the result of the inaccurate stitching during the reconstruction process, which was fixed in later releases of the manufacturer software.

Both Figure 28 and Figure 29 show the accumulation of ^{18}F -NaF and its wash-out over the period of the scan. Maximum accumulation of the ^{18}F -NaF in the skull and spine was seen at 30 minutes post injection. However, at 60 minutes the joints achieved a maximum retention of ^{18}F -NaF, while the uptake in the kidneys was further reduced compared to that seen at 30 minutes. At 90 minutes there was still enough ^{18}F -NaF within the skeleton to produce good quality image, i.e. allowing the distinction of all the major joints and skeletal structure.

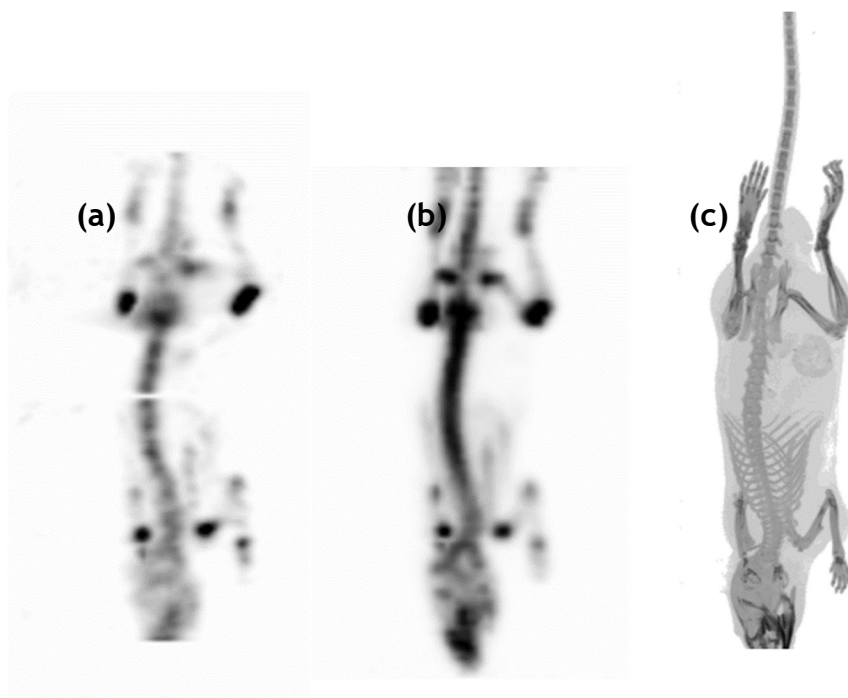


Figure 27 Maximum Intensity Projection (MIP) in dual-radiotracer experiment; a) ^{99m}Tc -MDP, b) ^{18}F -NaF PET (Pajak *et al.*, 2016), c) CT generated for the first mouse.

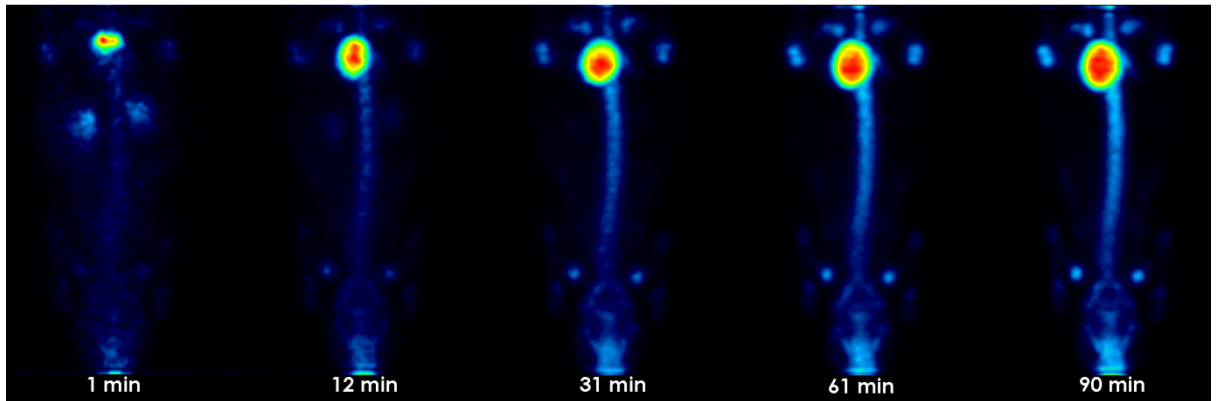


Figure 28 Summary of 90 min dynamic PET acquisition: Maximum Intensity Projection (MIP) following the intravenous injection with 3.50 MBq of ^{18}F -NaF at $t=0$ min.

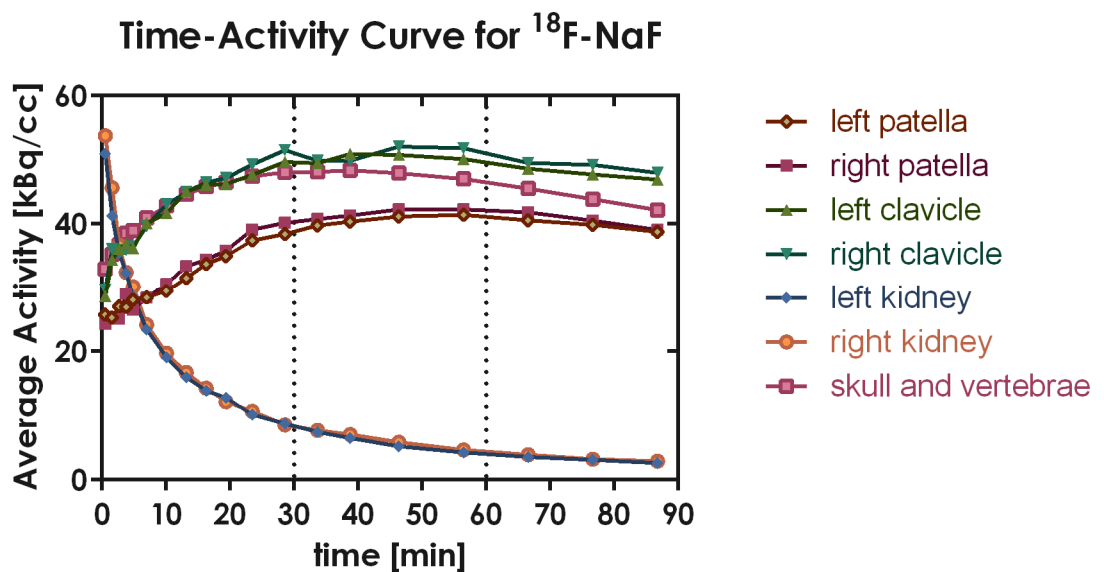


Figure 29 Time-Activity Curves showing accumulation, retention and clearance of ^{18}F during dynamic PET scan following the intravenous injection of 3.50 MBq of ^{18}F -NaF at $t=0$.

5 Discussion

5.1 Performance Evaluation of 2-ring Albira PET

5.1.1 NEMA NU4-2008 Overview

NEMA NU4-2008 states guidelines for assessing performance of small animal PET scanners. It is by no means the only way of conducting performance testing of such devices nor is it exhaustive. For example, the standard states four tests using phantoms and prescribing certain measurements and calculations, however, it does not specify that the scanner is tested by an actual animal imaging study, which is the ultimate verification of a scanner's usability. Of course one could argue that the purpose of NEMA is to facilitate benchmarking of different technologies. Although articles reporting NEMA results for new devices provide great reference for other manufacturers competing in the same market sector, they are also read by potential customers. Scanner users may need to decide which scanner they are going to choose and since they bear a significant cost, users need to commit to the technology that they will be using for the next 5-10 years. In his article on Mediso USA's blog (Muller, 2014), Muller points out that this group of readers is more interested in the overall performance of the new device, while most review articles give for example only a peak sensitivity value, which most likely pertains a single point source positioned within the scanner's FOV. NU4 standard also requires determination of values for average sensitivities over a mouse (central 7 cm) and rat (central 15 cm) FOV. These values are more useful when assessing how robust a scanner is. Muller warns also against review articles, which often contain out-of-date data. This may be due to the time-scales involved when publishing new papers, but in his view they "distort reality".

Although the NEMA standard does not explicitly require the acquisition of animal images by the system being tested, many articles reporting the performance of new scanners contain animal images. For an audience not familiar with the detailed performance parameters, they are more indicative of what can be achieved in the laboratory environment. Naturally a lot of hardware evaluation

research is conducted in engineering shops, where animal imaging is not feasible. It would be useful nonetheless to be able to compare animal images from different systems, which were acquired using standardised protocols.

The existing NEMA NU4-2008 protocol may require some amendments within the near future. For example, in its sensitivity part it requires moving a point-source along the scanner axis. For scanners without automatic bed movement, this may be difficult to do as typically around a few dozen measurements need to be acquired every 0.5-2 mm step. Elhami and colleagues (Elhami *et al.*, 2011) addressed this problem by comparing the measurements acquired using point-source and using a line source and aluminium sleeves (which is the source used for assessing clinical devices according to NEMA NU2 standard). They found the difference to be within 0.9%, which indicates that a line source may be indeed be a more suitable phantom for sensitivity testing.

NEMA NU4-2008 also requires the measurements of spatial resolution to be reconstructed using FBP. This, however, can be problematic when the manufacturer does not provide this algorithm within the standard software packages. For this reason, often users wanting to perform NEMA NU-4 testing resort to using a non-NEMA compliant reconstruction algorithm, such as iterative reconstruction methods (Herrmann *et al.*, 2013; Spinks *et al.*, 2014). In this case, results obtained using iterative reconstruction cannot be easily compared to those achieved using FBP reconstruction. On the other hand, FBP has some serious drawbacks, which can prevent one from obtaining any results at all at certain positions in the scanner. For example, in the 2-ring Albira PET the gap between the rings corresponds to the axial centre of the FOV. Using single slice re-binning and FBP it is impossible to reconstruct any images of the point source, regardless of their radial offset (Figure 12a). Yet using iterative reconstruction algorithms it is possible to reconstruct images from within the gap region. However, it also needs to be acknowledged that many of the built-in (iterative) algorithms by default apply corrections, which further improves the image. For these reasons caution should be taken when comparing values of spatial resolution reported for different machines.

5.1.2 2-ring Albira PET vs. other small-animal PETs and 1- and 3-ring Albira PET

Goertzen and colleagues published in 2012 a quite comprehensive overview of microPET devices and the NEMA NU4 results. (Goertzen *et al.*, 2012) In 2014 Kuntner and Stout (Kuntner & Stout, 2014) published another fairly exhaustive overview of small-animal PET covering technical parameters like those assessed by NEMA NU4 as well as some practical considerations regarding rodent imaging (e.g. anaesthesia, fasting, vitals monitoring) and PET images quantification. However, in terms of the performance characteristics it cites Goertzen *et al.* and adds Sofie Biosciences Genisys4 citing Herrmann and colleagues, (Herrmann *et al.*, 2013) (although it does not include further NEMA evaluations of this system published by Gu *et al.* late in 2013 (Gu *et al.*, 2013; Gu *et al.*, 2011) and quotes results for the 1-ring Albira PET (Sanchez *et al.*, 2012). Since then Spinks and colleagues published evaluation of the 3-ring Albira PET (Spinks *et al.*, 2014), although only part of those results was obtained following NEMA guidelines (i.e. sensitivity and count-rate performance results were calculated from reconstructed images and not sinograms and spatial resolution acquisitions were reconstructed using MLEM algorithm).

Compared to 1-ring, the absolute sensitivity determined by this evaluation of the 2-ring Albira PET system (5.3%) is over twice that reported by Sanchez *et al.* (2.5%). This is due to the difference in the axial FOV of the 2-ring Albira PET system (94.4 mm as opposed to 40 mm for the 1-ring variant). It could be therefore expected that the 3-ring version would achieve a similar step change in sensitivity of over 7%. However, Spinks *et al.* report only 6.3%. This underestimation could be due to the fact that their analysis was not conducted on raw sinograms, but images reconstructed using MLEM algorithm. Count-rate performances of all three variants cannot be directly compared since Spinks and his team did not analyse their data according to NEMA prescription. Despite this, the results for the 2-ring Albira PET system (scatter fraction of 9.9% and 22% for mouse- and rat-like phantoms, respectively) appear to be in line with those for 1-ring (7.5% and 13%, for mouse- and rat-like phantoms, respectively). Furthermore, system saturation occurred at 205 kBq/ml and 39.9 kBq/ml for the

2-ring Albira PET system for mouse- and rat-like phantoms, respectively, while for 1-ring the same parameters were 370 kBq/ml and 42 kBq/ml, respectively. The lower saturation level observed in this assessment of the 2-ring system may be a result of larger field of view, while the signal-processing electronic remained the same for both systems. As an outcome, the 2 ring system needs to process more events than in the case of a shorter axial FOV, hence a lower saturation level. For both systems the usable range of activities reaches its upper limit at approx. 5-6 MBq. Interestingly, Spinks *et al.* claim the usable range of activities for their system to be up to 10 MBq. The difference may be explained since Spinks and colleagues performed their assessment on a scanner fitted with some more recent upgrades (with respect to the technology used in this investigation of the 2-ring Albira PET system. For example, new electronics will allow dead-time correction over broader range of radioactivities, thereby increasing the upper activity limit. Nonetheless, the 3-ring Albira PET system design allows for a wider acceptance angles and therefore more coincidences are registered, which will improve the scanner's performance in every respect.

One aspect that certainly differs between the 3-ring variant assessed by Spinks *et al.* and the 2-ring one discussed in this thesis is the image quality. The 3-ring Albira PET system utilised attenuation correction, which was unavailable for the 2-ring Albira PET system evaluated here nor was it used by Sanchez *et al.* for assessment of the 1-ring Albira PET. This affected the recovery coefficients (RCs) and spill-over ratios (SORs) reported: RC for 5 mm rod was 95% for the 3-ring PET as opposed to 90% for the 2-ring and 73% for the 1-ring versions; SORs for the 3-ring option were 0.20 for both, air- and water chambers, while for the 2-ring PET they were 0.14 and 0.22, respectively and for the 1-ring version 0.30 and 0.23, respectively. It is worth noting that the RC and SOR values for all three systems are not entirely comparable since the values for the 2-ring PET are reported for an image reconstructed using 20 iterations of MLEM. Even so, the differences among the results for the three versions of Albira PET are not as gross as one could expect looking at the effects of attenuation correction implemented in Siemens Inveon, which reduces SORs of both, water and air chambers to almost 0 and increases the RC for 1 mm rod to 21% (as opposed to 5%, 3% and 2% for the 2-ring, 3-ring and 1-ring Albira PET, respectively). (Visser

et al., 2011) This may prove to be an opportunity for the future improvement of the reconstruction algorithms used by the Albira system.

5.1.3 2-ring Albira PET vs. other tri-modal PET/SPECT/CT scanners

The Albira is not the only tri-modal PET/SPECT/CT platform ever developed. There are three other available commercially: TriFoil Imaging Triumph (Aide *et al.*, 2012; Prasad *et al.*, 2011a; Prasad *et al.*, 2010; Prasad *et al.*, 2011b), Siemens Inveon (Bao *et al.*, 2009; Kemp *et al.*, 2009; Magota *et al.*, 2011; Visser *et al.*, 2009; Visser *et al.*, 2011) and MILabs VECTor (Goorden *et al.*, 2013). As of 2015, the Inveon is no longer being manufactured. However, being in use at many research institutions, it remains probably the most popular to date. The VECTor platform is distinct among others since its imaging approach is based on the principles of SPECT imaging for both, single-photon and positron-emitting radionuclides. VECTor scanner contains of a common gantry made of three large stationary detectors common for the PET and SPECT imaging. It is within this gantry that a cylindrical, clustered-pinhole (48 clusters of 4 pinholes) tungsten collimator is inserted. According to Goorden and colleagues (Goorden *et al.*, 2013) such design allows for simultaneous imaging of PET and SPECT radiopharmaceuticals. This could not be achieved in either Albira, Triumph or Siemens scanners, which all separate each of their modalities and allow for sequential imaging only. Yet, even though the simultaneous PET/SPECT imaging has its merits (visualisation of more than one molecular targets at the same time), it is worth noting that the sub-millimetre resolution for PET and SPECT, that authors claim, was not achieved following any standard protocol of performance testing, but a 1-hour scan of mini-Jaszczak phantom. This is a rather long imaging time compared to the 20 mins prescribed by NEMA standard in the image quality testing section. However, regardless of reported performance results, VECTor PET cannot be compared with PET sub-systems of aforementioned other commercial tri-modal platforms, because by using the collimator feature it is no longer a coincidence PET and cannot be fully quantitatively assessed.

The shared PET/SPECT detector gantry was recently reported for new animal PET/SPECT/CT system, a compact platform called Inliview-3000 (Wei *et al.*, 2015), which is not yet commercially available. Inliview-3000 features cone-beam helical CT scanner, which has been by far used mostly in clinical machines. Additionally, the PET/SPECT detector ring is similar to the one used in Albira PET in the sense that it too uses octagonal detector arrangement in a ring, although unlike Albira, Inliview-3000 uses arrays of LYSO crystals (9720 crystals in total vs. 8 in Albira). The SPECT capability is achieved by the insertion of the rotating cylindrical tungsten multi-pinhole (50 elliptical holes) collimator between the detector ring and the imaging bed. In that sense Inliview-3000 SPECT is somewhat similar to VECTor PET/SPECT. In terms of performance as prescribed by NEMA, results for the Inliview-3000 PET are in line with Albira and Triumph platforms - the only two remaining on the market. The system is described by Wei *et al.* as low-cost, which, if it remains the case, may change the landscape of small-animal PET/SPECT/CT scanners.

5.1.4 Albira PET vs. MAMMI PET

Since its publication virtually every new small-animal commercial scanner or even an upgrade over a previous version has been evaluated using NEMA NU4-2008 guidelines. The standard has also found an application for special types of clinical scanners such as Positron Emission Mammographs (called also Mammi-PET) for which NU2 was not appropriate given their unconventional geometry. (Luo *et al.*, 2010) One such device of interest is the Oncovision MAMMI PET, which utilises almost the same hardware as Albira (in fact, Albira PET was its predecessor) with the exception that instead of 8 detectors, it contains 12 in a single ring of detector. The MAMMI PET system requires the patient to lie on her abdomen so that the breast, hanging through the hole in the bed is positioned in the aperture of the scanner gantry below. Evaluation of such geometry required Soriano *et al.* (Soriano *et al.*, 2013) to adapt NEMA standards NU2-2007 and NU4-2008. Furthermore, the device assessed in their work was an improved, the 2-ring version of MAMMI PET, which used also thicker LYSO crystals: 12 mm instead of 10 mm used in the Albira system or in the 1-ring MAMMI and, unlike 1-ring MAMMI, utilised DOI correction. This work is of even more interest since the 2-

ring MAMMI, like 2-ring Albira suffers from the gap between the rings, which encompasses the centre of the axial FOV. The reported sensitivity, even though twice than what was reported for the 1-ring MAMMI (Moliner *et al.*, 2012), was 3.1% as opposed to 5.3% for the 2-ring Albira. The difference may be a result of the geometry of the MAMMI scanner, which has a larger aperture than Albira (to allow space for a human rather than a rat or mouse and therefore has smaller acceptance angles for registered coincidences. It is also noteworthy that Soriano and colleagues measured better spatial resolution at the quarter of the axial FOV rather than in the centre: 1.6, 1.8, 1.9 mm at the centre vs. 1.5, 1.6 and 1.7 mm at the quarter of the axial FOV in radial, tangential and axial directions, respectively. This is the same observation as was made in the 2-ring Albira PET, where in the quarter of the axial FOV spatial resolution is 1.5, 1.7, 1.5 mm as opposed to 1.7, 1.7, 2.5 mm in the centre in radial, tangential and axial directions, respectively. Furthermore, it can be expected that the spatial resolution results obtained could be further improved if NEMA would allow for a different choice of the axial position for spatial resolution measurement. In particular, if the measurements were made in the centre of the rings. As such, the current requirements of NEMA NU4 are sub-optimal for the scanners like the Albira PET or MAMMI PET.

5.1.5 Albira PET Improvements

Recently an application note was published (Gonzalez *et al.*, 2015) detailing some new improvements to Albira PET design developed by Oncovision. Unlike previous upgrades that allowed faster electronics or better reconstruction algorithms, the new improvements will most likely fundamentally change the Albira PET system and its performance. The first improvement announced by Gonzalez *et al.* is a reduction of the gap between the scintillators, which as a consequence reduces the gap between the detectors within the ring to 0.5 mm. This should improve the image quality and spatial resolution by reducing the streak artifacts (Figure 12c) seen in an image taken of a point source placed within the gantry of the current 2-ring Albira PET system.

Another improvement will be the shape of the scintillator crystals, which will still have 50×50 mm base, but the top of the crystal will increase from the current 40×40 mm to 48×48 mm. There will also be a major change to the photomultipliers used. Currently, the Albira PET system implements multi-anode position-sensitive photo-multiplier tubes (MA-PS-PMT). The new technology utilises silicon photomultiplier (SiPMs) photosensors along the monolithic scintillators (LYSO crystals). The latter are a feature of all the former generations of Albira PET, but the new detectors are more compact and compatible with simultaneous PET-MR or in-line CT. The application note stipulates the new system (part of the new Albira platform called Albira Si) to have more uniform spatial resolution within the range of 1 to 1.2 mm. Sensitivity should also increase from about 9% to almost 12%. (Bruker BioSpin, 2014)

5.2 Albira CT Performance and Quality Assurance

Using a micro-CT mouse phantom, the basic stability of the CT system can be examined. The experiment conducted over three days revealed that during the first day there was a large difference between HU measured for the densest rods in the images acquired using a different number of projections. However, the variability between the measurements taken on the second and third day was minimal. This may be since on the first day the images were acquired within the first 30 mins after the system was powered on, while the system remained on for days 2 and 3. This would indicate significant relationship between the temperature of the lamp and quality of the acquired image. It would be therefore recommended that the Albira is on for at least an hour before any CT images are being acquired.

The high current-high voltage setting underestimated the HU for lungs region (Figure 18). Whereas, the high current-low voltage and the low current-high voltage settings measured a value close to -600 HU for the lung region which agrees with the expected HU values for lungs (see

Table 9). The best setting for small animal imaging would allow visualisation of the greatest difference between lungs and bone regions, and overall the highest

level of detail. The data acquired from the CT phantom clearly showed that low voltage-high current (35 kV - 0.4 mA) setting shows the biggest change in HU between the lung and bone densities.

Table 9 Example Hounsfield Units (HU) for different types of tissue, air and water (Brant & Helms, 2007)

Substance/tissue	HU
Air	-1000
Lung	-800 to -400
Adipose tissue	-100 to -60
Water	0
Muscle	10 to 40
Soft tissue	40 to 80
Soft tissue (contrast agent)	100 to 300
Bone	400 to 3000

In terms of the amount of tissue detail visible, the number of acquired projections was found to be the parameter of the most significance. However, the absorbed dose is proportional to the duration of the scan and hence also the number of projections (Figure 4). And therefore, since some imaging studies may have a longitudinal design, which entails the repetitive exposure of the animal to the ionising radiation, the duration of the single scan becomes important. As Figure 21 shows, there is not much difference between “high resolution” and “best” settings, and therefore the shorter duration of the best quality setting may be considered more appropriate, especially when performing repeat imaging of the same animal. Furthermore, when the CT image is required to provide only a general frame of reference and smaller skeletal features are not

of importance, a lower quality may also be the more appropriate setting of choice.

Some examples of the impact that reconstruction parameters have upon the image quality using “standard” and “high resolution” images of the CT mouse-like phantom are shown in Figure 22 and Figure 23. The quality of the resulting images between “medium” and “high” FBP was very similar. The smaller the voxel size used during reconstruction, the larger the constructed image matrix, the larger the overall size of the image and the longer the reconstruction time. Unless CT is being used as stand-alone diagnostic tool, “medium” setting of FBP is probably the one that will satisfy most applications. Although the “low” reconstruction setting led to significant deterioration of the image quality, it may still be useful for a quick preview of the acquired data, but its usefulness beyond this is rather limited.

The low current-low voltage setting showed strong beam hardening effects on all settings investigated and proves this acquisition to be unsuitable for animal imaging. On visual examination of the different reconstruction settings (Figure 25 and Figure 26) the high current-low voltage showed the best image quality, albeit the contrast between the body of the phantom and 50 mg/cc rod is very poor. Analysis of the apparent quality of the images reconstructed using “high” and “medium” FBP settings led to the conclusion that the quality of the images reconstructed using $0.25 \times 0.25 \times 0.25 \text{ mm}^3$ voxels is almost as good as of those reconstructed using $0.125 \times 0.125 \times 0.125 \text{ mm}^3$ voxels. A cadaver was imaged using the high current-low voltage setting (Figure 25), which was identified as the preferred acquisition setting for small animal imaging studies. The image allowed visualisation of the soft tissue within mouse however the soft tissue contrast is not sufficient to distinguish all the different organs. Different contrast agents may be considered to alleviate this problem. A good overview of CT contrast small animal imaging was given by Wathen and colleagues. (Wathen *et al.*, 2013). Injectable contrasts (e.g. Iomeprol 400, Omnipaque, gold nanoparticles, Aurovist, ExiTTron nano 12000, Fenestra VC, Visipaque 320) can be used to show vasculature, liver or kidneys enhancement. In addition, the gastrointestinal tract can be visualised using ingestible contrasts (e.g. barium

sulphate). However, the use of contrast agents in small animal CT imaging has many limitations, namely:

- the cost of many more sophisticated contrast agents (e.g. gold nanoparticles) can be high and may therefore be not feasible,
- the use of contrast agents requires careful titration as they may have toxic effects upon an animal,
- the use of contrast agents allows usually for enhancing an image only of a single organ,
- dosing an animal with too high amounts of a contrast agent may lead to opaqueness of the affected organ not only for X-rays, but may also lead to scattering of the gamma-rays produced by single-photon emitting radionuclides or of the anti-parallel pairs of photons produced in the positron annihilation events,
- in the experiments utilising nuclear imaging the use of contrast agent complicates imaging protocols leading to greater variability.

5.3 PET/CT quality control

The main objective of NEMA U4-2008 standard is the performance testing of small animal PET scanners. Apart from the benchmarking of the emerging technologies it is frequently followed in an acceptance testing of new scanners or in periodical (e.g. annual) quality control (QC) measurements. However, due to its complexity it is rather impractical for a weekly or day-to-day QC. Although to date no uniform QC standards were set for small animal PET scanners, clinical tomographs have been following such guidelines for years. (Saha, 2010)

The most basic test performed on PET is a uniformity test. It requires a transmission scan, which is acquired using long life positron emitter (e.g. ^{68}Ge or ^{137}Cs) and generation of a sinogram from the gathered data. If there is a problem with any detector pair, it will appear on the sinogram as a streak. Furthermore, the uniformity test allows also for checking if the normalization works as

intended - any deviation will produce non-uniform sinogram. Unfortunately, generation of sinograms in the Albira requires writing custom computer code to process scanner's list mode files, so any test requiring this form of reconstruction may prove to be impossible to follow through. Acquisition file could be reconstructed using the built-in iterative algorithms (MLEM or OSEM) in the provided software, but these reconstruction methods may obscure potential hardware problems.

Another useful test, which may also be used to check the uniformity uses a phantom filled with positron-emitter (e.g. solution of ^{18}F), which is then scanned. After the reconstruction (using the attenuation correction, where available) the image should be inspected for any non-uniformities. NEMA NU4 covers such check in image quality part of the standard; however, the area of the phantom used is rather small. It would be more accurate to use a cylindrical phantom for this purpose (supplied by the Albira vendor) and image it in few different positions along the scanner axis.

Above-described phantom can additionally be used to check for dead-time correction accuracy. Specifically, if filled with the solution of short-lived positron emitter like ^{11}C or ^{18}F it should be scanned repeatedly over few half-lives of the isotope used. Resulting images, when reconstructed, on any selected VOI within the phantom should show activity concentration that follows the decay curve over time. Alternatively, measured activity should remain constant if decay correction was applied. If the measured activity in time differs from the theoretical value that can be easily calculated it may indicate a drift in the detector electronics or corruption of the dead time correction file.

It may also be advisable to complete a dose calibration test, which requires a scan of a phantom (e.g. Jaszczak phantom) containing known activity concentration (or a range of different concentrations). Next these known values should be compared to those measured on the reconstructed image. The phantom used should have sufficient size to avoid partial volume effect (i.e. larger than approx. twice the spatial resolution of the scanner).

QC of the CT component requires similar approach. Namely, acquisition of an image phantom filled with water and/or air allows for verification of the HU values. Also, any dead-lines in the detector (non-responsive parts of the detector) will appear as streaks on the reconstructed image. In the clinical context, periodical dose measurement during the standard scan is performed to ensure patients safety; however, this is not a common practice in small animal CT QC.

This work was focused upon performance evaluation of the Albira 2-ring PET based on the NEMA NU4-2008 standard and not on periodical QC measurements of any of its sub-systems. CT phantom was imaged to establish the most useful acquisition parameters in the mouse imaging studies and to test whether the CT component is thermally stable. It was established from the measurements that the scanner should be best powered on continuously to avoid quality fluctuations. This was not, however, a part of any QC protocol.

5.4 Multi-modal Animal Studies

Currently there are several commercial small animal single or dual-modality (combined with CT or MRI) dedicated PET or SPECT scanners. The power of the tri-modal platform, however, is in its flexibility and potential to utilise both nuclear imaging methods within one experiment. These dual radionuclide studies (PET and SPECT) studies take advantage of the fact that the photons emitted from the annihilation events occurring from PET radionuclides have greater energy (511 keV) than the photons emitted from SPECT radionuclides (e.g. 140 keV for ^{99m}Tc). The order in which the SPECT and PET scans are completed is important for these dual radiotracer studies. To successfully complete a dual-radiotracer imaging experiment, the SPECT radiopharmaceutical administration and scan must be conducted before administration of the PET radiopharmaceutical. This is to prevent the 511 keV photons from the PET radionuclide masking the photons being emitted from the SPECT radionuclide. In Figure 27 maximum intensity projections from a dual radionuclide imaging study are presented.

For all three modalities the image was rotated around the z-axis by 30° in order to show the uptake of the radiotracer in sternum and ribs. On the SPECT image a small gap within the middle of the image is visible. It is thought that this may have been caused by the slightly inaccurate calibration of the instrument (wrong axial offset of the second bed scan) or error during the stitching of the images of individual beds into the final SPECT image. No corrections were applied in the SPECT image, nor was here any post-processing except for masking the bladder, which showed excretion of the radiopharmaceutical in the urine. All the major joints are visible, but the vertebrae cannot be distinguished. Scatter and randoms corrections were applied as part of the reconstruction of the PET image, so limited options exist in terms of improving image quality and the represented level of detail. The centre of the image, which corresponds to the gap between the detector rings, suffers from axial under-sampling, which in turn leads to blurry image of mouse's spine. In comparison, the vertebrae in the tail are more distinguishable. This suggests that when imaging of structures approaching spatial resolution limit of the scanner (<1.7 mm) or smaller is required, the imaged subject should be positioned in the manner that structure of interest lays as close to the trans-axial centre and as close to the centre of the ring as possible. In any case the CT image can be used to visualise all the bones and the outline of the mouse's body and bladder.

The dynamic PET scan seen on Figure 28 and its complementary TACs (Figure 29) demonstrated that after 30 minutes the accumulation of ^{18}F -NaF in most joints, vertebrae and skull is close to maximum. This data suggests that a minimum uptake time of 30 minutes is required when imaging using ^{18}F -NaF. The uptake of ^{18}F -NaF remained almost unchanged up to 90 minutes. Therefore, imaging mouse between 30 and 90 mins should yield optimal results.

In future studies, if there was a region of interest the time-activity curves obtained in this study could be used to determine the optimal time to image that region. This highlights how when setting up new imaging protocols using a new radiopharmaceutical, dynamic scanning can provide information on the radiopharmaceutical pharmacokinetics and the optimal time for imaging. To further examine the kinetics of a radiotracer blood sampling would be needed to

establish a blood input function, which can serve as an input in kinetic modelling. However, for well-known radiopharmaceuticals (^{18}F -FDG, ^{18}F -NaF etc.) static imaging protocols can allow for serial and high through-output imaging.

Part II: Using ^{18}F -FLT and Positron Emission
Tomography in Monitoring Treatment
Response in Murine Pancreatic Cancer
Models

6 Introduction

6.1 Anatomy, Morphology and Role of the Pancreas

The pancreas is an exocrine and endocrine gland, which forms part of the digestive system. On one hand, it secretes hormones like insulin, somatostatin, pancreatic polypeptide and glucagon, which control metabolism and blood sugar levels. On the other, enzymes like trypsinogen, lipase, and amylase, among others, produced by the pancreas are indispensable for normal digestion, breaking down proteins, lipids and carbohydrates in stomach, duodenum and small intestine.

The gross anatomy of the pancreas depends on the species in question. For example, the human pancreas is dense and compact. It can be divided into head, body and tail, while in mice parts of the pancreas are diffused and separated by a mesenteric fat. (Dintzis & Liggitt, 2012) In both cases the organ is encapsulated by the thin layer of connective tissue.

Histological analysis of the pancreas allows for the distinction of important functional regions, identifiable regardless of species. (Dintzis & Liggitt, 2012; Dolenšek *et al.*, 2015) These regions are:

- Lobules,
- Islets of Langerhans,
- Blood vessels,
- Lymph vessels,
- Nerves ganglia,
- Ducts.

Each of the regions is associated with different type of cells, which form it. Those of particular interest in this work are: acinar cells (which form lobules), alpha, beta, delta and gamma cells (aggregated in the pancreatic islets) and ductal cells (pancreatic ducts). (Dintzis & Liggitt, 2012)

6.2 Differences between Human and Murine Pancreas

The human pancreas is compact and its parts can be clearly distinguished. The pancreas of the mouse is, on the other hand, diffused and its parts cannot be clearly distinguished. At the histological level, the size of the lobules is relative to the size of the species, but this relationship does not hold for the islets. The ducts become larger for larger species. Mice have a common bile duct and pancreatic duct (or ducts), which drain to duodenum. In humans, common bile and pancreatic ducts first join at ampulla of Vater (major ampulla) and form a conduit, which then drains bile and pancreatic secretions into the duodenum. (Campbell & Verbeke, 2013) The islets of Langerhans vary in size and location within the murine pancreas and are about twice the size compared to human ones. Additionally, in mice the acinar cells have multiple nuclei, which is not the case in humans.

6.3 Overview and Statistics for Pancreatic Cancer in UK

6.3.1 Types of Pancreatic Cancer and Epidemiology

Pancreatic cancer is one of the most lethal types of cancer. The chances of survival depend very much on the stage of the disease and its subtype. All pancreatic cancers can be divided into two general categories: endocrine and exocrine ones, where the latter account for over 95% of all cases. Pancreatic cancer can be broken down into the following sub-types (Pancreatic Cancer UK, 2014):

Exocrine

- Pancreatic ductal adenocarcinoma (PDAC),
- Solid pseudopapillary neoplasm,
- Serous cystadenocarcinoma.
- Acinar cell carcinoma,
- Intraductal papillary mucinous neoplasm with invasive carcinoma (IPMN),

Endocrine

- Neuroendocrine tumour (NET),
- Somatostatinoma,
- Mucinous cystic neoplasm with invasive carcinoma (MCN),
- Insulinoma,
- Glucagonoma,
- Pancreatoblastoma,
- Verner-Morrison syndrome (VIPoma).

More than 60% of pancreatic tumours originate in the head of the pancreas and around 30% in its body and tail. 5% of pancreatic neoplasms grow in the whole organ. (Pancreatic Cancer UK, 2014) The most aggressive subtype, PDAC is diagnosed in more than 85% of all cases and is associated with the poorest survival: less than 5% in within the 5-year-period. Frustratingly, despite research effort, this survival rate has not changed in the last 40 years, which makes PDAC one of the deadliest types of cancer diagnosable.

6.3.2 Risk Factors

The exact aetiology of pancreatic cancer remains unknown; however, to date few main risk factors were identified:

- tobacco smoking,
- obesity (BMI over 35),
- lack of physical activity,
- ethnicity,
- diabetes mellitus,
- genetic predisposition,
- age and gender,
- chronic pancreatitis.

Tobacco (and smokeless tobacco) smoking. Various studies suggest that tobacco smoking, including smokeless tobacco (Boffetta *et al.*, 2005), increases the risk of pancreatic cancer between 20 to 100%. (Ekblom & Trichopoulos, 2008)

Smoking cessation reduces the risk over time, but it takes 20 years before it is comparable to the one of a person, who never smoked. It is therefore the main avoidable risk factor.

Obesity and lack of physical activity. Obesity also has been shown to increase such risk (de Gonzalez *et al.*, 2003) and so does the lack of physical activity. (de Gonzalez *et al.*, 2006)

Diabetes. There is significant positive correlation between pancreatic carcinoma and diabetes mellitus type 2 (Adami *et al.*, 1991; Noto *et al.*, 2011; Zhang *et al.*, 2012).

Familial history of pancreatic cancer. Having at least two diagnosed blood-relatives increases the risk from 7 to 13 times, which points to genetic predispositions that may be inherited. (Ekbom & Trichopoulos, 2008; Fernandez *et al.*, 1994; Ghadirian *et al.*, 1991; Klein *et al.*, 2004)

Genetic mutations de novo. In over 90% of cases, however, the culprit mutations in oncogenes and tumour-suppressor genes are the result of *de novo* mutations acquired during an individual's lifetime. (Ekbom & Trichopoulos, 2008; Petersen *et al.*, 2006)

Age, sex and ethnicity. Another factor showing strong positive correlation is age with most diagnosed cases being in persons over 65. Men seem to be slightly more susceptible than women and also African American origin predisposes to the disease more than other racial backgrounds. (Ekbom & Trichopoulos, 2008)

Alcohol consumption. Excessive alcohol consumption (defined as 6 or more drinks per day) is also associated with increasing the risk by half. (Ekbom & Trichopoulos, 2008; Michaud *et al.*, 2001)

Pancreatitis. Chronic pancreatitis may nearly triple the risk of developing pancreatic cancer, but hereditary pancreatitis increases the risk of its onset by a factor of 70 by the age of 70 making it one of the most prominent risk factors in pancreatic adenocarcinoma. (AndrenSandberg *et al.*, 1997; Ekbom & Trichopoulos, 2008)

6.3.3 Clinical Signs and Symptoms

One of the reasons of high mortality in PDAC is its late diagnosis. Many patients do not experience symptoms in the early stages of the disease. Additionally, all initial symptoms can indicate conditions of gastrointestinal tract (e.g. pancreatitis, diabetes mellitus, gallbladder stones, jaundice), which are much more common. The clinical presentation may vary, depending on the origin of tumour (head, body or tail of the pancreas) and the type of the cancer, although most of the symptoms described below are common features of all pancreatic cancers, especially the exocrine cancers like PDAC.

The most common symptom is an abdominal pain and/or upper back pain. This may indicate:

- the cancer spread to the nerves surrounding pancreas,
- an inflammation of the pancreas or surrounding organs,
- an obstruction of the bile duct, stomach or duodenum by the growing tumour.

Pancreatic tumours are solid, characterised by desmoplasia, which is suggested to be the source of their chemoresistance. (Whatcott *et al.*, 2012) They are unlikely to be palpable, although gallbladder may and in the advanced stages of metastatic disease umbilical nodule or nodules (Sister Mary Joseph nodule) may be felt. (Bai *et al.*, 2012)

Any of the above symptoms can in turn lead to nausea and vomiting, fever and shivering and, when the tumour blocks the bile duct, an obstructive jaundice. In the latter case, an excess of bilirubin in the blood causes the change of skin colour and whites of the eyes into yellow, itchy skin, dark urine and pale stools. An ascites (a build-up of fluids in the peritoneal cavity) can also occur in the advanced stages of pancreatic cancer.

Due to the progressive loss of the function of the pancreas, there is underproduction of the endocrine digestion enzymes. This can lead to diarrhoea, steatorrhea (large, oily, pale, floating and foul-smelling stools indicating that the body is not digesting fats), and dyspepsia. The inability by the body to

properly digest and absorb nutrients eventually leads to weight loss. In the late stages of cancer development, cachexia usually occurs, which is characterised by a weight loss, loss of appetite, muscle atrophy and fatigue.

A major symptom that can indicate a tumour growing in the pancreas is also diabetes. Sudden diabetes can cause: polydipsia (increased thirst), polyuria (increased urination), polyphagia (increased hunger), headaches, weight loss, fatigue, blurry vision, itchy skin or slowly healing wounds. However, there is also growing evidence that diabetes may be, in fact, a contributory factor to the development of cancer and not just its consequence. (de Gonzalez *et al.*, 2003)

6.3.4 Diagnosis and clinical classification

All the aforementioned clinical signs are non-specific. Therefore, initially other possible diagnoses need to be excluded. Blood testing is conducted. Raised levels of conjugated bilirubin, alkaline phosphatase and γ -glutamyl transpeptidase in liver function tests usually indicate biliary duct blockage. (Carr-Locke & Davies, 1980) Testing for a cancer marker CA19-9 (carbohydrate antigen 19.9) is sometimes conducted. It has been shown that 85% of patients diagnosed with PDAC show elevated levels of CA19-9. Furthermore, there is a correlation between the level of this antigen and the stage of the disease. (Parikh *et al.*, 2014)

Medical imaging is invaluable in determining the location of the tumour. This is done using one or more of the following imaging modalities:

- Ultrasound (US),
- Endoscopic Ultrasound (EUS),
- Computed Tomography (CT),
- Magnetic Resonance Imaging (MRI),
- Magnetic Resonance Cholangiopancreatography (MRCP),
- Positron Emission Tomography (PET).

These techniques allow for a visualisation of the tumour and its location. However, in order to ascertain the exact type of cancer, an US-guided biopsy (usually by fine needle aspiration) is conducted. Pancreatic cancers can be

differentiated based on the morphological differences visible during the histopathological examination. To aid pathologists, medical residents and fellows the Johns Hopkins University School of Medicine compiled a comprehensive atlas of human pancreatic pathology. Providing gross anatomy and histological photographs it shows the features of 115 diagnostic entities. (Hruban *et al.*, 2015)

Based on the results of the aforementioned tests, the disease is classified using a two-tier system. First, a tumour is described using a TNM scoring system. “T” stands for “tumour” and describes the size of a tumour, with five possible values: from the smallest (Tis = carcinoma *in situ*) to the largest (T4). Lymph nodes involvement is considered (the “N” stage) and one of two discrete values: N0 or N1 is assigned (no lymph nodes involvement or cancer spread to lymph nodes, respectively). Metastatic spread (the “M” stage) is also either positive (M1) or negative (M0), which describes if the cancer spread beyond the pancreas or is still limited only to its primary organ. Based on the TNM staging, the cancer is classified as falling into one of four stages (from the least, stage 1 to the most severe, stage 4) of the disease advancement.

6.3.5 Statistics for UK

Cancer Research UK, a main cancer research and awareness charity in UK, on its website (Cancer Research UK, 2015a) summarised data provided by the statistics collecting authorities for all parts of Great Britain:

- Office for National Statistics (Office for National Statistics, 2015),
- Information Services Division (ISD) Scotland (Information Services Division Scotland, 2015),
- Welsh Cancer Intelligence and Surveillance Unit (Welsh Cancer Intelligence and Surveillance Unit, 2015), and
- Northern Ireland Cancer Registry (Northern Ireland Cancer Registry, 2015).

This summary spans from early 70s until 2012 and regards pancreatic cancer and its incidence, mortality and survival.

According to this publication, pancreatic cancer accounts for 3% of all new cancer cases, equally affecting men and women, and as of 2012 is the tenth most common cancer in UK with 8875 new cases (4453 men and 4422 women) diagnosed that year. This is slightly above the worldwide average of 2% (338,000 new cases diagnosed in 2012), and in line with European statistics, which place pancreatic cancer as the eighth most common types of cancer (104,000 new cases in 2012, which is equal to 3%). The crude incidence rate per 100,000 persons in the UK is 14 for males and females.

Pancreatic cancer seems to strongly correlate with age. Only about 4% of new cases are diagnosed in patients below the age of 50 and almost half (47%) were diagnosed in persons aged 75 or over. Although the age-standardised ratio between men and women affected by this disease is 1:1, detailed analysis of the annual incidence rate distribution across the age groups for both genders shows that for ages 45 to 49 this ratio is 15:10. As of 2010 the lifetime risk of developing pancreatic cancer for men and women in UK is 1 in 73 and 1 in 74, respectively.

Although, pancreatic cancer is rather infrequent compared to other cancer types; its mortality and survival data place it among the deadliest. Age-standardised data for England and Wales for years 2010-2012 shows that almost 21% of adults survive one year, but this percentage falls to only 3% when survival is measured over 5-years and to 1% in 10-year period. The survival rate shows strong correlation with age. Based on the data for England during 2007 to 2011, the 5-year survival rate for men is 14% among the population aged 15 to 49 and falls to only 2% for 80 to 99 year-olds. For women and for the same age groups the 5-year survival rates are 24% and 2%. There is then 10% difference between the 5-year survival rate of men and women in the under 50-age group. In Europe, the average 5-year survival rate is 5%, however, it ranges across different countries from 2% to 9%. Cancer Research UK suggests that this variation may be partially due to differences in data collection among the individual countries.

The median survival for patients who have undergone surgical resection of the primary tumour is 11 to 20 months and their 5-year survival rate ranges from 7% to 25%. PDAC, however, is highly infiltrative, which means that it is frequently not easy to distinguish the margin of the disease (so-called R0- zero resection

margin beyond which the tissue is cancer-free). Therefore, although surgery is the most effective treatment for pancreatic cancer, most of the patients at the time of diagnosis have too advanced disease (either advanced locally or one that has frequently spread to other organs) or are too unwell to undergo the procedure. Therefore, patients with stage III (unresectable locally advanced disease) have 6- to 11-month median survival and stage IV (metastatic disease) only 2 to 6 months.

Over the last three decades (1979-1981 to 2010-2012) in UK, the incidence of pancreatic cancer among men aged 25 to 49 decreased by 30%, but for men aged 70 to 79 over the first two decades of that period decreased by 19%, and then rose by 8%. Among females over the age of 60, however, the incidence rate is on the rise and increased by 14% from the late 1970s. For women over 80 this rate has been increasing since late 1990s and has risen by 11%. For other age groups of men and women the rate has remained stable over the last thirty years.

6.4 Genetic Background of Pancreatic Ductal Adenocarcinoma

6.4.1 Mutated Genes and Pathways

As with many other types of cancer, pancreatic cancer is driven by a variety of genetic alterations, which affect cell proliferation, apoptosis, regulation of the cell cycle and other signalling pathways. The disease initiation and progression seem to rely mainly on activation of mutated oncogenes and inactivation of tumour suppressing genes, which can be attributed to somatic point mutations and allelic losses. (Simeone & Maitra, 2013) The former group mainly target KRAS2, a proto-oncogene that has been identified in over 90% cases of pancreatic neoplasms. The main genes in the latter group are: CDKN2/INK4, inactivation of which was found in around 90% of cases; Tp53, mutations in which are encountered in approximately 75% of analysed cases and which are associated with metastatic disease (Hingorani *et al.*, 2005; Morton *et al.*, 2010); and SMAD4/DPC4, which is deleted in 55% of the resected tumours. Other genes involved in this type of cancer are BRCA2, which is encounter in 19% of familial cases (Hingorani *et al.*, 2005) and less than 10% of sporadic ones. MSH2 and

MLH1, genes responsible for the DNA repair, are mutated in less than 10% of cases. It seems, however, that the less frequently encountered mutated genes are being identified in rather rare types of pancreatic cancer and do not coexist with KRAS or Tp53 mutations, which are mainly seen in PDAC.

Based on the analysis of 456 resected pancreatic tumours Bailey and colleagues in their recent work identified 32 genes which could be assigned to 10 distinct signalling and cell differentiation pathways, i.e.:

- KRAS,
- TGFB,
- WNT,
- NOTCH,
- ROBO/SLT,
- G1/S transition,
- SWI-SNF,
- Chromatin modification,
- DNA repair,
- RNA processing.

Furthermore, analysis of gene expression allowed them to propose a new classification of pancreatic cancer consisting of four subtypes: squamous, pancreatic progenitor, immunogenic and ADEX (aberrantly differentiated endocrine exocrine), which in their view may aid in the development of new therapeutic targets and agents. (Bailey *et al.*, 2016)

6.4.2 Mouse Models of Pancreatic Ductal Adenocarcinoma

6.4.2.1 *Rationale for Using Murine Models*

Many therapeutic targets and drugs in cancer research are discovered at the *in vitro* stage using biochemical and cell-based assays. The most likely next step in drug discovery are *in vivo* trials involving the use of animal models. Without the *in vivo* experiments, it is impossible to predict the behaviour of the therapeutic agent in a living organism from the *in vitro* results alone. Yet, many drugs fail at

the *in vivo* stage. In such cases at best they show no effect on the subject. At worst, they have fatal effect or cause such severe side effects that no therapeutic benefits can outweigh them. If the results at the *in vivo* stage, however, are encouraging, pilot clinical trials can be scheduled.

An animal genetically closest to a human is a monkey. However, the use of monkeys in research is expensive and poses many ethical concerns. However, other mammals also can prove viable alternative. The Mouse Sequencing Consortium reports that out of 4000 genes that have been studied in humans and in mice only 10 appear in either one or the other species.

(Mouse Sequencing Consortium, 2010) The potential of using mouse models of human disease is not only plausible, but it is a reality. There are various types of mouse models of cancer. One of them is xenograft, where human cells are implanted into immune-compromised mice, subcutaneously or into an organ they were taken from. Such models can be useful in the initial screening of drugs cancer cells may be susceptible to (so-called personalized medicine), but are less useful for studying disease initiation and progression.

Genetically modified mouse models (GEMMs) focus on genes, which are commonly found to be mutated in certain sub-types of cancer. Some of those models very well recapitulate features of human disease. Their other benefit is the lifespan of a mouse, which is much shorter than the one of human. Mouse gestation lasts only 3 weeks; it is therefore possible to test research hypothesis over few generations of mice reasonably quickly. Below two mouse models of PDAC are described. The clinical symptoms mice exhibit in both models are very similar, although on the molecular level there are differences in the pathways activated.

6.4.2.2 *KPC*

Hingorani and colleagues proposed a mouse model of PDAC based on the endogenous expression of mutated KRAS and Tp53 genes. (Hingorani *et al.*, 2005) This transgenic model uses the Cre-Lox system to conditionally express those genes in Pdx-1 expressing pancreatic progenitor cells. Hence, the model is known as KPC (KRAS; Tp53; Cre-Pdx-1).

KRAS is a proto onco-gene and its point mutations have been identified in over 90% of all diagnosed cases of human PDAC. Heterozygous (homozygous expression is known to be lethal at the embryonic stage), endogenous expression of mutated KRAS (henceforth noted as KRAS^{G12D}) is responsible for the initiation of pancreatic intraepithelial neoplasia (PanINs), which are understood to be the progenitor lesions leading to pancreatic adenocarcinoma and are common in elderly human population. (Hruban *et al.*, 2008) PanINs are classified by grades corresponding to the level of histological changes observed. From the least severe these are PanIN-1A, PanIN-1B, PanIN-2 and PanIN-3, beyond which carcinoma *in situ* is diagnosed. (Hruban *et al.*, 2001; Maitra & Hruban, 2008) Although KRAS^{G12D} by itself can develop into carcinoma and then into invasive metastatic disease, its progression is slower than when it is concomitant with the mutations (or deletions) of the tumour suppressor genes like Tp53 (e.g. Tp53^{R172H}, which is an ortholog of the mutation identified in human disease). Inactivation of Tp53 is observed at PanIN-3 grade of pancreatic lesions and beyond - in adenocarcinoma (Hruban *et al.*, 2001), and is identified in up to 75% of PDAC cases.

6.4.2.3 *KC Pten*

Another mouse model resembling KPC uses the Pdx-1-Cre system to conditionally express heterozygous mutation of KRAS (KRAS^{G12D}) and biallelic deletion of the Pten gene (Pten^{flox/flox}) in pancreatic progenitor cells (Pdx-1). Like in the case of KPC model, mutant KRAS is understood to be the initiator of the neoplasms in pancreatic tissue. Pten, on the other hand is another well-known tumour suppressor gene. In terms of the disease progression, this model resembles KPC; however, due to different genetic background the signalling pathways driving the disease, mainly PI3K/AKT and MAPK pathways. (Chalhoub & Baker, 2009; Hill *et al.*, 2010)

6.4.2.4 *Disease Onset, Clinical Signs and Necropsy Findings in Mouse Models*

One of the first signs of the disease is subtle weight loss, which, as the disease progresses, turns eventually into cachexia. Abdominal distention can be

observed, which, shortly before the end of life, becomes haemorrhagic ascites. Biliary and small intestine obstruction can occur. Animals adopt a slightly hunched position protecting the abdomen. As the tumour burden increases it becomes less active and stops grooming. KPC mice show the first clinical signs of the disease as early as 10 weeks of age and their median survival rate is 5 months. (Hingorani *et al.*, 2005) KC Pten mice exhibit very similar clinical signs, but have even shorter median survival of 3.5 months. (Hill *et al.*, 2010)

Upon the necropsy the tumour presents itself as hard, fibrotic tissue. Sub-millimetre metastases can be appreciated upon the inspection of liver, sometimes also the diaphragm and lymph nodes. The spleen is generally enlarged, frequently doubled in size.

Thymic lymphoma and lung cancer are occasionally observed in this model. In such cases animal shows difficulty breathing. Those symptoms may coexist with, but usually precede signs of PDAC, and they, not the latter, ultimately lead to the animal's demise.

6.5 Current Treatment of Pancreatic Cancer

The treatment of pancreatic cancer depends very much on the stage of the disease. Pancreatic neoplasms are classified as either locally advanced, locally advanced with lymph node involvement, or advanced with metastatic spread. Their localisation (head, body or the tail of the pancreas) and large blood vessels involvement are also factors considered when treatment plan is drawn.

Treatments can be divided into potentially curative and palliative. The main types of treatment available are:

- Tumour resection,
- Ablative or embolization therapy,
- Radiotherapy,
- Chemotherapy,
- Immunotherapy,
- Chemoradiation therapy,
- Palliative therapy.

Additionally, the treatments may be combined, e.g. chemotherapy can precede or follow tumour resection, which is called neoadjuvant or adjuvant therapy, respectively.

6.5.1 Potentially Curative Resection

The major requirement for potentially curative resection is disease advanced locally, without distant metastases, although metastases onto stomach and duodenum do not disqualify from the operation. Until recently involvement of the major blood vessels within and around a tumour was considered an absolute contraindication for resection, however, this is no longer the case due to improvement in surgical techniques. In any case, the medical state of the patient must be sufficiently good to allow for surgery, but due to late presentation, for many this is not an option.

78% of PDAC tumours involve head, neck and uncinate process of the pancreas (Bond-Smith *et al.*, 2012). For these *pancreaticoduodenectomy* (Whipple procedure) may be used. It consists on removing the affected part of the pancreas along with part of the stomach, distal bile duct, and duodenum while restoring continuity of the gastrointestinal tract by connecting gallbladder, stomach and the remaining part of the pancreas to small intestine. However, within 30 days following the operation up to 40% of patients die due to complications like delayed gastric emptying or pancreatic insufficiency, among others. (Bond-Smith *et al.*, 2012; Yang *et al.*, 2005)

Distal pancreatectomy may be performed when the tumour affects the body and tail of the pancreas. This procedure does not disturb the continuity of the gastrointestinal tract. Like *pancreaticoduodenectomy*, it can be carried out laparoscopically. The most common complication is the leakage of the pancreatic fluid, which causes fistula formation at the resection margin. Hence, the morbidity for this operation can be as high as 28%.

In both cases, patient survival improves, where disease-free resection margin can be achieved. In practice though, it is difficult to accomplish due to the highly infiltrative nature of PDAC cells and pancreatic morphology.

Total pancreatectomy means removing the entire pancreas and spleen. It is sometimes used where cancer affects the head or body of the pancreas and Whipple procedure cannot be performed. Patients after this type of surgery undergo pancreatic hormone and enzyme replacement therapy to combat the inevitable diabetes and lack of digestive enzymes formerly produced by the pancreas. Loss of the spleen makes patients prone to infections.

Bleeding and infections are also a common risk during and after any of those kinds of surgery.

6.5.1.1 *Neoadjuvant and Adjuvant Treatment*

Neoadjuvant (before surgery) chemo- and chemoradiation therapy can reduce tumour burden and allow for the resection of borderline locally advanced disease. It improves also the chance for disease-free resection.

Adjuvant (post-surgery) chemotherapy has been shown to improve patient's survival as compared to chemoradiotherapy, which had the opposite effect as it was shown in the European Study Group for Pancreatic Cancer 1 trial. (Neoptolemos *et al.*, 2004)

6.5.2 Ablative or Embolization Therapy

Tumours may also be destroyed using ablative or embolizing techniques.

Small tumours (up to few centimetres in length) or proximal metastases may be destroyed using ablative treatments as described below.

(American Cancer Society, 2016a)

- Radiofrequency ablation (RFA) uses a thin probe, which is inserted into a tumour. High-energy radio waves emitted from the probe cause a temperature increase within a tumour and cancer cell destruction.
- Microwave thermotherapy uses microwaves to heat up the tumour during procedure that is otherwise like RFA.
- Cryoablation uses thin metal probe to deliver very cold gases to the tumour and freeze cancer cells.

- Irreversible electroporation (NanoKnife) utilizes electric current of high voltage, which is delivered through needles inserted into and around the tumour. (Pancreatic Cancer UK, 2015a)

The procedures listed above may cause internal bleeding, infection or abdominal pain.

Embolization requires a chemical substance to be injected into an artery delivering blood to the tumour to disrupt this blood flow and cause the cancer cells to die and may be used to treat unresectable pancreatic tumours and/or metastatic disease.

- (Trans-)arterial embolization (TAE) requires a catheter to be inserted through a femoral artery, into hepatic artery and into celiac or splenic artery (Tanaka *et al.*, 2012) (depending on the tumour position) and the artery providing blood flow to a tumour is occluded either by microparticles or a coil.
- (Trans-arterial) chemoembolization (TACE) is performed similarly to TAE with the exception that either the beads used to occlude the target artery contain a chemotherapeutic drug or it is delivered using a catheter used for embolization. (Azizi *et al.*, 2011)
- Radioembolization combines radiation therapy with embolization treatment by introducing radioactive microspheres (filled with e.g. ^{90}Y) into a target artery. Radiotherapy is hence delivered locally and the kind of radiation used (β -particles) ensures only the tissues within a small proximity from the microspheres position are destroyed. (Michl *et al.*, 2014)

These procedures can cause side effects in the formation of blood clots, infection, fever, nausea or abdominal pain. (Bond-Smith *et al.*, 2012)

6.5.3 Radiation Therapy

Most commonly high energy x-rays (external beam radiation) are used to treat pancreatic cancer, particularly in patients with unresectable locally advanced

tumours or whose health status makes surgical resection impossible.
(Pancreatic Cancer UK, 2015b)

6.5.4 Palliative Treatment

Palliative treatment involves various approaches to manage symptoms, where the disease progressed beyond the point, where cancer remission can be achieved. (Bond-Smith *et al.*, 2012)

- Obstruction of duodenum or biliary tract is one of the most common problems that can be resolved by surgical or endoscopic stenting, bypass surgery or radiotherapy.
- Exocrine insufficiency, which causes fat malabsorption can be counteracted by supplementing pancreatic enzymes like pancreatin.
- Delayed gastric emptying can be managed by e.g. nasogastric drainage, pro-kinetic medication or nutritional supplementation.

Unresectable tumours or distant metastases can be treated with radiotherapy or chemotherapy to prolong survival and lessen the pain. When the cancer reaches nerves leading to the pancreas it is possible to relieve the pain to the patient by cutting them or injecting with alcohol. (American Cancer Society, 2016b)

Pharmacological pain management is also an option, with opioid medications like morphine being most commonly used.

Immunotherapy using GV1001, a monoclonal antibodies and the telomerase vaccine is currently in clinical trial with the hope that it may prolong survival of patients with unresectable or metastatic disease. (Cancer Research UK, 2015b)

6.5.5 Chemo- and Immunotherapy

6.5.5.1 *Standard Treatment*

Below listed and briefly described are the most common chemotherapeutic drugs used clinically for the treatment of PDAC.

- Gemcitabine is a cytidine analogue, which by being incorporated into the DNA and RNA of the cancer cells can inhibit their proliferation, prevent their repair and in consequence induce apoptosis. It is considered a “golden standard” in the treatment of PDAC; in particular, in the adjuvant therapy and metastatic disease. (Alvarellos *et al.*, 2014; Louvet *et al.*, 2002) Oxaliplatin is platinum-based antineoplastic drug. Through its DNA-crosslinking properties it inhibits DNA synthesis and repair. It is used on its own or in combination with 5-FU, which is called FOLFOX. (Ehrsson *et al.*, 2002)
- Fluorouracil (5-FU) is a pyrimidine analogue and functions as another anti-proliferative compound. It does so by interfering with the synthesis of thymidine via inhibition of the enzyme needed for its production, thymidylate synthase. It is highly toxic and may cause nerve damage. It is being used on its own or in combination with other drugs (e.g. as part of FOLFIRINOX). (Johnston & Kaye, 2001; Longley *et al.*, 2003) Capecitabine is a pro-drug administered orally instead of intravenously, which via enzymatic action of dihydropyrimidine dehydrogenase is converted to 5-FU. (Johnston & Kaye, 2001)
- Paclitaxel interferes with cell division by targeting tubulin. It is an anti-proliferative drug. However, it has severe side effects related to the solvent in which it is formulated. (Horwitz, 1992) Because of this problem alternative formulations were developed. Specifically, protein-bound paclitaxel (known as nab-paclitaxel) uses albumins as a form of paclitaxel delivery intravenously, which causes it to be better tolerated by patients. (Chen *et al.*, 2015; Horwitz, 1992)
- FOLFIRINOX is a combination of four drugs: folinic acid, which helps to reduce side effects of 5-FU; 5-FU; irinotecan, inhibitor of an enzyme responsible for the coiling of the DNA helix and its duplication; and oxaliplatin. It is used in particular in the treatment of the metastatic disease. (National Cancer Institute, 2011)

6.5.5.2 *Immunotherapy*

The purpose of immunotherapy is the utilization of body’s natural defence mechanisms. This is done by introducing antigens specific to the tumour genetic

characteristics. The delivery routes of these vary and include whole cells, dendritic cells, DNA and T-cell receptor vaccines. (Gunturu *et al.*, 2013; Loc *et al.*, 2014)

6.5.5.3 *Clinical Trials*

There are many clinical trials testing novel drugs or vaccines. Many trials compare the drugs currently used to treat patients with PDAC or their various combinations and treatment regimes. They address a broad palette of molecular pathways and targets, and all stages of tumour development and treatment. A recent in-depth overview of those was recently published by Garrido-Laguna and Hidalgo. (Garrido-Laguna & Hidalgo, 2015)

6.6 TGF β

As mentioned above in the section 6.4.1 Mutated Genes and Pathways, one of the pathways affected during the development of PDAC is the TGF β pathway. Transforming Growth Factor beta (TGF β) is one of the cytokines, i.e. small proteins involved in cell signalling. In the context of cancer, it is an important part of inflammatory, proliferative, apoptotic and cell differentiation pathways. (Moustakas & Miyazawa, 2013) It has been shown that in early disease stages that TGF β plays a tumour suppressive role by arresting proliferation and inducing apoptosis via its canonical, i.e. SMAD pathway. (Gaspar *et al.*, 2007; Ten Dijke *et al.*, 2002) SMAD proteins act as transcription factors and are activated by the TGF β receptors. After forming complexes, they are translocated to cell nucleus, where they regulate gene activity (e.g. Tp53). However, at some point this changes and TGF β starts driving cancer by inducing proliferation and aggregation of fibroblasts via its non-canonical pathways, most notably PI3K/AKT. (Ikushima & Miyazono, 2010) This pathway is activated by the tyrosine kinase Src. (Moustakas & Miyazawa, 2013) It can then either induce metastasis, angiogenesis and proliferation via AKT-mTOR activation, which in turn phosphorylates S6 kinase, which is responsible for regulation of the protein synthesis. Alternatively, it can control proliferation via PI3K-Ras-Raf-MEK-MAPK pathway. (Khan *et al.*, 2013; Rozengurt *et al.*, 2014) Generally, in pancreatic cancer TGF β

pathway eventually leads also to the formation of the tumour stroma - a typical feature of many types of pancreatic malignancies. (Apte *et al.*, 2004)

The exact mechanism and reason why TGF β changes its role from tumour suppressor to driver is still speculative. (Akhurst & Derynck, 2001; Ikushima & Miyazono, 2010; Principe *et al.*, 2014) However, it is understood that it has many functions and plays an important role in the epithelial to mesenchymal transition (EMT) (Kabashima *et al.*, 2009), which is an important mechanism leading to cancer cell migration and metastasis. (Kalluri & Weinberg, 2009) Metastatic disease is one of the features of the KRAS and Tp53-driven PDAC. As such, this role of TGF β has already been addressed in few early pre-clinical trials. (Neuzillet *et al.*, 2015) It has also been targeted in few clinical trials for other kinds of cancer. (Buijs *et al.*, 2012)

6.7 ^{18}F -FLT

^{18}F -Fluoro-L-thymidine (^{18}F -FLT) is a thymidine analogue and is used to measure cellular proliferation. Indigenous thymidine is taken up by a cell and phosphorylated using thymidine kinase 1 (TK1). It can be then incorporated into the nuclear DNA. ^{18}F -FLT relies on TK1 as well, but is trapped in the cell as radiolabelled phosphate compound. (Lamarca *et al.*, 2016; Shields *et al.*, 1998) It is therefore a surrogate a measurement of TK1 activity rather than proliferation itself.

^{18}F -FLT has been used in an imaging of pancreatic cancer in number of pre-clinical and clinical studies and is often claimed to be superior in to ^{18}F -FDG in the sense that it is more specific, although some studies show that it may have lower sensitivity than ^{18}F -FDG. (Challapalli *et al.*, 2012; Debebe *et al.*, 2016; Herrmann *et al.*, 2012; Lamarca *et al.*, 2016; Lamarca *et al.*, 2013; Quon *et al.*, 2008; Schober *et al.*, 2013; Shreve, 1998; von Forstner *et al.*, 2008)

6.8 Research Questions

The survival rates of patients presenting with PDAC are so low because diagnosis of the disease generally occurs too late for surgical intervention. Chemo- and/or radiotherapy also bring only marginal benefits in terms of survival, yet have

significant impact upon the quality of patient's life. (Garrido-Laguna & Hidalgo, 2015) Any therapy that could prolong patient's life or improve the quality of her life in the last stages of the disease would be welcomed by the sufferers and their families. Unfortunately, to date, the therapies available failed to deliver significant improvements. This issue has many facets, but the main one would be that PDAC is driven by several genes as described in section 6.4 Genetic Background of Pancreatic Ductal Adenocarcinoma, while the therapies available target specific pathways. Since these pathways relate to specific genes, if the expressed genes do not activate certain pathway, the therapeutic agent will not deliver the anticipated benefits while exposing patients to many adverse effects from chemotherapy.

Many *in vitro* and pre-clinical *in vivo* trials show that therapeutic efficacy of drugs depends on the genes driving the disease. The latter relies on animal models, which KPC and KC Pten mouse models are example of. Both models recapitulate well human PDAC, and although they show similar clinical signs and survival, they are being driven by different pathways. Finding therapeutic approaches that work in those mouse models is the key to help a subset of patients, whose tumours are driven by the same genes.

Even though it has been established that TGF β plays an important role in tumourgenesis, the exact circumstances upon which it switches its function from tumour-suppressing to tumour-driving are not well understood. However, since its pathway is active throughout the cancer development, TGF β presents itself as an attractive therapeutic target that could potentially arrest the switch from benign tumours to aggressive carcinoma *in situ* and further - the metastatic spread.

7 Aims and objectives

7.1 mTOR Inhibitor study

The mTOR pathway has been previously shown to be driving PDAC in the sub-set of tumours lacking tumour suppressing Pten gene. (Kennedy *et al.*, 2011; Thorpe *et al.*, 2015) The aim of the study was to compare the efficacy of mTOR inhibitor Rapamycin in KC Pten and KPC mouse models of PDAC. This was done by conducting *in vitro* and *in vivo* experiments, which were all a collaborative effort. Shown and discussed here are the results of the *in vivo* study using ¹⁸F-FLT PET/CT, which compares proliferation in those mouse models before and after treatment.

7.2 TGFB Study

The aim of the TGFB antibodies study was to assess if combining anti-TGFB antibody with Gemcitabine would be more effective than Gemcitabine monotherapy in the treatment of PDAC. This was done by observing its acute (24±2h post-injection) effect on proliferation using ¹⁸F-FLT and *ex vivo* techniques like gamma counting, autoradiography and Ki68 immunohistochemistry.

8 Methods

8.1 mTOR Inhibitor Study

8.1.1 Study Design

Two cohorts of mice (n=3) were compared. All animals were genetically engineered using Cre-Lox system to conditionally express or delete genes within Pdx-1 (pancreatic and duodenal homeobox1 promoter) expressing tissues. The first group expressed mutated Kras in one allele and lacked Pten on both alleles: $Kras^{G12D/+}$; $Pten^{-/-}$; Pdx1-Cre and will be henceforth called KC Pten. The control cohort expressed mutated Kras and Tp53 genes on one of the alleles and wild-type copies of those genes on the other one: $Kras^{G12D/+}$; $Tp53^{R172H/+}$; Pdx1-Cre (henceforth called KPC).

8.1.2 Treatment Regime and Sampling

Upon detecting palpable tumour and confirming the finding by ultrasound (Vevo770 System with 35 MHz Real-Time Micro Visualisation VisualSonics scanhead), mice were imaged using PET/CT (Bruker Albira tri-modal PET/SPECT/CT system with 2-ring PET) and ^{18}F -FLT to establish base-line proliferation profile. Subsequent treatment commenced with mice receiving intraperitoneal injections: daily of rapamacin (10 mg/kg) or vehicle, and/or of gemcitabine (100 mg/kg) twice weekly. After four days of treatment the second PET/CT imaging study was conducted. Mice were then sacrificed and necropsy conducted. Tumours were excised, fixed in 10% buffered formalin solution, paraffin-embedded and then sectioned. H&E and Ki67 staining was performed on the section near the middle of the tumour.

8.1.3 PET/CT Protocol

To establish a baseline and the best time-point for imaging, the first mouse was anaesthetised using a mixture of 5% isoflurane and medical air, and intravenously (i.v.) injected with 3.33 MBq of ^{18}F -FLT via tail vein. It was then

placed on the imaging bed and imaged for a continuous period of 3h using dynamic PET protocol containing a series of 1 min frames and followed a CT scan (600 projections, 45 kV, 0.2 mA).

Subsequent mice were, under anaesthesia, injected with 6-8 MBq each of ^{18}F -FLT to compensate for the decay over the 2h (conscious) uptake period. They were then imaged using a static, 1h PET scanning protocol (40 mm bed offset) followed by the 2-bed-position CT (600 projections, 35 kV, 0.4 mA, 25 mm bed offset). The subsequent scans were changed to single bed CT protocol and the offset was adjusted to 40 mm, so the abdomen was clearly visible within the FOV.

8.1.4 Data Analysis

PET/CT images were reconstructed using the Albira Reconstructor software using the default reconstruction parameters: MLEM 12 iterations, $80\times 80\times 94$ FOV, $1\times 1\times 0.944$ mm voxel size for PET images, and FBP $0.25\times 0.25\times 0.25$ mm voxel size for CT ones. Reconstructed images were analysed using PMOD software and after the co-registration feature was used to ensure good alignment between the pictures. CT images did not have enough soft tissue contrast to delineate organs within the abdominal cavity. However, they were used as a reference on which lungs could be easily identified and from there liver could be found. Since the tracer is excreted with urine, it accumulates in the bladder, which was hence outlined: first a 3D ball slightly bigger than the bladder was drawn (preview tool allowing for tracking the VOI appearance in all directions was used to align it) and next threshold it to 10% of the hottest pixel within the FOV to focus it only over the bladder. The inspector tool was used to inspect the uptake values around the bladder, so when the VOI contains only bladder a masking tool can be used to mask this volume using an average uptake value from the tissues around.

In the next stage, hot spots were searched for within the abdomen and VOIs were manually drawn on each image slice to contain those hot spots.

8.2 Gamma counter experiments

8.2.1 Calibration

Starting with 3.0, 3.0 and 3.05 MBq three dilution series (log2) were prepared. The volume of the individual sample was 0.6 ml and was placed in 1.5 ml screw-top vials. Before the start of the experiment 2-3 empty cassettes were measured to acquire background counts and ensure there was no residual contamination on the cassettes. All samples were then loaded onto gamma counter (Packard Cobra II, Perkin-Elmer, Waltham, MA, US) and counting started using pre-set protocol no 7, set up for ^{18}F and which has three energy windows defined:

- 15 to 2000 keV,
- 311 to 711 keV,
- 722 to 1222 keV,

Counting time was 1 min.

Decay-corrected activity was calculated for each vial using ^{18}F half-life and an actual time each sample was measured.

8.2.2 Sample volume experiment

Background counts were acquired as above. A known activity (50 kBq at a reference time) was prepared in 1.5 ml screw-top vials in a range of volumes, from 100 ml to 1500 ml, every 100 ml in triplicate. The samples were then measured three times using gamma counter (1 min counting time). Counts from the energy window of 311 to 711 keV and 15 to 2000 keV were decay-corrected to the reference time. For each volume, the counts were averaged and standard error of the mean calculated. A line was fitted to these data points to show if there is a linear relationship between the counts measured depending on the volume of the sample.

A ratio of the counts measured in the 15 to 2000 keV and 311 to 711 keV was also calculated using non-decay-corrected data.

8.3 TGF β Antibody

8.3.1 Study Design

The effects of an anti-TGF β antibody were observed in a cohort of KPC mice, which were divided into two groups: mice, which received a single i.p. injection of Gemcitabine and mice, which received a single dose of Gemcitabine like the first group and at the same time were injected also with anti-TGF β antibody. 24 \pm 2 hours following the first injection the mouse was injected with a dose of ^{18}F -FLT i.v. After 2 more hours animals were sacrificed and following tissues harvested for gamma counting. Tissues marked with asterisk (*) from the list below were also assessed using autoradiography:

- blood,
- heart,
- lungs,
- spleen,
- kidney,
- stomach,
- small intestine,
- large intestine,
- tumour *,
- liver *,
- muscle,
- brain.

Gamma counting, autoradiography and Ki67 staining were performed on all or a sub-set of the samples. For technical reasons (problems during ^{18}F -FLT production, broken cryostat or film processor) it was not always possible to complete all three tests on all the mice in the study - details were gathered in Table 10.

Table 10 Summary of the number of mice used in the study and tests conducted on harvested samples

Protocol	Gamma counting	Autoradiography	IHC	All three completed
Ctrl WT	9	6	10	6
Gem	8	7	10	7
Gem + α -TGFB	8	7	10	7
Gem + ab10517	5	5	5	5
Gem + ab64715	3	2	5	2

8.3.2 Treatment Regime

Mice in the treatment group were given a single injection of Gemcitabine (100 mg/kg) intraperitoneally (i.p.) or the same dose of Gemcitabine with the additional injection of 100 μ g of anti-TGFB antibody (ab10517 or ab10517, Abcam, Cambridge, UK) via the same route. This treatment was administered 24 \pm 2h before the scheduled experiment. Table 11 shows the details of the age of mice used in the experiment in each of the sub-groups, their average weights and average dose of 18 F-FLT, which mice received prior to being sacrificed.

Table 11 Summary of an average mice age, weight and the dose of 18 F-FLT administered

Protocol	Avg Age [days]	Avg Activity [MBq]	Avg weight [g]
Ctrl WT	125.1	9.3	25.9
Gem	114.5	9.0	26.4
Gem + α -TGFB	124.8	9.4	26.8
Gem + ab10517	146.8	9.5	27.5
Gem + ab64715	102.8	9.3	25.5

8.3.3 Gamma Counting

Gamma counting was performed using Packard Cobra II (Perkin-Elmer, Waltham, MA, US; Figure 30) and pre-set protocol, which defines three energy windows to distinguish between all, true and scattered events:

- 15 to 2000 keV,
- 311 to 711 keV,
- 722 to 1222 keV.

Measurement time for each sample was 60 s and the latency between samples was 40 s. Before the start of the experiment 2-3 empty cassettes were measured to acquire background counts and ensure no residual contamination on the cassettes is present. All samples were placed during dissection in the screw-top 1.5 ml tubes and loaded onto cassettes. After choosing an appropriate command on the computer screen, the samples were measured automatically. Before experiment tubes containing PDAC tumour, liver, small and large intestine, were additionally filled with 0.5 ml of 10% buffered formalin since those samples were later passed for histological processing. All tubes were pre-weighed before the experiment and again after the gamma counting (after an overnight storage which allowed for the radioactivity to decay away to background levels). Subtraction of the pre- and post-weights allowed for the determination of the organ weight.

For each mouse between the time of the injection with ^{18}F -FLT and animal sacrifice three controls were prepared in 0.5 ml of PBS:

- negative control,
- 1/100 of the injected dose,
- 1/200 of the injected dose.

The negative control provided a volume-adjusted background measurement value, which was used to calculate actual counts for each tissue. The activities within each excised organ expressed in kBq or percentage of the injected dose could be found using the latter two controls.

Correcting for the decay of ^{18}F , normalizing for mouse weight and injected dose (described below), counts per gram of tissue could be calculated for all sampled organs. All results were automatically printed by the attached dot matrix printer and written down from the computer screen into an Excel worksheet (as shown in the Appendix).



Figure 30 Cobra II Gamma Counter with samples loaded onto cassettes and photon counting process in progress. On the right perforated paper hangs from the dot-matrix printer, which prints the results in real-time. The last 10 results are also displayed on the computer screen.

8.3.4 Autoradiography

Parts of the pancreatic and liver tissue were frozen at the time of the dissection using cryo-spray and transported on dry ice out of the animal facility into the Histology laboratory. An empty and clean sample disk was placed inside the microtome cryostat chamber, which was set to -20°C . After a few minutes during which it cooled down, a small amount of OCT (optimal cutting temperature) compound was poured onto it to cover the area slightly bigger than a sample that was to be cut. When OCT started to solidify (indicated by the change of colour from transparent to white) the sample was placed on top of the disk, so it became partially embedded in OCT and stuck to it. Then more OCT was poured around the sample to create, after solidification, a frozen block with the sample embedded in it. Care was taken to fill any cavities and avoid air bubbles that could disrupt the smoothness of the cutting process and, in effect, damage the cut section.

When the OCT with the embedded sample froze, the sample disk was mounted in the cryostat microtome rig (Leica CM1950, Leica Microsystems, Milton Keynes, UK). A few $100\ \mu\text{m}$ sections were cut using the coarse setting to expose the deeper layers of the tissue. Then sections of the same thickness were cut using the fine setting and gently transferred onto positively charged slides (Surgipath Snowcoat range, Leica Microsystems, Milton Keynes, UK) with care taken to avoid sample rolling, breaking, folding or creases. Each slide was placed in the plastic slide storage box ensuring sufficient space between the slides. When all slides containing cut sections from a given mouse were cut, the box was taken to a dark room and transferred to a light-tight cassette. A photographic film was subsequently applied (Kodak Biomax MR, Carestream Health, Rochester, NY, US) under dim red light and the cassette closed. Each cassette was then additionally put in a black, light-tight sleeve and placed in a -20°C freezer in a controlled-access radiation room.

After overnight storage, which allowed for a decay of ^{18}F to a background level, each cassette was opened in the dark room and film was developed using an automatic X-ray film processor. Developed autoradiography films from each experiment were later scanned using BioRad GS-800 Calibrated Densitometer (BioRad Laboratories, Hemel Hempstead, UK) and Quantity One 1-D Analysis

Software (the same vendor as the densitometer) and, using the same software, every scan was then exported as TIFF image and saved onto portable media drive.

Each TIFF image was opened in ImageJ software, version 1.4 (National Institutes of Health, Bethesda, Maryland, US). (Rasband, 1997-2016) Five rectangular regions of interest (ROI) were drawn using the Rectangular Selection tool. Next, ten ROIs were drawn for each tissue (liver or PDAC) using the Freehand Selection tool (Figure 31). All ROIs were added to the ROI Manager plugin in which Set Measurement option was selected and the following options chosen: Area, Mean (within the area), StdDev, Max and Min. After clicking "Measure" in the ROI Manager the measurements were taken and then saved to an Excel spreadsheet. The representative values for the investigated tissues were calculated by averaging measurements of all ten ROIs and by subtracting the average of the background ROIs. Results for all mice were then summarised in a separate spreadsheet, where normalization (described below) was performed.

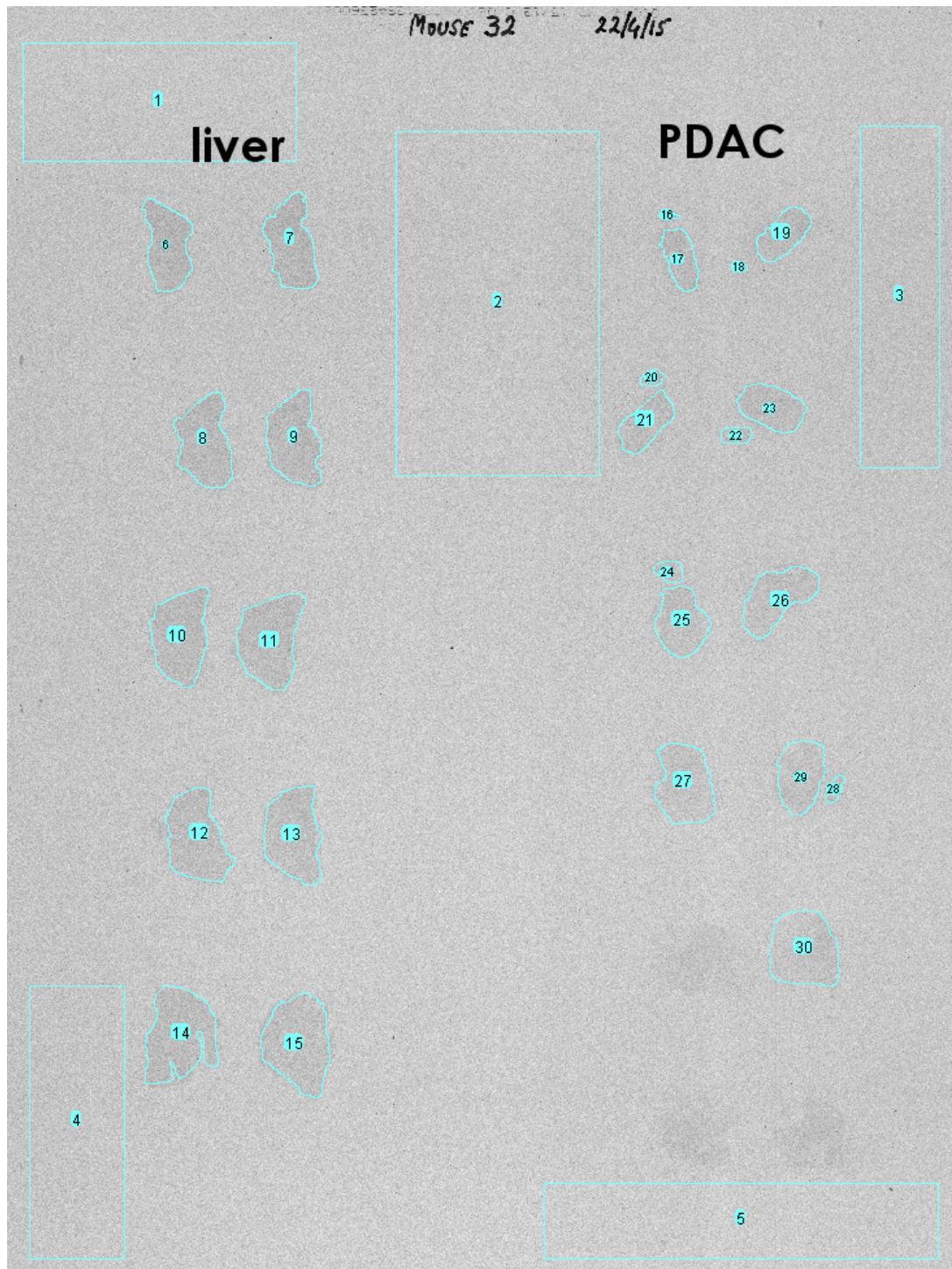


Figure 31 An example scan of an autoradiography film presenting images of 100 μm sections of liver and pancreas along with the regions of interest chosen in the analysis process in ImageJ software

8.3.5 Ki67

Formalin-fixed paraffin-embedded tissue (tumour or liver) was cut into 4 μm sections. Sections were then deparaffinised and stained using an automated protocol on Autostainer Link 48 (Dako, Ely, UK). The antibodies and reagents used were as follows:

- primary antibody - anti-Ki67 (SP6 RM-9106, Thermo Fisher Scientific, Waltham, MA, US), dilution 1/100,
- amplification step - Rabbit Envision kit (Dako, Ely, UK),
- visualisation substrate - liquid DAB (3,3' diaminobenzidine) peroxidase substrate (Dako, Ely, UK)
- counterstain - Gill's Haematoxylin (RHS-335, CellPath, Newtown, UK).

From each sample one section from the middle was cut and stained. It was then scanned in full at 20x magnification using a slide scanner (SCN400F, Leica Biosystems, Milton Keynes, UK) and uploaded onto a digital image server operating within the local network.

New Tissue Image Analyser protocols were defined. Their details for tumour and liver tissues are given in Table 12. Each slide was manually evaluated and ROIs containing tissues either to include (actual liver, pancreatic or tumour) in or exclude (fat, lymph nodes, small intestine, etc.) from the analysis were selected. Once this was done for few slides, they were selected for batch processing, defined protocol was selected and the job submitted to the server. If the sample contained healthy and cancerous areas, both were used in analysis. Only the areas not containing liver or pancreatic/tumour tissues were excluded.

After the job was processed, an output CSV file could be generated. The value used in the comparative analysis among animals subjected to the investigated treatments was a percentage of the positively-stained nuclei, which reflects the Ki67-expressing (i.e. proliferating) nuclei.

Table 12 Details of the Leica Tissue IA automatic scoring protocol defined and used for the assessment of PDAC and liver tissues stained with anti-Ki67 antibody

Data Input Parameter	PDAC	Liver
0= μm , 1=mm, 2=pixels	0	0
Segment Tissue from Background by Intensity	170	170
0=Nuclei are similar, >=1, Nuclei increasingly diverse (darkest to lightest)	2	3
0=Strong Nuclear Counterstaining, 2=Weak Nuclear Counterstaining	2	2
Values in units	37	37
Eliminate nuclei with area outside this range (specified in units squared)	0	0
Eliminate nuclei with density outside this range	0	0
Eliminate nuclei with nuclear area density outside this range (specified in units squared)	0	0
Eliminate cells with area outside this range (specified in units squared)	0	0
Values in units	100	100
Above this value pixels are identified as negative	200	200
Eliminate nuclei with a % below this value	10	10
Identify nuclei having strong/moderate/weak staining intensity	99	99
Above this value pixels are identified as negative	220	220
Eliminate areas with a % below this value	75	75
Identify areas having strong/moderate/weak staining intensity	160	160
Above this value pixels are identified as negative	220	220
Eliminate areas with a % below this value	75	75
Identify areas having strong/median/weak staining intensity	160	160
0 = Include All Cells, 1 = Include only Positive Cells, 2 = Include only Negative Cells	0	0
0 = Include All Cells, 1 = Include only Positive Cells, 2 = Include only Negative Cells	0	0
0 = Include All Cells, 1 = Include only Positive Cells, 2 = Include only Negative Cells	0	0
Default Calibration	1	1
File Input Parameter	Name	
Colour Definition File	deconvolution-Haematoxylin	
Colour Definition File	deconvolution-DAB	

8.3.6 Normalization

Before effects of the selected treatment could be compared it was necessary to normalize the results of gamma counting and autoradiography measurements to consider the weight of the mouse and dose of the radiotracer administered. The approach adopted was like the calculation of the standard uptake value (SUV) used in the analysis of PET images, in particular in the clinical practice, where the weights of patients may vary significantly. On the PET image the value measured is the concentration of the trapped and free tracer (and its radio-labelled metabolites) in each volume of interest (VOI), e.g. an organ or part of it. For example, in the Albira the reconstructed PET images in microPET format are calibrated to display kBq per cc.

SUV is defined as follows:

$$SUV_t = \frac{A_t}{ID} w,$$

where subscript t denotes value at a given time, A - activity concentration measured on an image, ID - injected dose and w - weight.

The normalized value, expressed as SUV is therefore a measured value (in this case, an activity concentration) multiplied by a factor calculated as a ratio of patient or subject weight to injected dose.

In a similar fashion one can calculate normalized values of gamma counts per gram of tissue or optical density measured over certain region of interest (area) on autoradiography images of all investigated tissues. Ki67 staining does not depend on the weight of the mouse, neither does it depend on the dose of ¹⁸F-FLT and therefore does not require normalization.

8.3.7 Statistical Data Analysis

Statistical analysis of the data was performed by Dr. Gabriela Kalna from the Computational Biology and Bioinformatics team in the CR UK Beatson Institute. The normalized counts per gram calculated as explained above were log₂-transformed and analysed considering two factors - type of tissue and treatment

protocol. The empirical Bayes adjusted p-values and fold changes were calculated using R package limma. (Ritchie *et al.*, 2015; Smyth, 2004)

9 Results

9.1 mTOR Inhibitor Study

Figure 32 highlights the challenges posed by the low soft-tissue contrast encountered in CT imaging. Some organs could be approximately delineated based on the anatomical reference posed by the skeletal structure. Some (e.g. duodenum or bladder) are visible slightly better due to the natural contrast provided by the water. It is not possible, however, to tell with certainty where do the edges of the liver lie, where are kidneys, spleen, and stomach. More importantly for this experiment, it is also not possible to distinguish the PDAC tumour from the surrounding small and large intestine. One can see that the abdominal cavity does not have uniformly grey appearance. Yet it may be difficult to interpret the findings based on CT alone. For example, one can see that there are places in the abdomen that appear black. This may be simply gas trapped in the gastro-intestinal tract, but can indicate as well, a tumour that has a cyst.

Figure 33 presents the fused PET/CT image of a KC Pten mouse (same as above) injected with ^{18}F -FLT and imaged using dynamic PET over 3 hours followed by the CT. The image was created by averaging all the 1-min acquisitions over the last hour of the PET scan to reduce noise. Most of the tracer and its metabolised accumulated in the bladder, therefore a VOI around the bladder was drawn and masked to the average level of activity immediately outside it. This removed very high activity concentrations from the image and allowed for better visual contrast on the image, which immediately revealed PDAC tumour. The outline of the liver is also visible on the sagittal slice of the image.

Figure 34 shows the time activity curves for liver and PDAC. Beyond 60 min liver uptake stabilizes, while in the tumour raises all the way until the end of the scan. At 60 min, in fact, the uptake in both organs appeared to be the same, which would make it very difficult to distinguish them if the scan was stopped then. After the second hour of the scan the difference in the uptakes should be clearly visible, which the previous image (Figure 33) is an example of.

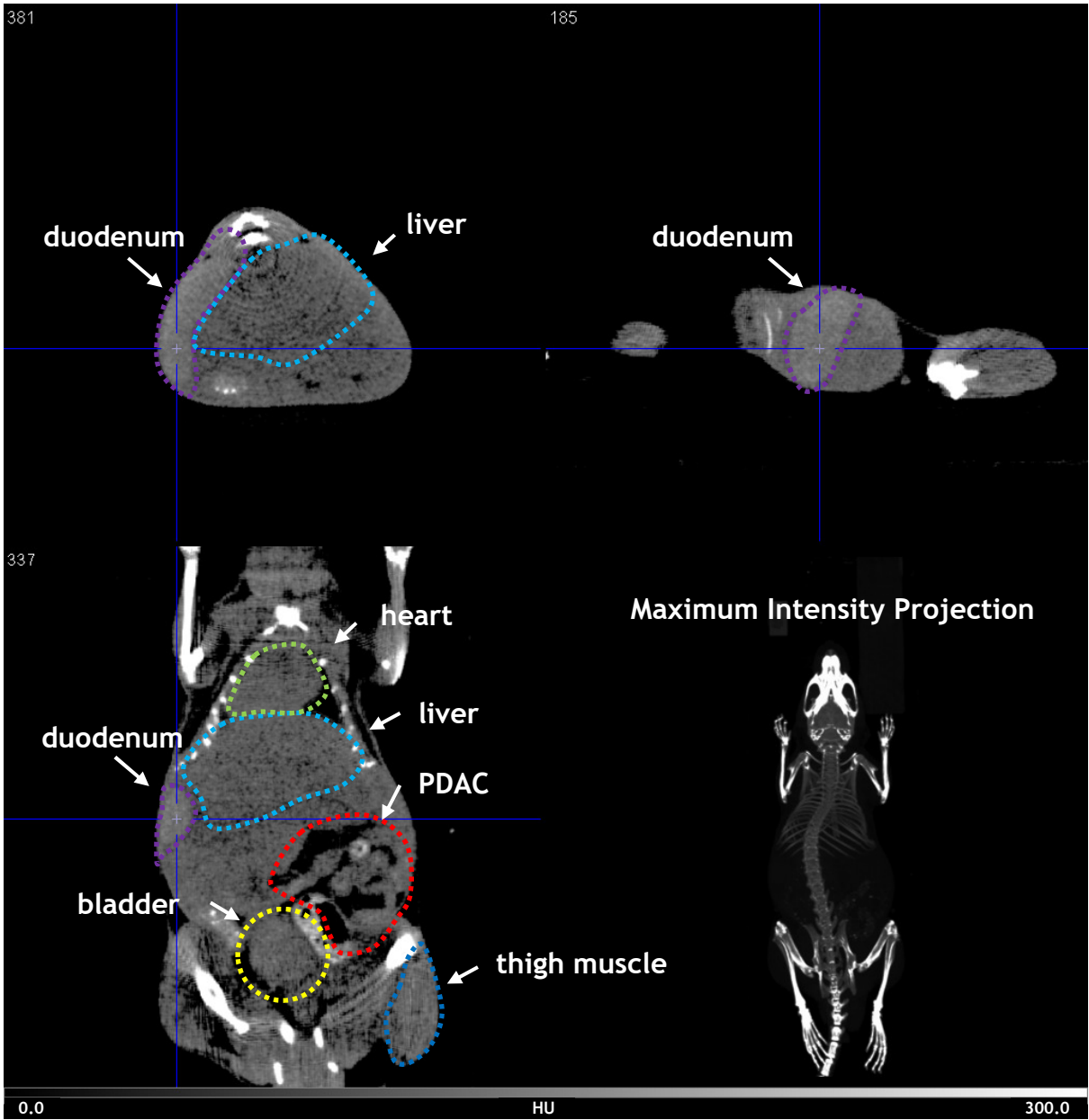


Figure 32 CT image of the mouse injected with ^{18}F -FLT. Soft-tissue contrast does not allow for the accurate distinction among particular organs. However, based on the skeletal structure, which is clearly visible, one can approximate their position.

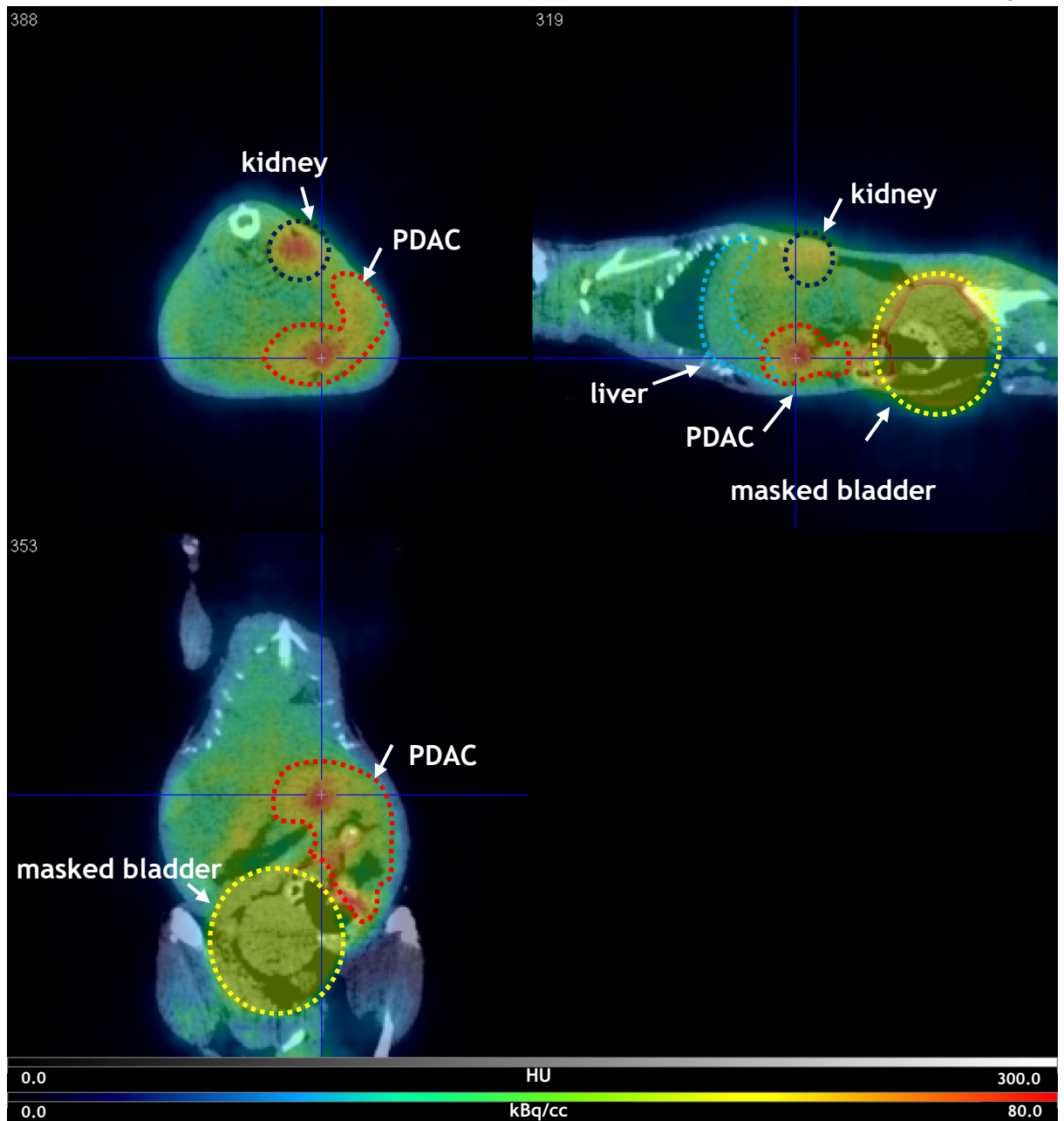


Figure 33 Fused PET/CT image on which bladder was masked with uniform, low-density volume. This led to the enhancement of the PET image contrast and made the tumour a prominent feature that would otherwise be difficult to distinguish from the surrounding high-proliferative intestine.

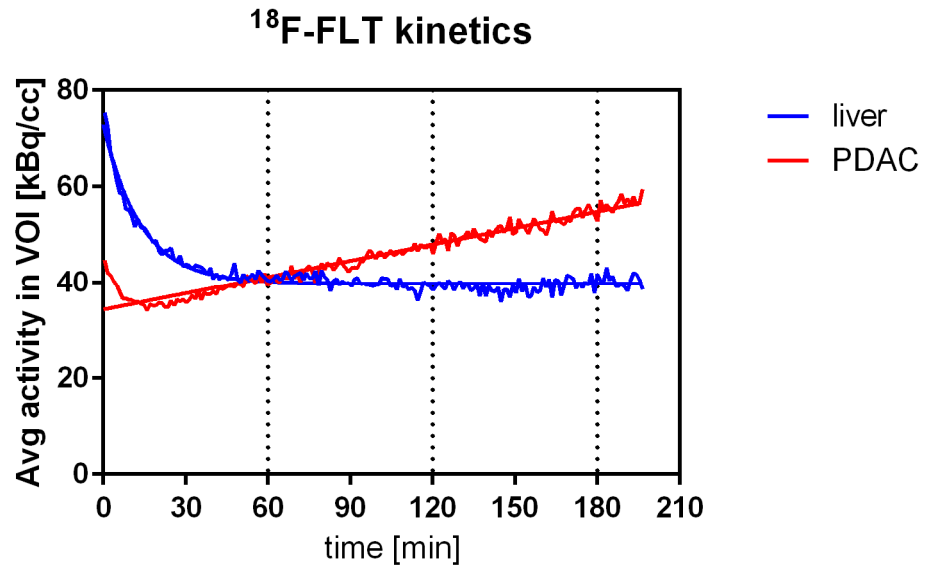


Figure 34 Time-activity curves presenting average activity (kBq/cm^3) for liver and tumour measured over a period of over 3h using 1 min frames.

Figure 35 to Figure 37 present the effects of mTOR inhibitor treatment on KC Pten mouse using different modalities, ^{18}F -FLT PET/CT, H&E and Ki67 IHC.

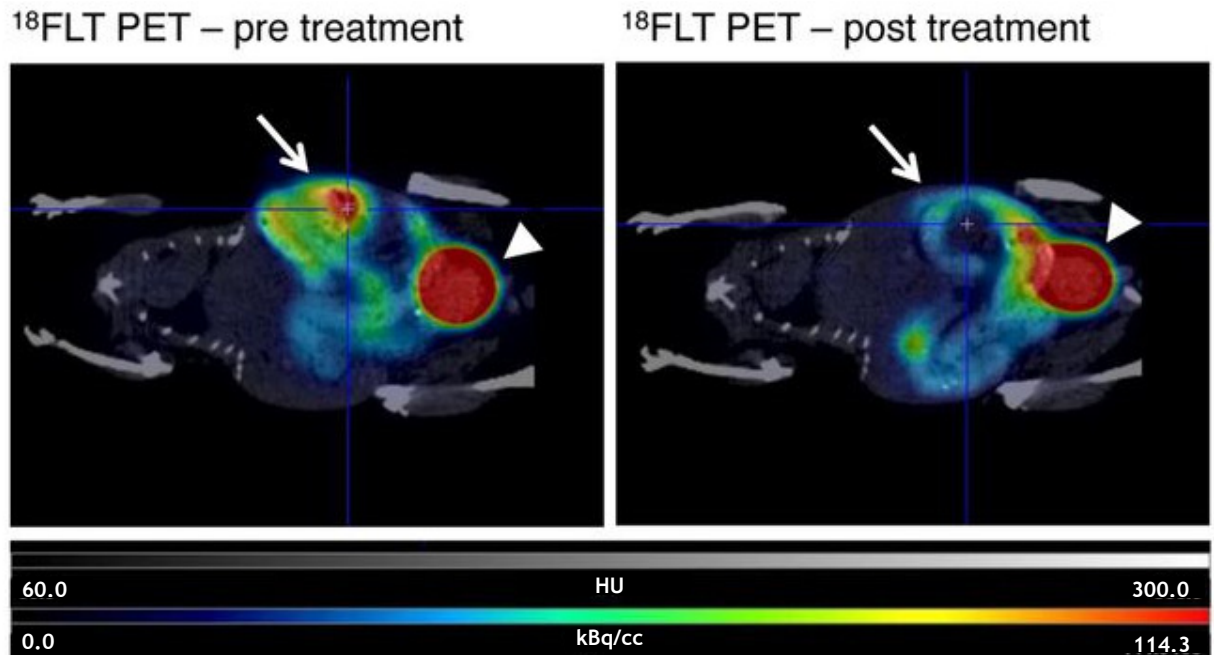


Figure 35 PET/CT image of KC Pten mouse treated with rapamycin and injected intravenously with ^{18}F -FLT. Long arrow points to PDAC tumour, while the other marker shows the accumulation of the tracer in the bladder. Picture taken from (Morran *et al.*, 2014).

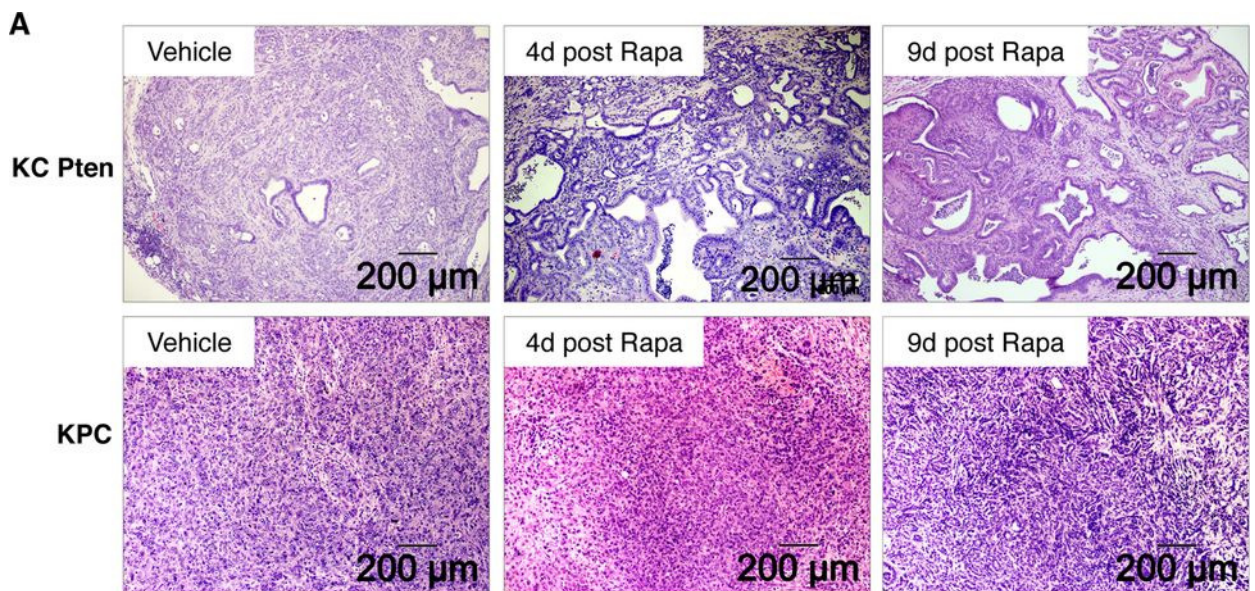


Figure 36 H&E staining presenting the effects of rapamycin treatment on PDAC tumours spontaneously developed by mice of two distinct genetic backgrounds. Picture taken from (Morran *et al.*, 2014).

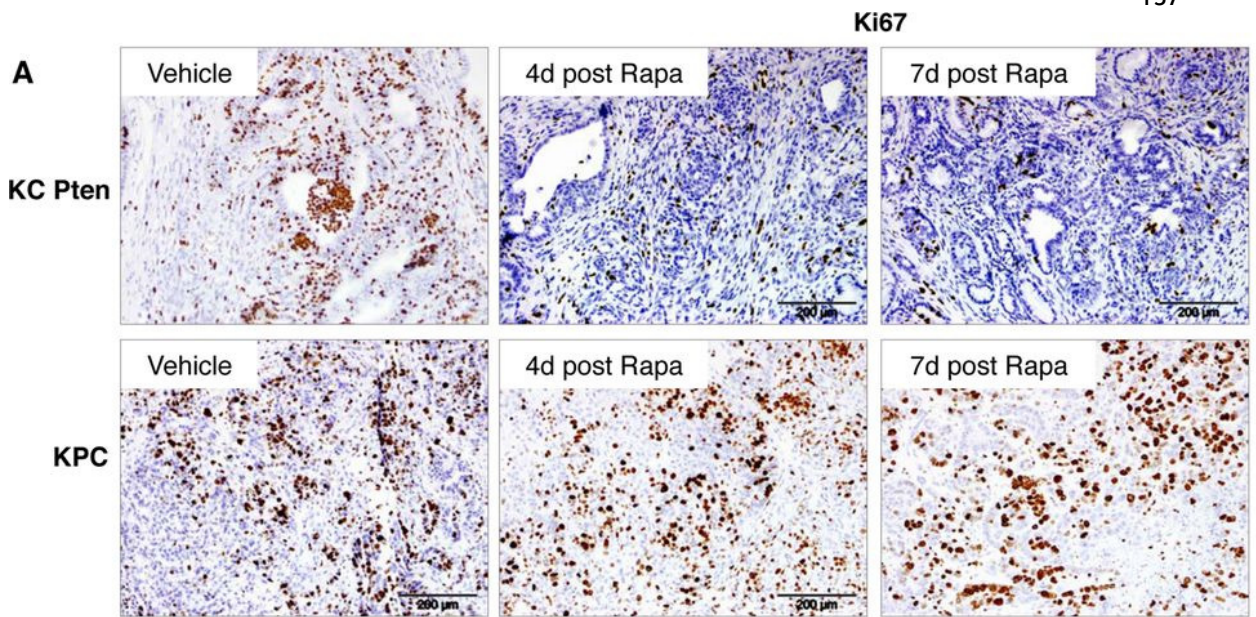


Figure 37 Ki67 staining on pancreatic adenocarcinoma tissues presenting the effects of rapamacin treatment on tumour proliferation in KC Pten and KPC mice. Picture taken from (Morran *et al.*, 2014).

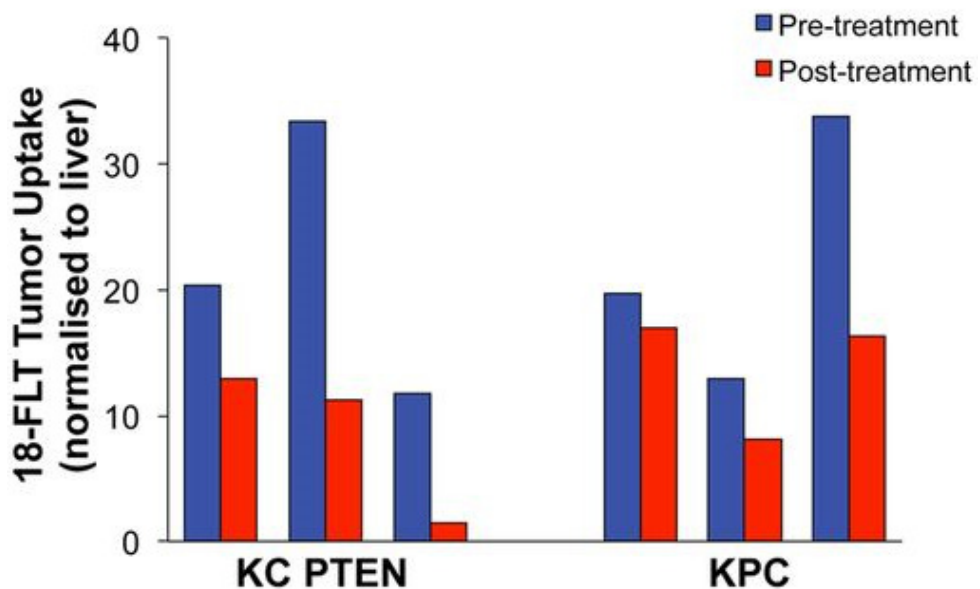


Figure 38 Tumour uptake of ^{18}F -FLT measured on PET image as maximum pixel value and normalised to liver. The graph shows individual results for two cohorts of three mice (KC Pten and KPC) before and after rapamacin treatment. Graph taken from (Morran *et al.*, 2014).

9.2 Gamma counter Calibration

9.2.1 Calibration

Figure 39 presents counts measured within one minute from three dilution (\log_2) series. Each measurement consists of counts registered in one of three (partially overlapping) energy windows. The activity of each sample is presented as decay-corrected to account for the time elapsed between the time when samples were prepared and the time of measurement. Samples higher in the dilution series and of activity above ca. 300 kBq (at the time of measurement) are not shown on the plot as they fall outside the resolution of the gamma counter, i.e. lead to the detector saturation and subsequent computer freeze. Within the measured range, however, i.e. 275 kBq to 80 Bq the counts showed good linearity within all three energy windows.

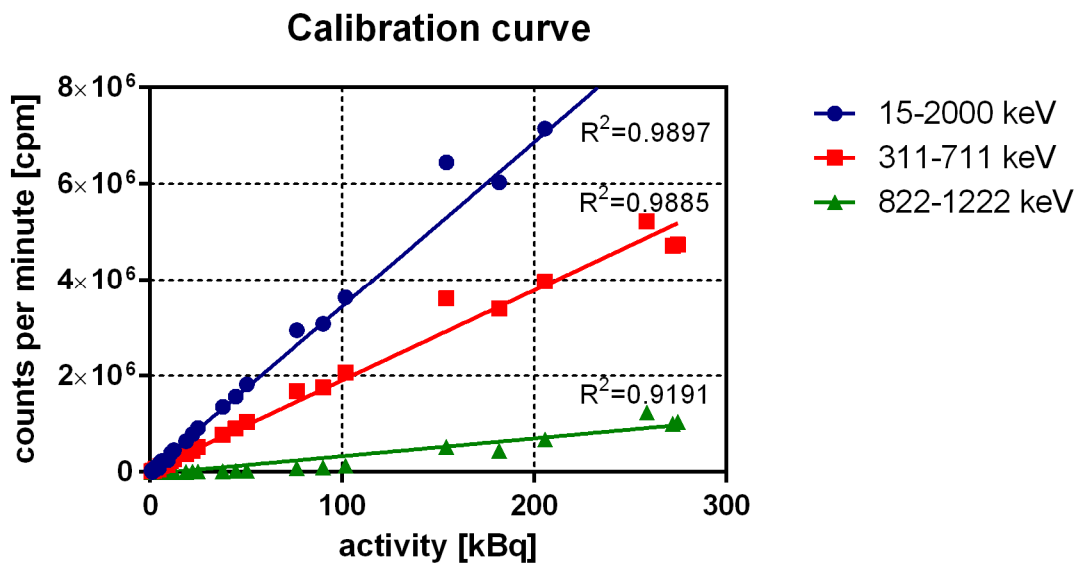


Figure 39 Calibration curve showing linear relationship within the measured range of activities within three energy windows.

9.2.2 Sample volume

Figure 40 shows how the ratio between the counts measured in the energy window of 15 to 2000 keV and 311 to 711 keV changes. The relationship is exponential with $R^2 = 0.98$. Figure 41 summarizes how the sample volume impacts the measured number of photons. Individual points are the average of triplicate samples prepared within the given volume and the error bars reflect the standard error of the mean within those three samples. All data points were decay-corrected and the almost horizontal line is a linear fit of all points shown.

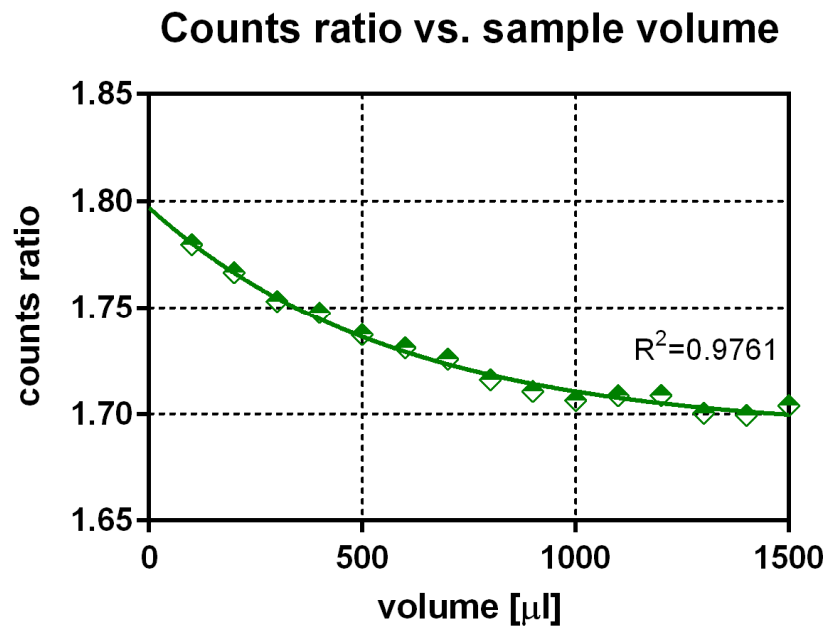


Figure 40 The ratio of counts in the energy window of 15 to 2000 keV to those in 311 to 711 keV depending on the volume of the sample.

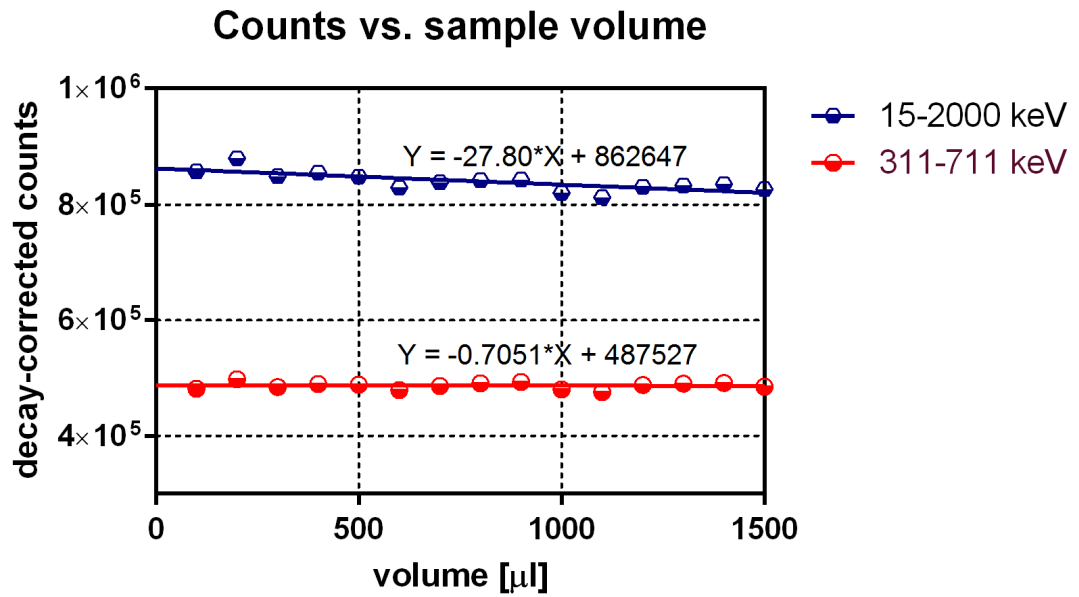


Figure 41 Relationship between the sample volume and measured counts. The linear fit is nearly horizontal, which means that within the range measured (100-1500 μl) the sample volume has very little effect on gamma photons measured by the counter.

9.3 TGF β Antibody Study

9.3.1 Gross Anatomy

Figure 42 to Figure 47 present examples of gross anatomy findings at necropsy, which reflect the heterogeneity of PDAC in mice, but also in men. Shown conditions may have impact on variable results of the experiment.



Figure 42 Large pancreatic cyst filled with fluid surrounded by fibrous tumour stroma.

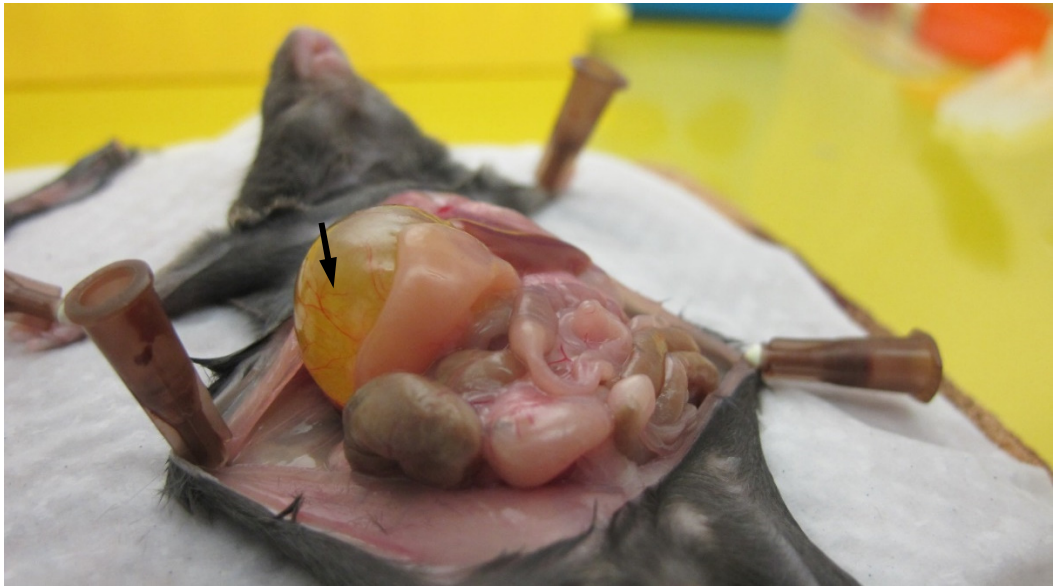


Figure 43 Blocked bile duct leading to its subsequent dilation and jaundice.



Figure 44 Tumour encapsulating enlarged spleen.

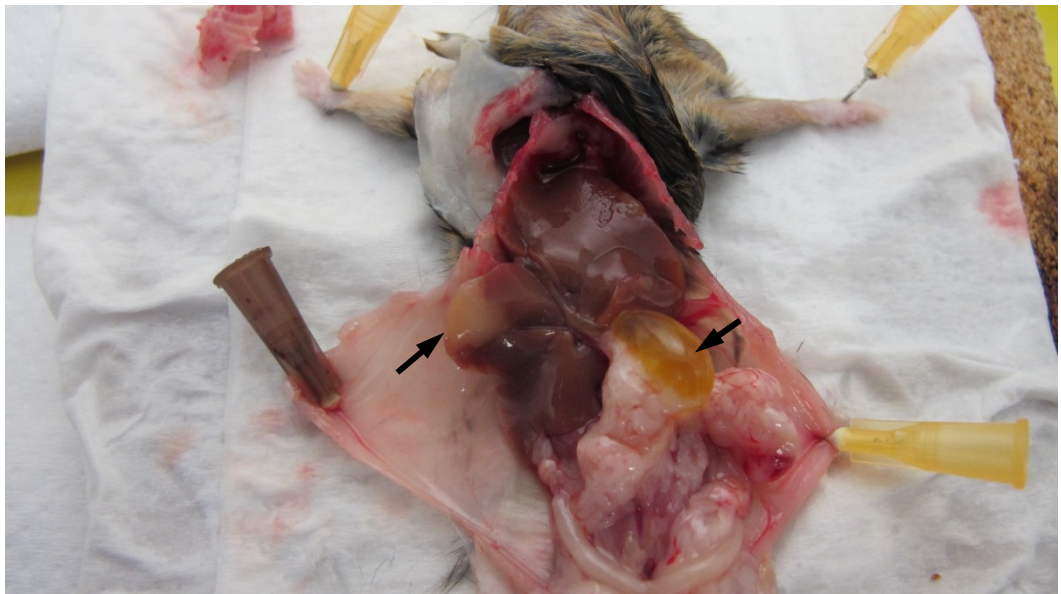


Figure 45 Blocked bile duct and macroscopic liver metastases.



Figure 46 Tumour cells blocking part of the duodenum causing retention of bile within it.

Tables 13 to 24 correspond to individual organs measured using the gamma counter. The tables present the results of the Bayesian t-test performed on the samples. Mice are grouped into cohorts and those cohorts are compared with each other. Subsequent columns show log₂ of fold change between the average result for the compared cohorts and p-value as the measure of statistical significance. Since the p-value between the cohorts treated with different antibodies is for all organs greater than 0.5 it can be assumed that there is no statistically significant difference between the effects of those antibodies measured by the gamma counting and therefore those antibodies can be pooled together. In the last two rows of each table the comparison is made between the cohort made up of all mice treated with the antibody and either untreated, or gemcitabine-only treated groups.

Figure 47 summarizes the biodistribution of ¹⁸F-FLT and its metabolites measured using the gamma counter. Four groups of mice are distinguished, i.e. untreated, gemcitabine monotherapy and gemcitabine with one of two antibodies-treated. This figure confirms the results of the analyses provided in the above tables, specifically that there is not enough evidence to support the existence of a statistically significant difference (or lack of it) between the pairs of compared cohorts for any of the sampled organs.

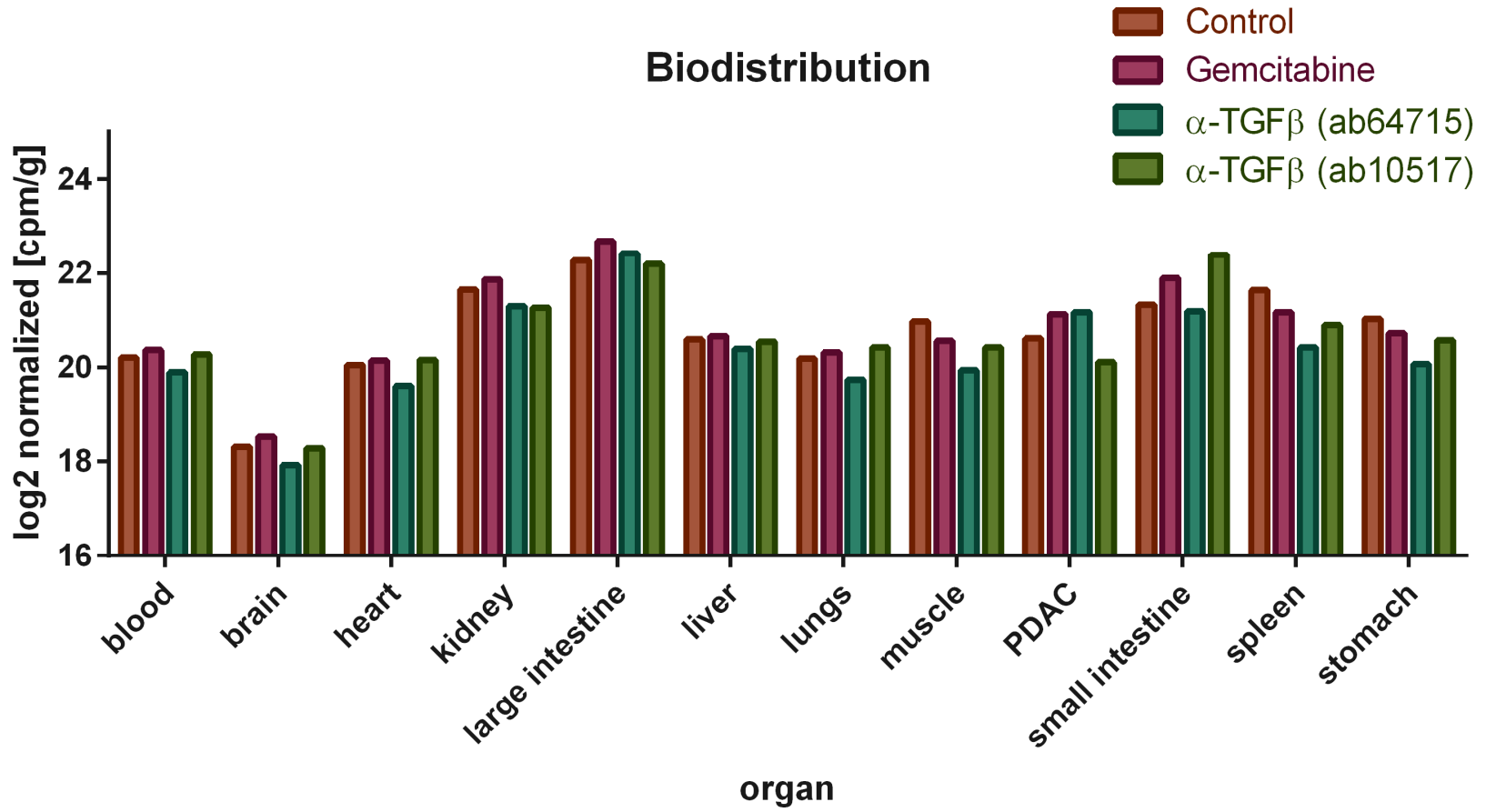


Figure 47 Biodistribution of ¹⁸F-FLT and its metabolites 2hrs after injection as measured by the gamma counter.

Table 13 Liver

Cohort 1	Cohort 2	log ₂ FC	p value
Gemcitabine	Untreated control	0.07013	0.9196
Gemcitabine + ab64715	Untreated control	-0.1987	0.8349
Gemcitabine + ab10517	Untreated control	-0.0432	0.9568
Gemcitabine + ab64715	Gemcitabine	-0.2688	0.7813
Gemcitabine + ab10517	Gemcitabine	-0.1134	0.8894
Gemcitabine + ab10517	Gemcitabine + ab64715	0.1554	0.8816
Gemcitabine + antibody	Untreated control	-0.1787	0.9403
Gemcitabine + antibody	Gemcitabine	-2.6464	0.2854

Table 14 PDAC

Cohort 1	Cohort 2	log ₂ FC	p value
Gemcitabine	Untreated control	0.5103	0.5047
Gemcitabine + ab64715	Untreated control	0.5513	0.5989
Gemcitabine + ab10517	Untreated control	-0.5059	0.5642
Gemcitabine + ab64715	Gemcitabine	0.0410	0.9692
Gemcitabine + ab10517	Gemcitabine	-1.0161	0.2606
Gemcitabine + ab10517	Gemcitabine + ab64715	-1.0571	0.3593
Gemcitabine + antibody	Untreated control	-0.1094	0.8856
Gemcitabine + antibody	Gemcitabine	-0.6197	0.4307

Table 15 Blood

Cohort 1	Cohort 2	log ₂ FC	p value
Gemcitabine	Untreated control	0.1647	0.8114
Gemcitabine + ab64715	Untreated control	-0.3105	0.7432
Gemcitabine + ab10517	Untreated control	0.0690	0.9307
Gemcitabine + ab64715	Gemcitabine	-0.4752	0.6218
Gemcitabine + ab10517	Gemcitabine	-0.0958	0.9059
Gemcitabine + ab10517	Gemcitabine + ab64715	0.3795	0.7148
Gemcitabine + antibody	Untreated control	-0.0733	0.9143
Gemcitabine + antibody	Gemcitabine	-0.2381	0.7343

Table 16 Brain

Cohort 1	Cohort 2	log ₂ FC	p value
Gemcitabine	Untreated control	0.2188	0.6827
Gemcitabine + ab64715	Untreated control	-0.3794	0.6056
Gemcitabine + ab10517	Untreated control	-0.0269	0.9650
Gemcitabine + ab64715	Gemcitabine	-0.5982	0.4240
Gemcitabine + ab10517	Gemcitabine	-0.2457	0.6955
Gemcitabine + ab10517	Gemcitabine + ab64715	0.3525	0.6613
Gemcitabine + antibody	Untreated control	-0.1591	0.7633
Gemcitabine + antibody	Gemcitabine	-0.3779	0.4882

Table 17 Heart

Cohort 1	Cohort 2	log ₂ FC	p value
Gemcitabine	Untreated control	0.0918	0.8992
Gemcitabine + ab64715	Untreated control	-0.4493	0.6518
Gemcitabine + ab10517	Untreated control	0.1072	0.8975
Gemcitabine + ab64715	Gemcitabine	-0.5412	0.5928
Gemcitabine + ab10517	Gemcitabine	0.0154	0.9856
Gemcitabine + ab10517	Gemcitabine + ab64715	0.5565	0.6101
Gemcitabine + antibody	Untreated control	-0.1015	0.8874
Gemcitabine + antibody	Gemcitabine	-0.1933	0.7933

Table 18 Kidney

Cohort 1	Cohort 2	log ₂ FC	p value
Gemcitabine	Untreated control	0.2142	0.7311
Gemcitabine + ab64715	Untreated control	-0.3547	0.6783
Gemcitabine + ab10517	Untreated control	-0.3833	0.5925
Gemcitabine + ab64715	Gemcitabine	-0.5689	0.5133
Gemcitabine + ab10517	Gemcitabine	-0.5975	0.4157
Gemcitabine + ab10517	Gemcitabine + ab64715	-0.0286	0.9756
Gemcitabine + antibody	Untreated control	-0.3726	0.5445
Gemcitabine + antibody	Gemcitabine	-0.5868	0.3555

Table 19 Large intestine

Cohort 1	Cohort 2	log ₂ FC	p value
Gemcitabine	Untreated control	0.5125	0.4267
Gemcitabine + ab64715	Untreated control	0.2507	0.7553
Gemcitabine + ab10517	Untreated control	0.0227	0.9733
Gemcitabine + ab64715	Gemcitabine	-0.2619	0.7553
Gemcitabine + ab10517	Gemcitabine	-0.4898	0.4974
Gemcitabine + ab10517	Gemcitabine + ab64715	-0.2280	0.7927
Gemcitabine + antibody	Untreated control	0.1082	0.8531
Gemcitabine + antibody	Gemcitabine	-0.4043	0.5229

Table 20 Lungs

Cohort 1	Cohort 2	log ₂ FC	p value
Gemcitabine	Untreated control	0.1357	0.8477
Gemcitabine + ab64715	Untreated control	-0.4439	0.6475
Gemcitabine + ab10517	Untreated control	0.2392	0.7682
Gemcitabine + ab64715	Gemcitabine	-0.5796	0.5569
Gemcitabine + ab10517	Gemcitabine	0.1034	0.9007
Gemcitabine + ab10517	Gemcitabine + ab64715	0.6830	0.5213
Gemcitabine + antibody	Untreated control	-0.0170	0.9807
Gemcitabine + antibody	Gemcitabine	-0.1527	0.8322

Table 21 Muscle

Cohort 1	Cohort 2	log ₂ FC	p value
Gemcitabine	Untreated control	-0.4059	0.61580
Gemcitabine + ab64715	Untreated control	-1.0352	0.3532
Gemcitabine + ab10517	Untreated control	-0.5507	0.5534
Gemcitabine + ab64715	Gemcitabine	-0.6293	0.5767
Gemcitabine + ab10517	Gemcitabine	-0.1448	0.8785
Gemcitabine + ab10517	Gemcitabine + ab64715	0.48451	0.6900
Gemcitabine + antibody	Untreated control	-0.7324	0.3612
Gemcitabine + antibody	Gemcitabine	-0.3265	0.6909

Table 22 Small intestine

Cohort 1	Cohort 2	log ₂ FC	p value
Gemcitabine	Untreated control	0.5673	0.4415
Gemcitabine + ab64715	Untreated control	-0.1408	0.8889
Gemcitabine + ab10517	Untreated control	1.0703	0.2093
Gemcitabine + ab64715	Gemcitabine	-0.7081	0.4901
Gemcitabine + ab10517	Gemcitabine	0.5030	0.5601
Gemcitabine + ab10517	Gemcitabine + ab64715	1.2110	0.2765
Gemcitabine + antibody	Untreated control	0.6161	0.4049
Gemcitabine + antibody	Gemcitabine	0.0488	0.9486

Table 23 Spleen

Cohort 1	Cohort 2	log ₂ FC	p value
Gemcitabine	Untreated control	-0.4676	0.4179
Gemcitabine + ab64715	Untreated control	-1.2169	0.1293
Gemcitabine + ab10517	Untreated control	-0.7370	0.2682
Gemcitabine + ab64715	Gemcitabine	-0.7493	0.3523
Gemcitabine + ab10517	Gemcitabine	-0.2694	0.6897
Gemcitabine + ab10517	Gemcitabine + ab64715	0.4799	0.5791
Gemcitabine + antibody	Untreated control	-0.9169	0.1134
Gemcitabine + antibody	Gemcitabine	-0.4493	0.4444

Table 24 Stomach

Cohort 1	Cohort 2	log ₂ FC	p value
Gemcitabine	Untreated control	-0.2992	0.6365
Gemcitabine + ab64715	Untreated control	-0.9611	0.2721
Gemcitabine + ab10517	Untreated control	-0.4512	0.5352
Gemcitabine + ab64715	Gemcitabine	-0.6619	0.4541
Gemcitabine + ab10517	Gemcitabine	-0.1520	0.8376
Gemcitabine + ab10517	Gemcitabine + ab64715	0.5099	0.5921
Gemcitabine + antibody	Untreated control	-0.6424	0.3079
Gemcitabine + antibody	Gemcitabine	-0.3432	0.5946

9.3.2 Autoradiography

Tables 25 and 26 gather results of a Bayesian t-test for liver and PDAC measured using autoradiography. Again, there is not enough evidence to confirm or disprove the existence of the statistically significant difference among the organs in question between any of the pairs of cohorts.

Table 25 Liver

Cohort 1	Cohort 2	log ₂ FC	p value
Gemcitabine	Untreated control	1.1183	0.1920
Gemcitabine + ab64715	Untreated control	0.9301	0.4251
Gemcitabine + ab10517	Untreated control	0.7655	0.3860
Gemcitabine + ab64715	Gemcitabine	-0.1882	0.8675
Gemcitabine + ab10517	Gemcitabine	-0.3528	0.6740
Gemcitabine + ab10517	Gemcitabine + ab64715	-0.1645	0.8868
Gemcitabine + antibody	Untreated control	0.8125	0.3087
Gemcitabine + antibody	Gemcitabine	-0.3058	0.6833

Table 26 PDAC

Cohort 1	Cohort 2	log ₂ FC	p value
Gemcitabine	Untreated control	0.7433	0.3291
Gemcitabine + ab64715	Untreated control	0.1595	0.8779
Gemcitabine + ab10517	Untreated control	0.2529	0.7476
Gemcitabine + ab64715	Gemcitabine	-0.5838	0.5663
Gemcitabine + ab10517	Gemcitabine	-0.4904	0.5165
Gemcitabine + ab10517	Gemcitabine + ab64715	0.0934	0.9283
Gemcitabine + antibody	Untreated control	0.2262	0.7493
Gemcitabine + antibody	Gemcitabine	-0.5171	0.4449

9.3.3 Ki67

Figure 48 to Figure 52 show example results of the anti-Ki67 IHC. Because the results showed no clear difference in the Ki67 expression among the treated and untreated specimen, those images are given as an example of typical Ki67 pattern observed in PDAC in KPC model, including liver metastasis and intestines.

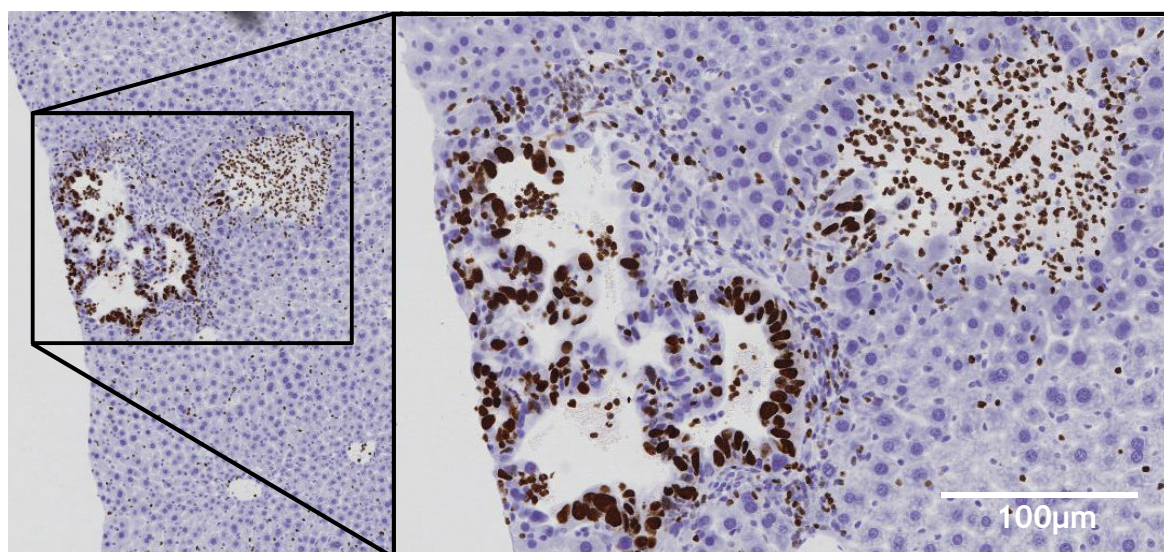


Figure 48 Liver metastasis in a mouse treated with anti-TGF β antibody (x4 & x20 magnifications)

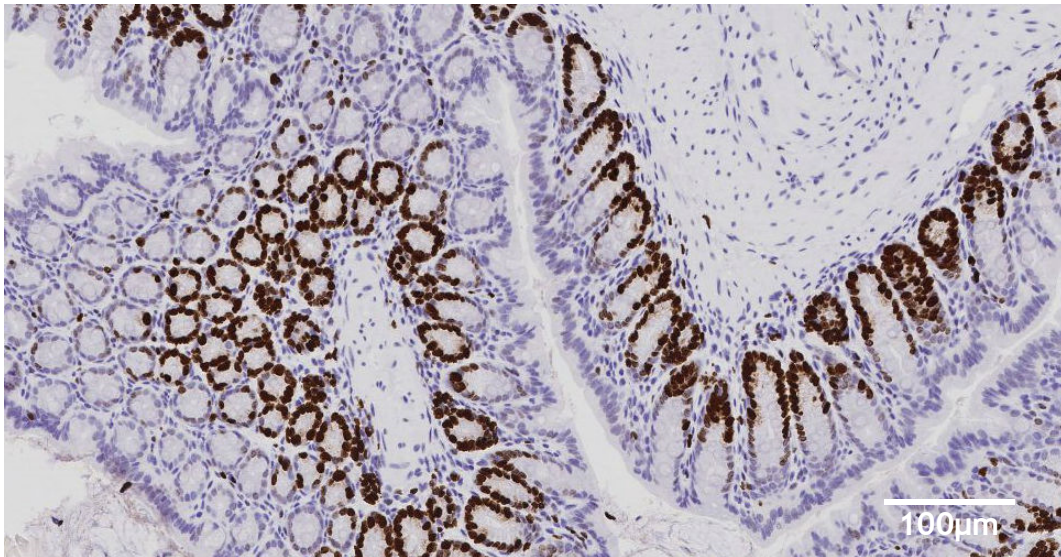


Figure 49 Example expression of Ki67 in large intestine (x10 magnification)

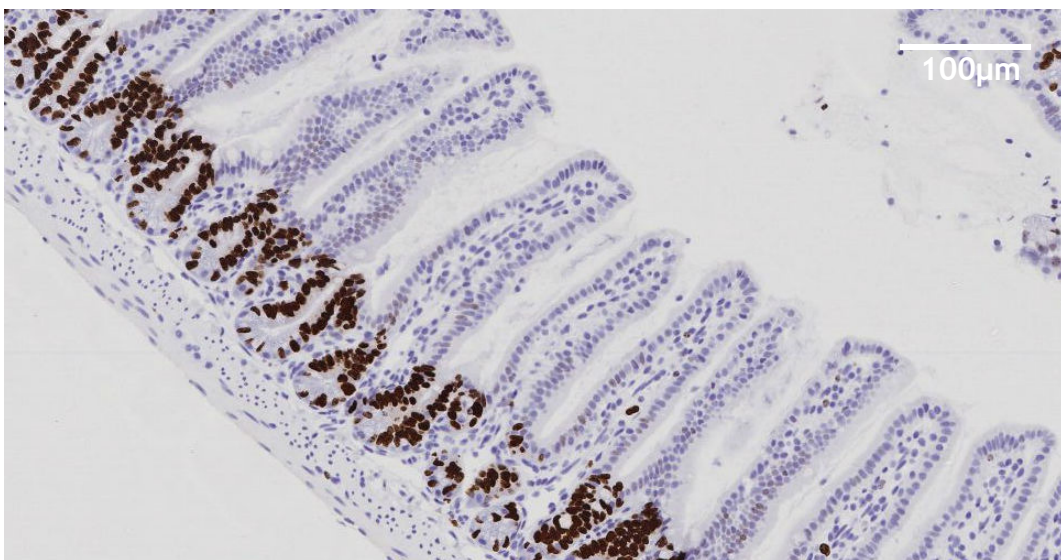


Figure 50 Example expression of Ki67 in the small intestine (x10 magnification)

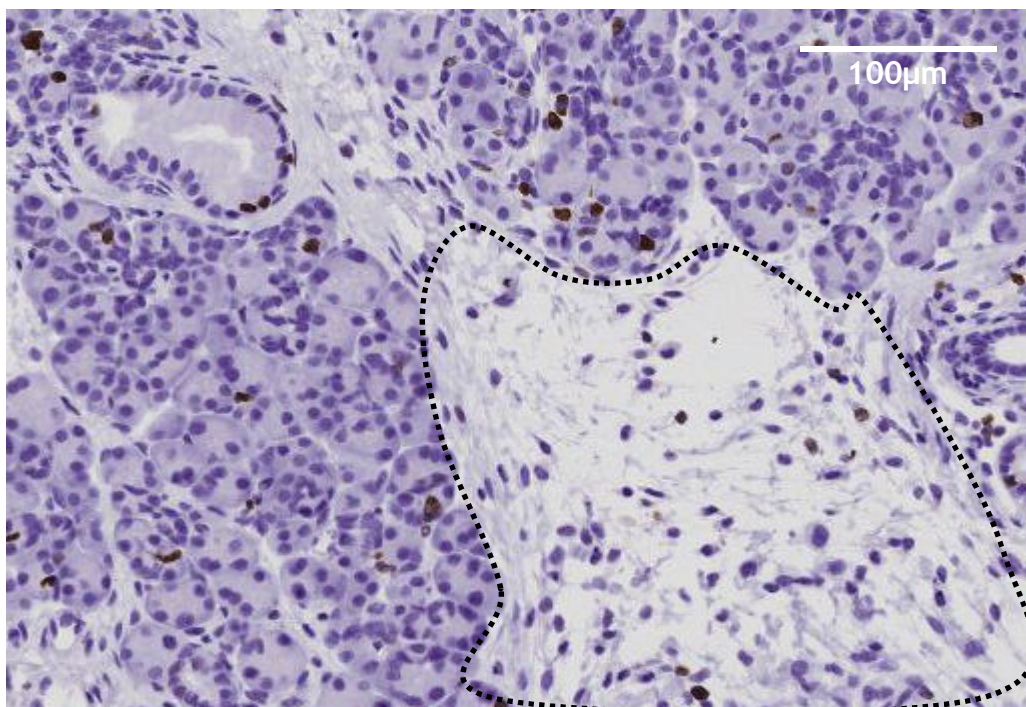


Figure 51 Ki67 expression in the PDAC tumour showing still some normal acinar cells and with highlighted region (dotted line) of desmoplasia (x20 magnification).

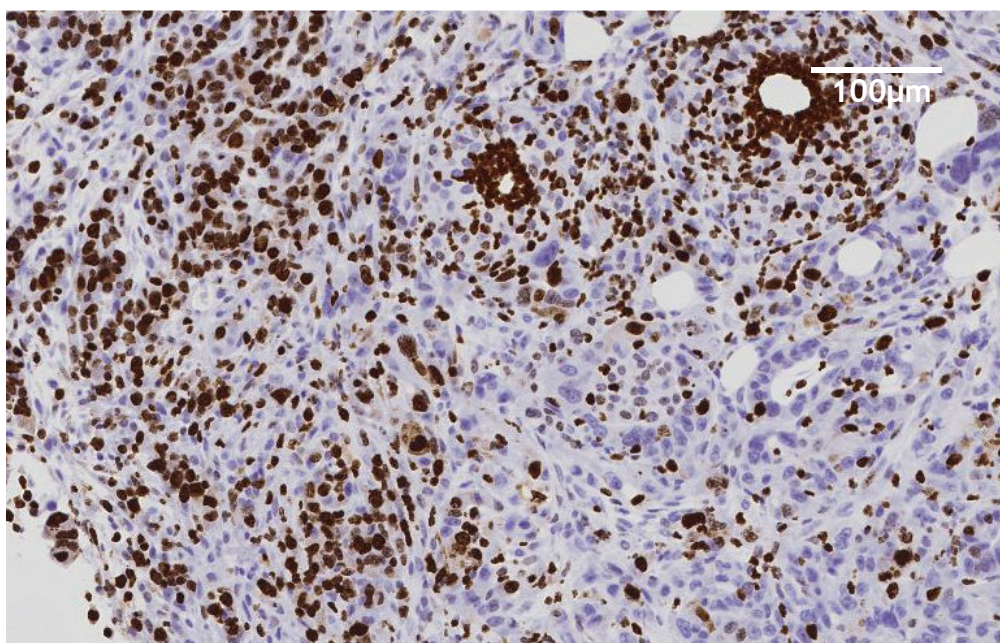


Figure 52 Ki67 expression of Ki67 in the untreated advanced PDAC tumour (x10 magnification)

Figure 53 presents a screen-shot of the metadata file containing the results of the analysis of the sample using automated Leica Tissue IA tool.

Leica
BIOSYSTEMS

About Contact My Profile Logout

Welcome Meg Pajak

Location: Browse > Root > Meg Pajak (Local Image Server) > liver > View Image Metadata > collection_0000001070_2015-06-02 19_22_54.scn

Browse Search Conference Tissue IA

Metadata Annotations Files

File Information

Thumbnail:

- no categories -

Wholeslide Image Analysis Results: Measure Stained Cells Algorithm

Job Reference Number	797
Run By	Meg Pajak
Run On	2015-06-04 11:39:24
Merged Result For Annotations	yes
Measurement Units	µm
Total Tissue Area (in measurement units squared)	23,813,552.75
Total Number of Cells	416,934
Cellular H-Score For Nuclear Staining	6
Total Number Of Accepted Nuclei	416,934
Number Of Negative Nuclei	405,255
% Of Negative Nuclei	97.20
Number Of Positive Nuclei	11,679
% Of Positive Nuclei	2.80
Number Of Weak Intensity Nuclei	431
% Of Weak Intensity Nuclei	0.10
Number Of Moderate Intensity Nuclei	11,248
% Of Moderate Intensity Nuclei	2.70
Number Of Strong Intensity Nuclei	0
% Of Strong Intensity Nuclei	0.00
Average Nuclear Staining Intensity (Positive Area Only)	167.11
Average Nuclear Staining Absorbance (Positive Area Only)	14
% Of Positive Nuclear Area In Tissue	1.66

System generated metadata

Attribute	Value
base_magnification	20
calibration	0.5
file_name	collection_0000001070_2015-06-02 19_22_54.scn

Create New Category Show Library

Figure 53 Example output data of the automatic Tissue IA tool.

In Tables 27 and 28 are shown the results of the Bayesian t-test of the percentage of the positively-stained (proliferating) nuclei within the sample. As marked, only two cohorts show some statistical difference in the liver: gemcitabine monotherapy group and the gemcitabine with the TGF β -antibody ab10517 show lower proliferation when compared with the untreated control. No analogous (or

otherwise) evidence emerges from the analysis of the PDAC/pancreas samples that would support or fail to support that significant difference exists among any of the treatment groups.

Table 27 Liver

Cohort 1	Cohort 2	log ₂ FC	p value
Gemcitabine	Untreated control	-0.5579	0.0623
Gemcitabine + ab64715	Untreated control	-0.4765	0.1530
Gemcitabine + ab10517	Untreated control	-0.9920	0.0260
Gemcitabine + ab64715	Gemcitabine	0.0814	0.9871
Gemcitabine + ab10517	Gemcitabine	-0.4341	0.4214
Gemcitabine + ab10517	Gemcitabine + ab64715	-0.5155	0.5261
Gemcitabine + antibody	Untreated control	-0.7629	0.9403
Gemcitabine + antibody	Gemcitabine	-0.2050	0.2854

Table 28 PDAC

Cohort 1	Cohort 2	log ₂ FC	p value
Gemcitabine	Untreated control	-0.3188	0.3165
Gemcitabine + ab64715	Untreated control	-0.4258	0.7659
Gemcitabine + ab10517	Untreated control	-0.6071	0.9006
Gemcitabine + ab64715	Gemcitabine	-0.1071	0.6500
Gemcitabine + ab10517	Gemcitabine	-0.2884	0.3481
Gemcitabine + ab10517	Gemcitabine + ab64715	-0.1813	0.7156
Gemcitabine + antibody	Untreated control	-0.5266	0.9289
Gemcitabine + antibody	Gemcitabine	-0.2078	0.3679

Figure 54 gathers the results of all three methods of measuring proliferation in the livers or pancreata of the mice belonging to any of the sub-groups specified above.

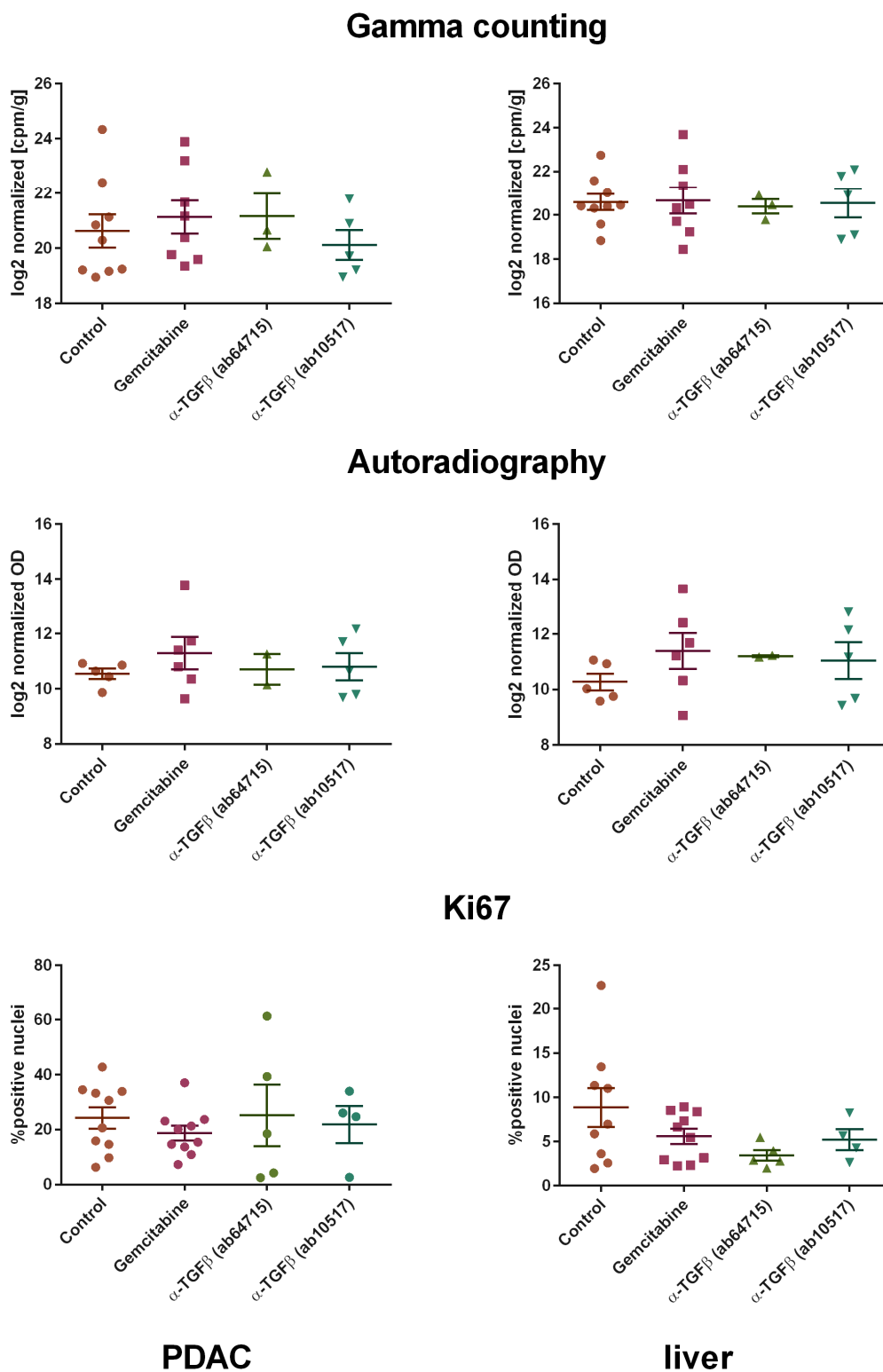


Figure 54 Summary of the acute effects of anti-TGF β on KPC mice. Each row of graphs presents results obtained using a different technique, which can be used to complement and validate PET imaging. Control denotes untreated mice. Refer to Table 10 for the sample size in each of the groups.

10 Discussion

10.1 mTOR

The investigation of mTOR inhibition in two distinct cancer models used both *in vitro* and *in vivo* approaches to characterize effects of rapamacin on PDAC. *In vitro* studies were conducted by Douglas Morran and aimed at understanding the mechanisms of action of rapamacin on pancreatic cancer tumour cells, which are not fully understood. Discussed below is the *in vivo* part of the study, which involved PET/CT imaging and data analysis.

The results of the PET/CT imaging complement well the *in vitro* results in that rapamacin showed beneficial effects on mice of KC Pten phenotype, but none on the KPC ones. This is in concordance with the *in vitro* results and the experimental hypothesis. The use of ^{18}F -FLT allowed for visualisation of proliferation in the tumour, which was expected to be negatively affected by rapamacin. Indeed, that appeared to be the case for KC Pten mice that were imaged.

However, PET imaging posed a set of challenges that needed to be overcome during the study. First of them was the interpretation of the PET image after reconstruction, i.e. identifying the tumour position on the image. The reason for this initial confusion was that ^{18}F -FLT is non-specific in its way that it labels proliferating cells. Because of it all abdominal cavity showed significant signal, mostly in the bladder, where the probe metabolites accumulated. In the first step then a VOI was drawn around the bladder, threshold set up as described in the Methods section and all counts inside were masked. That drastically changed the appearance of the image and allowed for distinguishing subtler features in that area. The tumour wasn't readily visible also for another reason, namely, because of the signal from mouse intestines, which also proliferate.

The way to deal with this interference was to aid the PET image interpretation by overlaying it onto CT image. This allowed for broad understanding of the placement of major organs. Brain and lungs showed no signal on PET image and their position could easily be verified using mouse's skeleton as an anatomical

frame. When it comes to the mouse's abdomen, however, the soft tissue contrast could hardly distinguish individual organs. Visible were the areas of low Hounsfield numbers as compared to the surrounding tissues that could be interpreted as trapped gas. Tumour position could be approximated looking at the outline of the body of the mouse. Knowledge of the mouse anatomy was also useful. To start with, healthy pancreas in a mouse can be found below liver and stomach and is connected to the duodenum, which in the mouse's right side. Healthy pancreas can be excised from the animal by removing first the intestines with which it is connected. Normal spleen is placed below stomach, on mouse's left side. Because all subjects were in advanced stage of their illness, they exhibited number of symptoms like abdominal distension. Additionally, their tumours grew large enough to have fibrous stroma and often, necrotic core. By analysing the area of the image between the approximate position of the liver and the bladder, one could often notice how the tumour bulk shifts the bladder off its normally central position in the pelvis. When analysing the fused image, by connecting the above clues it was possible to confirm that the areas of higher signal in untreated mice indeed correspond to the tumour.

Because the study was the first one to use ^{18}F -FLT in the CR UK Beatson Institute, it was necessary to establish imaging protocol that would maximise signal-to-noise ratio. One of the ways to do it would be to temporarily inhibit the indigenous thymidine in the mouse, so it doesn't compete with the molecular probe administered. This was tried using thymidine phosphorylase used clinically to treat patients with solid tumours, but despite due care and slow infusion of the drug all three mice died shortly after its administration. The reason for it lies most likely in the formulation of the drug that was in a buffer solution containing potassium. Although no information could be obtained as to the actual potassium content it is very possible that it was sufficiently high to dysregulate mouse's cardiac rhythm that led to its demise. This approach was understandably abandoned.

Due to lack of information in the literature about uptake times and pharmacokinetics of ^{18}F -FLT in pancreatic cancer mouse models beyond 60 min, it was decided that this should be investigated. The hypothesis was that longer uptake time would allow for the probe to accumulate in the target (i.e. tumour)

while allowing for its clearance from other organs and therefore improving the signal-to-noise ratio. Dynamic scan of the mouse from the time of the i.v. injection with ^{18}F -FLT was conducted over the period of 3h after which CT scan was acquired. The reason for the scan duration was that Home Office guidelines limit the time mouse can be under continuous anaesthesia for up to 4h. Given the animals were showing clinical signs of advanced PDAC it was unlikely they would survive longer scan anyway. Indeed, two mice died during later scans that were shortened to 60 min static acquisition (after 2h uptake time). In the first dynamic PET scan conducted, however, mouse successfully recovered from anaesthesia after the imaging protocol concluded. In the future studies, it would be useful if mouse's vital signs (e.g. respiration) could be monitored. The tri-modal Albira PET/SPECT/CT at the time when the study was conducted did not offer such option. The only way to monitor an animal was a camera inside the scanner, close to the X-ray gantry, which, however, made it difficult to check the state of the animal if it was placed properly on the imaging bed, which was then closed with a semi-transparent lid. Also, when mouse was being scanned using PET, the distance between the imaging subject and the camera was too long to check the state of the mouse. For example, if the mouse was showing any signs of waking up from the anaesthesia or gasping this was considered a signal that the level of anaesthesia is too high. This problem was addressed by the manufacturer after the mTOR inhibitor study has concluded. The solution offered consisted of the integration of Albira with a third-party modular animal monitoring system, which became available as an extra option.

The time frames in this dynamic study were set to 1 min due to the unknown pharmacokinetics of the tracer in these mouse models. The focus was on finding the time-point, when the tumour uptake was at its maximum and the tracer is cleared from other tissues. The duration of the individual frames had several consequences. To start with the study ended with 180 individual list-mode files, which needed then to be reconstructed. This was very time-consuming. On the other hand, it did allow for the detailed analysis of the tracer biodistribution over relatively long period of time.

Short time frames mean that there was more noise in the reconstructed images due to relatively low number of coincidences registered. Furthermore, images

were reconstructed using Albira Reconstructor software and the default MLEM algorithm. This reconstruction method approximates tracer distribution over the selected number of iterations. It uses corrections like random and scattered events correction or normalization factor, which corrects for the uneven sensitivity within the scanner's FOV. As it was shown in the spatial resolution part of the NEMA protocol discussed in detail in Part I of this work, the best spatial resolution of 2-ring Albira PET can be obtained in the middle of one of its rings. The further away from that position, the poorer the spatial resolution is going to be. This fact was generally considered during all imaging studies conducted using Albira PET. However, the main objective of this exercise was to obtain biodistribution information, which requires that, if possible, whole body of the mouse fits within the FOV. This resulted in the tumour being in sub-optimal position within the FOV. Since there was a significant signal from the probe accumulated in the proliferating intestine, it would be impossible either way to draw a VOI reflecting exactly the shape of the tumour. PDAC tumours are known to be heterogeneous, which is reflected in the uneven tracer uptake.

Looking at the biodistribution of ^{18}F -FLT in the PDAC and the liver over the period of the pilot scan a trend can be observed with the signal coming from the tumour raising and the one from liver slowly. It is possible that scanning the animal for even longer period would lead to an improved image contrast. Of course, the image would be sharper if the initial activity of the injected radiopharmaceutical was higher, so the input from scattered events is relatively low. Yet, at the time of the imaging the dose could not be higher than 6 MBq (see section 4.1.3 Count-rate Performance in Part I), as otherwise the detectors would saturate. The pilot study using dynamic protocol used activity that was well within the linear range of the detectors' count-rate response. Based on the results of the pilot study future mice were imaged using static acquisition over a period of an hour. Imaging commenced 2h after tracer injection and its dose compensated for the ^{18}F decay over this time, so at the time of imaging still about 3 MBq of ^{18}F remained in the mouse (minus any excretion in the urine).

The aim of the study was to investigate a treatment response in two mouse models of PDAC. This involved scanning an animal before and after treatment. It was impossible to position the mouse on the imaging bed the same twice.

Therefore, during an image analysis the tumour wasn't in the same place and could only be identified relatively to the surrounding tissues, which can naturally lead to inaccuracies. Furthermore, in both cases the tumour was being outlined manually, which is somewhat arbitrary and needed to be validated. Agata Mrowinska and Douglas Morran independently conducted their analysis with good concordance. Results presented here are those of Douglas Morran. (Morran *et al.*, 2014)

Because CT showed poor contrast of the soft tissues its role in the identification of the tumour was limited. This could be improved using contrast agents, in particular those targeting liver and gastrointestinal tract. The use of the former was tried by Agata Mrowinska using Fenestra Liver Contrast (MediLumine, Montreal, Canada formerly known as Advanced Research Technologies; results not shown) (Cy *et al.*, 2013), but this was not done for the mice used in the ^{18}F -FLT study. The latter could be addressed by feeding the mice with barium sulphate (e.g. mixing it with peanut butter or drinking water). (Ay & Zaidi, 2006; Clark *et al.*, 2015; Wathen *et al.*, 2013) This was not tried. All contrast agents need to be carefully titrated to find an appropriate dose (although this is often suggested by the manufacturer). Their clearance also needs to be known. Fenestra can enhance the liver contrast over 1 day (Suckow & Stout, 2008), but care has to be taken in dosing an animal as an allergic reaction to iodine may occur. (MediLumine, 2016) Important to note is that any use of CT contrast agent with PET should be validated due to the potential of increasing the scattering of positrons and hence deteriorate the quality of the PET image. This can, however, be partially overcome by using X-ray based attenuation map and using it as correction in PET. (Ay & Zaidi, 2006) Unfortunately, the available Albira PET did not offer such option although the newer generations of this scanner and in particular the 3-ring version of PET provide it.

Normal pancreas shows a background level of signal in a PET image. This is not the case for cancerous lesions. The literature presents conflicting reports regarding the usefulness of ^{18}F -FLT in diagnosing or observing a treatment response in human pancreatic cancer due to its lower sensitivity than ^{18}F -FDG, which is used as standard. (Challapalli *et al.*, 2015; Debebe *et al.*, 2016; Herrmann *et al.*, 2012; Mamon *et al.*, 2009; Quon *et al.*, 2008) Herrmann and

colleagues point out that proliferation is not the exclusive feature of pancreatic malignancies and can be found also in benign inflammatory lesions of the pancreas. This may lead to false-positives. Overall it is more specific radiotracer than ^{18}F -FDG and may complement the former in diagnostic and therapeutic investigations.

This study showed that PET imaging with ^{18}F -FLT is a useful tool in comparing the proliferation response to mTOR inhibitor rapamycin in KC Pten and KPC mice. Specifically, it showed proliferation arrest in the former, but not in the latter. This is an evidence that Pten deletion makes tumour rely on the mTOR pathway. It is an important finding that can lead to better therapy for a subset of patients (ca. 10%) with tumours driven by KRAS mutation and Pten deletion.

10.2 Gamma Counter Experiments

In the preparatory experiment the calibration curve of the gamma counter was measured. Its results bear significance over the samples that can be then measured during animal experiments, i.e. how high and high low activities can be measured and is there a linear relationship between the activity of the samples and counts registered. The experiment showed that such relationship exists ($R^2 = 0.99$ for the energy windows 15 to 2000 keV and 311 to 711 keV, and $R^2 = 0.92$ for 822 to 1222 keV). Furthermore, it was important to determine that samples with the activities above ca. 300 kBq cannot be resolved by the counter as the detectors saturate and the device freezes. This has direct bearing upon the dose an animal can be injected with, i.e. if at the time of dissection and subsequent measurement any organ contains too high activity, this will not be able to be measured, at least not until ^{18}F decays below this threshold.

The experiment showed also another few issues that had to be considered in the later experiments. One of them was that the samples cannot be placed on the rack too close to each other as this may cause an interference in the measurements. As the rule of thumb, it was established by the previous users that 2-3 empty spaces in the cassette are sufficient to avert this. Another important consideration is the outdated technology. Although the detector electronics may be reliable and of high resolution, it is connected to a PC using DOS operating system. This computer displays results on the screen, but only the

last 10 of them. They are also printed using a dot-matrix printer, which uses special perforated paper. Any problems with the paper feed may result in the printing error and lead to a potential risk of losing data. The quality of the print also left a lot to be desired for and required some experience in reading the numbers off the page. There is no modern communication device that would allow for an export of the file containing the results - only a 5 ¼ inch floppy disk station. The only way to deal with those challenges was to stay at the gamma counter until at least the first sample is counted and the results are sent to a printer (meaning also that the sample activity is within the linear range) - if the paper feed is even and the print-out readable, other samples can be left unattended. When processing the data later using spreadsheet, the accuracy of the entered numbers could be verified calculating the ratio of the counts measured in the 15 to 2000 keV to 311 to 711 keV - depending on the sample volume (discussed below) the ratio should be around 1.7.

There is no way to predict how much activity will be retained in the tissue after a certain uptake time, using a certain radiotracer and an animal model. This needs to be verified during pilot experiments or estimated analysing PET images, if available. If there are prior PET images, gamma counting *ex vivo* can serve as a tool to validate the PET data and estimate partial volume effect PET images may suffer from. In the absence of PET images, such data can still provide valuable information about the biodistribution of the probe at a given time-point. It would be unwise, however, to assume that gamma counting results would be immune to sample size or the activity an organ (or piece of it) contains. As discussed above, the latter, in case of ^{18}F and the counter used in the experiment, is about 300 kBq. On the other hand, the experiment looking at the impact of the size volume showed that the relationship between counts registered in the widest and the middle energy window (15 to 2000 kBq and 311 to 711 kBq) follows an exponential decay curve.

One could expect that the larger the volume of the sample, the more scattered the gamma photons become and the more likely they lose their energy and fall outside the bottom threshold of the 311 to 711 keV energy window (the annihilation photons energy peak being 511 keV). In that case the number of photons in the 15 to 2000 keV energy window would increase and in 311 to 711

keV would decrease. Their ratio therefore would increase with the increasing volume. Yet the effect observed is quite the opposite. The decay-corrected and averaged results in the latter energy window aggregate around line of negligible slope, so within 100 to 1500 μl are nearly constant. However, the counts in the 15 to 2000 keV energy window decrease as the volume of the sample increases. If the number of the photons in the former energy window is unchanged then the loss in the total measured photons can be explained by the absorption of the low energy photons (below 311 keV) by the sample. Per the plot of count ratio with respect to sample volume, the number of the low energy photons increases exponentially as the sample size increases. It is worth noting, however, that this effect does not depend on the sample activity, since the annihilation photons peak energy is also independent of this activity.

It was calculated that the difference between the maximum and the minimum measurement in the 311 to 711 keV energy window within the range of activities measured was less than 5%. This energy window therefore yields the least variable results and it is the reason why it was chosen as the reference window in the ^{18}F -FLT biodistribution experiments.

10.3 TGFB

The aim of the study was to investigate if the addition of TGFB antibody to gemcitabine, which is for now still considered a “golden standard” in the treatment of pancreatic cancer, improves the efficacy of such treatment. The surrogate outcome in which it was assessed was proliferation, which is one of the processes controlled by the PI3K pathway in which TGFB plays an important role. Proliferation was measured in three different ways. Animals were injected with ^{18}F -FLT and the biodistribution of the probe in all main organs harvested 2h after injection was measured using gamma counting. Next, parts of the frozen pancreatic and liver tissues were cut and exposed overnight to photographic film in autoradiography study. Finally, the remaining parts of those tissues were fixed in buffered formalin, paraffin embedded, cut and Ki67 IHC performed.

There is not enough evidence that would indicated that statistically significant difference between the biodistribution of ^{18}F -FLT as measured by gamma counting among the treated and untreated cohorts of mice exists or does not

exist. An organ that showed the smallest retention of the probe was brain and the highest was measured for large and small intestine. This is consistent with the expected level of proliferation in those organs, also in a healthy animal. The level of signal measured for the tumour was like the one of spleen, stomach, liver or blood and varied little between groups treated with gemcitabine or with added TGF β antibodies. This did not differ from the untreated group, which is unexpected since gemcitabine interferes with DNA synthesis (and hence proliferation) and induces apoptosis. One of the explanations could be that benefits of gemcitabine treatment can be observed in the longer time-scale and after treatment that involves constant, but small dosing of the drug, and not acutely, 24h after intraperitoneal injection.

The lack of obvious difference among the experimental groups can also possibly be attributed to mice being at different stages of the disease development. Although all due care was taken to select only animals with palpable tumours, at necropsy the disease advancement proved to vary vastly - some mice had obvious, large tumours with fibrous stroma, but some seemed to have no tumour at all and only proved to be at early stages of carcinoma when IHC was performed. Also, some animals were showing co-morbid conditions like blocked bile-duct, lymphoma or additional lung cancer. It might be that the actual effect of the investigated therapy will only emerge once the cohorts are further enlarged, so such animals can be excluded from the analysis or when there is sufficient number of those with such conditions that they can be analysed as separate sub-groups.

Alternatively, since TGF β is known to play two different roles in the cancer development, the effect would be prominent if mice could be divided for the cancer stage. However, this would be very difficult to achieve using KPC mouse model as it is challenging to select animals at the early stage of the disease and additionally, animals in late stages have very limited life-expectation and may need to be euthanized prematurely for ethical reasons. Some animals had also distant metastasis, which further changes the picture of the summary. The level of the disease development is probably the largest contributing factor in the variability in the experiment, mainly because the role of TGF β changes as the cancer advances. It could be that by introducing TGF β antibody in the early

stages the pace of cancer progression was increased as the cancer-suppressive properties of TGF β were inhibited. On the other hand, in late stages of the disease the variety of co-morbid conditions may impact in how the TGF β antibody is distributed in the body. It might be that it shows affinity to receptors in other sites than pancreatic tumours.

The dose of the antibody could also be inadequate in late stages of the disease. The dose used in the experiment was the same as one used in the (unpublished) pilot study performed in the CR UK Beatson Institute. It could be that titration of the drug is needed to establish the minimal working dose. However, the aim of the study was not to find the dose that would impact mouse survival, but rather to establish if introducing TGF β antibody has any impact on proliferation whatsoever.

During the experiment a problem arose with the availability of the TGF β antibody that was being used. After discussion with the manufacturer, an alternative was selected and the study was continued using the new antibody. Although very little difference was observed between mice treated with either antibody it would certainly improve the statistical power of the study if the same antibody could be used throughout the whole study.

It could also be that no effect was observed, because the antibody does not reach the site of interest. The antibody was optimised to be used in other applications like Western Blotting and/or IHC, but not necessarily in the *in vivo* study. It could be that it is broken down or otherwise metabolized before it has a chance to bind to the receptors in the cancer site when introduced via an intraperitoneal injection. The way to answer that would be to perform IHC using the antibody to see if there is any difference in IHC expression among treated and un-treated cohorts. However, even if the antibody binds to the receptor, TGF β activity should be confirmed. This could be done by investigating the activity of the downstream proteins in the SMAD pathway (e.g. SMAD2, SMAD3) and in the PI3K/AKT pathway (e.g. Src, S6 kinase).

The study looked at the acute effect of antibody on proliferation, i.e. at 24 \pm 2h post-injection. It is likely that any longer than that and the antibody is completely cleaved from the receptor and the latter returns to the base-line

state. It could be, however, that at shorter time-point the observed effects is greater and that to bring benefit, mouse would need to be treated at shorter time intervals, which is problematic when it comes to animal welfare (even if the stress induced by frequent treatment is considered) and cost-effectiveness antibody-treatment being much costlier than chemotherapy.

It would be beneficial if all mice in the study were investigated using the same techniques. This was not, however, possible for independent reasons, e.g. after selected mice were treated the day before, ^{18}F -FLT synthesis was not always possible due to equipment failure. Also, some mice had to be euthanized before they could be used in the study and the necropsy showed that their poor condition was caused by the cancer-related condition like lymphoma or blocked bile duct.

It proved challenging to inject animals with enough ^{18}F -FLT, so after 2h (plus the time needed for the dissection) the level of signal from each sampled organ would be high enough (but too high) to perform gamma counting and autoradiography. Care had to be taken here not to inject animal with volume larger than 200 μl and ensuring that all animals studied on the day were injected with the same activity. The last of three mice was always injected with the highest volume due to the radiotracer decay and using this volume as a guideline, the maximum dose for other two mice was calculated.

Although the study design entailed sacrificing mice after treatment such approach requires use of much larger cohort of mice to achieve the same statistical power than if each mouse was its own control. This could only be achieved if some sort of functional imaging technique *in vivo* could be used. As such, PET imaging using proliferation marker like ^{18}F -FLT would be particularly helpful. Unfortunately, at the time the study was conducted, Bruker Albira PET/SPECT/CT scanner was decommissioned and could not be used and this is part of the reason why alternative techniques were used. The other reason for the use of gamma counting and autoradiography was that they can be used as *ex vivo* validation techniques of PET since all three are based on the use of radio-labelled probe. Ki67 IHC was used because it is an alternative way of measuring proliferation and, at least in theory, should provide the same answer to the aforementioned.

Out of the three ways of measuring proliferation, autoradiography proved to be the least-informative. The contrast between the background and the tissue was low and images of the sections proved to be of low resolution that would not reflect tumour heterogeneity. Perhaps if the mouse was injected with higher activity this could be partially alleviated, but using sensitive photographic film risks bleaching in the over-exposed regions. This was observed when one of the mice was accidentally injected with ^{18}F -FLT subcutaneously in the tail and, as a result, the dose must have been being absorbed over longer period of time than if it would otherwise be the case (data not shown).

Ideally also it would be useful if autoradiography slices could be compared 1:1 with Ki67-stained ones. This could be achieved by cutting pairs of adjacent frozen sections and then using one of them for autoradiography and another one for frozen Ki67 staining. This was attempted at the first experiments, where the latter stage was performed using automatic protocol on Dako Autostainer. Unfortunately, the IHC on frozen sections proved unsuccessful (the tissue sections were peeling off the slide) and this direction was eventually abandoned in favour of the formalin-fixed and paraffin-embedded sections from the other half of the tissue sample. This provided valuable high-resolution insight into the tissue morphology in cases, where gross pathology could not point to an obvious solid tumour. Yet, since PDAC tumours are known from their heterogeneity it could be that autoradiography and IHC samples were inadvertently taken from sites unequally affected by the disease. In that respect IHC and gamma counting samples could theoretically be compared more closely, because those measurements were taken using the same pieces of tissue. However, Ki67 staining was performed on a single section, 4 μm -thick, which may not represent well the rest of the sample. If one were to compare the correlation between Ki67-staining and gamma-counting results, whole piece of tissue should be sliced and stained. Although time-consuming, this is possible, albeit does not guarantee better accuracy of the results or definitive answer to the question posed.

Certainly, what would improve the statistical power of the results is if all mice in the study could be evaluated using all three techniques. Unfortunately, despite the best efforts some data was lost due to equipment failures (e.g.

failure of the GE FastLab to produce ^{18}F -FLT, error in the X-ray film processor). The biggest challenge remained, however, in the time needed to process one mouse from the moment of the tail-vein injection to the time of submission of the samples to the Histology Department for fixing, embedding in paraffin, cutting and staining for Ki67. Even when the injection of the mice was staggered, this would only allow for processing of maximum of three mice on any given day. Partially this constraint stems from the limited volume the mouse can be injected with. Mainly, however, it was a result of the actual time needed to harvest all the samples, freeze them, transport them out of the animal facility and to the laboratory holding the gamma counter. Further, time was needed to cut the frozen tissues and apply the X-ray film in the dark room placed in the far-end part of the building.

Biodistribution data show that no trends could be discerned among the accumulation of ^{18}F -FLT or its metabolites in the sampled organs, but provides insight into the behaviour of the used probe that can be useful when planning another study using the same mouse model and/or PET imaging study. If the latter was available, a comparison could be made between apparent activity concentration and one that was measured using gamma counter. In general, gamma counter is more sensitive, while in PET part of the signal is lost due to the scanner geometry and detector technology, which at the moment can, at best, register 9-10% of all annihilation events. Additionally, PET suffers from partial volume effect, which may lead to over- or underestimation of the actual activity concentration in the given organ. This may be significant if one were to compare pre- and post-treatment images of a subject. The only way to avoid it would be to excise the organ and measure it using an independent technique (e.g. gamma counter). However, the advantage of PET over *ex vivo* measurements is that it allows for longitudinal studies and monitoring the progression of the disease, where subject is its own control over the period.

The normalized results for each organ (which considered the administered dose of ^{18}F -FLT, weight of the mouse and time that elapsed between administration of ^{18}F -FLT and measurement) were analysed using lima package in R-software. These did not correlate with the treatment a mouse was subject to in a significant manner in any of the sampled tissues. For the sake of saving time if

the experiment was to be repeated or continued, only PDAC and liver tissues could be harvested and tested. This would most likely allow for processing of more than 3 mice per experiment. However, KPC mice are not easily available and develop cancer spontaneously from the age of 10-weeks onwards. This complicates the logistics-side of the matter, because at the time experiment is due, there can be problems in finding suitable number of animals that would show clinical signs of locally advanced disease. It can only be achieved if one were to keep large cohort of animals of different ages, which is costly and does not guarantee success. Also, because the pancreata of mice have mesenteric and not a solid structure (like in humans), which wraps around intestine, it is possible and relatively easy (especially for an unexperienced person) to misdiagnose an animal. Namely, during the palpation of the mouse's abdomen one may assume the existence of a tumour, where in fact it is the bowel movement. The way to avoid it would be to seek opinion from more experienced persons, use another technique to visualise the contents of the abdominal cavity (like ultrasound) or try to palpate the tumour the next day (bowel movement will most likely be gone by then while tumour will rather stay in the same place). In some cases, where mouse is expressing also fluorescent or bioluminescent proteins in the cancer cells (a derivative model from KPC) fluorescence or bioluminescence imaging techniques may also provide a way to pre-screen animals for the experiment. Their downside is that they are not very useful when the tissue of interest is deeper than few millimetres in the body and that the measured signal is proportional to the number of cancer cells. This has obvious limited application when looking for animals at the early stages of the disease. Of course, at later stages, the clinical signs are quite easily noticeable, but what causes problems then are the co-morbid conditions, which can be equally fatal to the mouse if left unattended (e.g. lymphoma, blocked bile duct etc.). This is the reason why some mice needed to be euthanized before they could be enrolled in the study and why data from the remaining ones is loaded with extra noise as some conditions were only diagnosed post-mortem.

The aim of the study was to compare the cohorts of mice treated with gemcitabine and TGFB antibody, and gemcitabine only. The results do not show clear advantage of the former upon monotherapy. Interestingly, compared to the untreated cohort, gemcitabine does not show to make significant difference

in the proliferation levels in any of the assessed organs nor using any of the measurement techniques applied.

The source of additional experimental noise could also be from the genetic background of the mice used. Specifically, most of the mice were of “pure” KPC phenotype, but additionally expressed green fluorescent protein (GFP) and ecadherin genes in the Pdx-1 progenitor cells. The latter were used in the experiment since they show the same clinical signs and at the same timescale as “normal” KPC mice. There is a possibility, however, that the extra proteins produced by the cancer cells interfere somehow with the drugs and/or ^{18}F -FLT administered. This could be investigated further if larger cohorts of mice of both genotypes were available. At the basic level of data analysis (data not shown), there was no apparent difference between the groups, hence they were pooled into one group to represent KPC mice.

The fact that no significant difference was observed in the series of experiments described above could be simply since the effect was too small to be observed due to the noise level. Alternatively, the time at which the proliferation was measured could be sub-optimal. The 2h uptake time was based on the results of the mTOR PET imaging experiment discussed above. Yet, in this experiment KC Pten mouse was imaged and the whole uptake period was taking place under anaesthesia. The 2h post- ^{18}F -FLT administration time was chosen, because KC Pten and KPC resemble each other in clinical signs and how the disease progresses. The anaesthesia would slow down the metabolism of the mouse, but should not have much impact upon proliferation.

The conclusion is that within the given time-scale and using the applied techniques no proliferation-inhibitory advantage of adding TGF β antibodies to gemcitabine was observed. This does not mean that this treatment approach would not improve survival rates or otherwise limit the metastatic spread. The available results assess the effects of a single treatment 24 ± 2 h after. This was deemed as “acute” response to treatment, while in fact there is no data investigating proliferation rates at different time-points or measuring the effects of TGF β antibodies administration over a time alone or in conjunction with gemcitabine. It could be that the TGF β antibody does aid the proliferation inhibition, but only over much shorter time after which its rate returns to the

baseline. Alternatively, there could be a benefit in using TGF β antibodies (preferably as a course of treatment) not only to inhibit proliferation, but to help with desmoplasia. If the latter was achieved, this could help in the drug delivery into the tumour. There could also be more effective TGF β inhibitors (other than antibodies) that could yield better results.

TGF β remains an attractive, yet somewhat elusive therapeutic target. Due to its complex interactions with other proteins and involvement in the variety of pathways activated in cancer, it will take time before we understand its role fully. The series of experiments presented aimed at only one of its facets, namely proliferation. We investigated the effect of TGF β inhibition in the *in vivo* environment and this work can now provide a good background data that can help in future imaging studies using ^{18}F -FLT in the pancreatic cancer mouse models.

11 Conclusions

As a molecular imaging technique PET became an important tool aiding the diagnosis and assessment of the treatment efficacy in cancer and other illnesses. With the improvements in the detector technologies and image reconstruction small-animal PET can currently produce images of a sub-millimetre spatial resolution and sensitivity approaching 10%. This makes it invaluable tool in pre-clinical *in vivo* research of novel radiopharmaceuticals, drug development and improving our understanding of mechanisms driving various diseases. In this work, I characterised the performance of PET and CT components of Albira PET/SPECT/CT - a tri-modal small-animal scanner, which proved it to be sufficient for mice imaging.

I then considered the use of ^{18}F -FLT as a proliferation marker allowing for the characterisation of the treatment response in two mouse models of PDAC. In the first study, we have shown that rapamycin, an mTOR inhibitor brings therapeutic benefits like proliferative arrest (measured using ^{18}F -FLT PET and Ki67 IHC) and improved survival in KC Pten, but not KPC mice. In the TGF β antibody study untreated, gemcitabine-treated, and gemcitabine and TGF β antibody-treated mice were compared using gamma counting, autoradiography and Ki67 IHC. None of those techniques showed significant difference to proliferation.

12 Appendix

Mouse record sheet

Date: _____ Mouse ID: _____ Strain: _____

Previous PPL: _____ Mouse sex: _____ Weight [g]: _____

Doses

Prepared: _____ MBq At (time) _____ In (volume) _____ μ l

Left: _____ MBq At (time) _____

Injected _____ MBq At (time) _____ Animal sacr.: _____

Gamma counting:

Counting started: _____

Protocol number: 7

Vial ID	Tissue	W. before [g]	W. after [g]	Tissue [g]	Counts /1min
	Blood				
	Heart				
	Lungs				
	Spleen				
	Kidney				
	Stomach				
	SG				
	LG				
	PDAC/pancreas				
	Liver				
	Muscle				
	Brain				
	Ctrl1				
	Ctrl2				
	Ctrl 3				

Autoradiography:

Cutting started: _____

Film applied: _____

13 References

Hounsfield Units - Scale of HU, CT Numbers.

<http://radclass.mudr.org/content/hounsfield-units-scale-hu-ct-numbers>

(accessed 20/10/2015)

Adami HO, McLaughlin J, Ekblom A *et al.* (1991) Cancer Risk in Patients with Diabetes-Mellitus. *Cancer Causes Control* **2**, 307-314.

Aide N, Visser EP, Lheureux S *et al.* (2012) The motivations and methodology for high-throughput PET imaging of small animals in cancer research. *European Journal of Nuclear Medicine and Molecular Imaging* **39**, 1497-1509.

Akhurst RJ, Derynck R (2001) TGF-beta signaling in cancer - a double-edged sword. *Trends Cell Biol* **11**, S44-S51.

Alvarellos ML, Lamba J, Sangkuhl K *et al.* (2014) PharmGKB summary: gemcitabine pathway. *Pharmacogenet Genomics* **24**, 564-574.

American Cancer Society (2016a) Ablation or embolization treatments for pancreatic cancer.

<http://www.cancer.org/cancer/pancreaticcancer/detailedguide/pancreatic-cancer-treating-ablative-techniques>

(accessed 05-06-2016)

American Cancer Society (2016b) Pain control in pancreatic cancer.

<http://www.cancer.org/cancer/pancreaticcancer/detailedguide/pancreatic-cancer-treating-pain-control>

(accessed 05-06-2016)

AndrenSandberg A, Dervenis C, Lowenfels B (1997) Etiologic links between chronic pancreatitis and pancreatic cancer. *Scand J Gastroenterol* **32**, 97-103.

Apte MV, Park S, Phillips PA *et al.* (2004) Desmoplastic reaction in pancreatic cancer: Role of pancreatic stellate cells. *Pancreas* **29**, 179-187.

Ay MR, Zaidi H (2006) Assessment of errors caused by X-ray scatter and use of contrast medium when using CT-based attenuation correction in PET. *Eur J Nucl Med Mol Imaging* **33**, 1301-1313.

- Azizi A, Naguib NN, Mbalisike E *et al.* (2011) Liver metastases of pancreatic cancer: role of repetitive transarterial chemoembolization (TACE) on tumor response and survival. *Pancreas* **40**, 1271-1275.
- Bai X-L, Zhang Q, Masood W *et al.* (2012) Sister Mary Joseph's nodule as a first sign of pancreatic cancer. *World Journal of Gastroenterology : WJG* **18**, 6686-6689.
- Bailey P, Chang DK, Nones K *et al.* (2016) Genomic analyses identify molecular subtypes of pancreatic cancer. *Nature* **531**, 47-52.
- Balcerzyk M, Kontaxakis G, Delgado M *et al.* (2009) Initial performance evaluation of a high resolution Albira small animal positron emission tomography scanner with monolithic crystals and depth-of-interaction encoding from a user's perspective. *Measurement Science & Technology* **20**.
- Bao Q, Newport D, Chen M *et al.* (2009) Performance Evaluation of the Inveon Dedicated PET Preclinical Tomograph Based on the NEMA NU-4 Standards. *Journal of Nuclear Medicine* **50**, 401-408.
- Boffetta P, Aagnes B, Weiderpass E *et al.* (2005) Smokeless tobacco use and risk of cancer of the pancreas and other organs. *Int J Cancer* **114**, 992-995.
- Bond-Smith G, Banga N, Hammond TM *et al.* (2012) Pancreatic adenocarcinoma. *Br Med J* **344**, 10.
- Boone JM, Velazquez O, Cherry SR (2004) Small-animal X-ray dose from micro-CT. *Molecular imaging* **3**, 149-158.
- Boyd SK, Davison P, Muller R *et al.* (2006) Monitoring individual morphological changes over time in ovariectomized rats by in vivo micro-computed tomography. *Bone* **39**, 854-862.
- Brant WE, Helms CA (2007) *Fundamentals of Diagnostic Radiology*. 3rd ed. Philadelphia, PA, USA: Lippincott Williams & Wilkins.
- Bruker BioSpin (2012) *Albira Imaging. Bruker Albira Imaging System - User Manual*. vol. IB5438511 Rev. C 12/12. www.bruker.com.

Bruker BioSpin (2014) Albira. Revolutionary Preclinical PET/SPECT/CT Imaging System.

Buijs JT, Stayrook KR, Guise TA (2012) The role of TGF-[beta] in bone metastasis: novel therapeutic perspectives. *BoneKEy Rep* 1.

Campbell F, Verbeke CS (2013) *Pathology of the Pancreas: A Practical Approach*: Springer London.

Cancer Research UK (2015a) Pancreatic cancer statistics for UK. <http://www.cancerresearchuk.org/health-professional/cancer-statistics/statistics-by-cancer-type/pancreatic-cancer>

Cancer Research UK (2015b) A trial looking at a vaccine called GV1001 for pancreatic cancer that has spread (TeloVac). <http://www.cancerresearchuk.org/about-cancer/find-a-clinical-trial/a-trial-looking-at-a-vaccine-called-gv1001-for-pancreatic-cancer-that-has-spread> (accessed 08-07-2016)

Carr-Locke DL, Davies TJ (1980) Pancreatic juice gamma-glutamyltransferase, alanine transaminase, and alkaline phosphatase in pancreatic disease. *Digestive diseases and sciences* 25, 374-378.

Chalhoub N, Baker SJ (2009) PTEN and the PI3-Kinase Pathway in Cancer. In *Annual Review of Pathology-Mechanisms of Disease*, vol. 4, pp. 127-150. Palo Alto: Annual Reviews.

Challapalli A, Barwick T, Pearson RA *et al.* (2015) 3'-Deoxy-3'-F-18-fluorothymidine positron emission tomography as an early predictor of disease progression in patients with advanced and metastatic pancreatic cancer. *European Journal of Nuclear Medicine and Molecular Imaging* 42, 831-840.

Challapalli A, Wasan HS, Al-Nahhas A *et al.* (2012) F-18-fluorothymidine (FLT) PET-CT for early response assessment in advanced pancreatic cancer. *J Clin Oncol* 30, 1.

- Chen NH, Brachmann C, Liu XP *et al.* (2015) Albumin-bound nanoparticle (nab) paclitaxel exhibits enhanced paclitaxel tissue distribution and tumor penetration. *Cancer Chemother Pharmacol* **76**, 699-712.
- Clark DP, Touch M, Barber W *et al.* (2015) Simultaneous imaging of multiple contrast agents using full-spectrum micro-CT. In *Medical Imaging 2015: Physics of Medical Imaging*, vol. 9412 [C Hoeschen and D Kontos, editors]. Bellingham: Spie-Int Soc Optical Engineering.
- Cy A, Bour G, Raykov Z *et al.* (2013) Structural imaging of the pancreas in rat using micro-CT: application to a non-invasive longitudinal evaluation of pancreatic ductal carcinoma monitoring. *Journal of Cancer Research & Therapy* **1**, 70-76.
- de Gonzalez AB, Spencer EA, Bueno-de-Mesquita HB *et al.* (2006) Anthropometry, physical activity, and the risk of pancreatic cancer in the European Prospective Investigation into Cancer and Nutrition. *Cancer Epidemiol Biomarkers Prev* **15**, 879-885.
- de Gonzalez AB, Sweetland S, Spencer E (2003) A meta-analysis of obesity and the risk of pancreatic cancer. *Br J Cancer* **89**, 519-523.
- Debebe SA, Goryawala M, Adjouadi M *et al.* (2016) F-18-FLT Positron Emission Tomography/Computed Tomography Imaging in Pancreatic Cancer: Determination of Tumor Proliferative Activity and Comparison with Glycolytic Activity as Measured by F-18-FDG Positron Emission Tomography/Computed Tomography Imaging. *Mol Imaging Radionucl Ther* **25**, 32-38.
- Dintzis SM, Liggitt D (2012) Pancreas. In *Comparative Anatomy and Histology*, pp. 203-209. San Diego: Academic Press.
- Dolenšek J, Rupnik MS, Stožer A (2015) Structural similarities and differences between the human and the mouse pancreas. *Islets* **7**, e1024405.
- Ehrsson H, Wallin I, Yachnin J (2002) Pharmacokinetics of oxaliplatin in humans. *Medical oncology (Northwood, London, England)* **19**, 261-265.

- Ekblom A, Trichopoulos D (2008) Pancreatic Cancer. In *Textbook of Cancer Epidemiology*, pp. 334-348 [H-O Adami, D Hunter and D Trichopoulos, editors]. Oxford Scholarship Online: Oxford University Press.
- Elhami E, Boulding J, Goertzen AL *et al.* (2011) Variations on the NEMA NU4-2008 Testing Procedures and Effect on the Performance Measurement Results. *2011 IEEE Nuclear Science Symposium and Medical Imaging Conference (Nss/Mic)*, 3244-3246.
- Fernandez E, Lavecchia C, Davanzo B *et al.* (1994) Family History and the Risk of Liver, Gallbladder, and Pancreatic-Cancer. *Cancer Epidemiol Biomarkers Prev* 3, 209-212.
- Funk T, Sun MS, Hasegawa BH (2004) Radiation dose estimate in small animal SPECT and PET. *Med Phys* 31, 2680-2686.
- Garrido-Laguna I, Hidalgo M (2015) Pancreatic cancer: from state-of-the-art treatments to promising novel therapies. *Nat Rev Clin Oncol* 12, 319-334.
- Gaspar NJ, Li LY, Kapoun AM *et al.* (2007) Inhibition of transforming growth factor beta signaling reduces pancreatic adenocarcinoma growth and invasiveness. *Mol Pharmacol* 72, 152-161.
- Ghadirian P, Boyle P, Simard A *et al.* (1991) Reported Family Aggregation of Pancreatic-Cancer within a Population-Based Case-Control Study in the Francophone-Community in Montreal, Canada. *Int J Pancreatol* 10, 183-196.
- Goertzen AL, Bao Q, Bergeron M *et al.* (2012) NEMA NU 4-2008 Comparison of Preclinical PET Imaging Systems. *Journal of Nuclear Medicine* 53, 1300-1309.
- Gonzalez A, Correcher C, Molinos C *et al.* (2015) Next Generation of the Albira Small Animal PET Based on SiPM Detectors and Continuous Crystals. (application note).
- Goorden MC, van der Have F, Kreuger R *et al.* (2013) VECTor: A Preclinical Imaging System for Simultaneous Submillimeter SPECT and PET. *Journal of Nuclear Medicine* 54, 306-312.

- Gu Z, Taschereau R, Vu NT *et al.* (2013) NEMA NU-4 performance evaluation of PETbox4, a high sensitivity dedicated PET preclinical tomograph. *Physics in Medicine and Biology* **58**, 3791.
- Gu Z, Taschereau R, Vu NT *et al.* (2011) Design and initial performance of PETbox4, a high sensitivity preclinical imaging tomograph. *Nuclear Science Symposium and Medical Imaging Conference (NSS/MIC), 2011 IEEE*, 2328-2331.
- Gunturu KS, Rossi GR, Saif MW (2013) Immunotherapy updates in pancreatic cancer: are we there yet? *Therapeutic Advances in Medical Oncology* **5**, 81-89.
- Herrmann K, Dahlbom M, Nathanson D *et al.* (2013) Evaluation of the Genisys4, a Bench-Top Preclinical PET Scanner. *Journal of Nuclear Medicine* **54**, 1162-1167.
- Herrmann K, Erkan M, Dobritz M *et al.* (2012) Comparison of 3'-deoxy-3'-F-18 fluorothymidine positron emission tomography (FLT PET) and FDG PET/CT for the detection and characterization of pancreatic tumours. *European Journal of Nuclear Medicine and Molecular Imaging* **39**, 846-851.
- Hill R, Calvopina JH, Kim C *et al.* (2010) PTEN Loss Accelerates Kras(G12D)-Induced Pancreatic Cancer Development. *Cancer Res* **70**, 7114-7124.
- Hingorani SR, Wang L, Multani AS *et al.* (2005) Trp53R172H and KrasG12D cooperate to promote chromosomal instability and widely metastatic pancreatic ductal adenocarcinoma in mice. *Cancer Cell* **7**, 469-483.
- Horwitz SB (1992) Mechanism of Action of Taxol. *Trends Pharmacol Sci* **13**, 134-136.
- Hruban RH, Adsay NV, Albores-Saavedra J *et al.* (2001) Pancreatic intraepithelial neoplasia: a new nomenclature and classification system for pancreatic duct lesions. *The American journal of surgical pathology* **25**, 579-586.
- Hruban RH, Kim B, Sandone C *et al.* (2015) The Johns Hopkins Atlas of Pancreas Pathology iPad App, 1.0 ed.: The Johns Hopkins University School of Medicine.
- Hruban RH, Maitra A, Goggins M (2008) Update on Pancreatic Intraepithelial Neoplasia. *International Journal of Clinical and Experimental Pathology* **1**, 306-316.

Ikushima H, Miyazono K (2010) TGF β signalling: a complex web in cancer progression. *Nat Rev Cancer* **10**, 415-424.

Information Services Division Scotland (2015). <http://www.isdscotland.org/> (accessed 12-12-2015)

Johnston PG, Kaye S (2001) Capecitabine: a novel agent for the treatment of solid tumors. *Anticancer Drugs* **12**, 639-646.

Kabashima A, Higuchi H, Takaishi H *et al.* (2009) Side population of pancreatic cancer cells predominates in TGF- β -mediated epithelial to mesenchymal transition and invasion. *Int J Cancer* **124**, 2771-2779.

Kachelriess M (2008) Micro-CT. In *Handbook of Experimental Pharmacology*, vol. 185, pp. 23-52 [W Semmler and M Schwaiger, editors]: Springer-Verlag Berlin, Heidelberger Platz 3, D-14197 Berlin, Germany.

Kalluri R, Weinberg RA (2009) The basics of epithelial-mesenchymal transition. *The Journal of Clinical Investigation* **119**, 1420-1428.

Kemp BJ, Hruska CB, McFarland AR *et al.* (2009) NEMA NU 2-2007 performance measurements of the Siemens Inveon (TM) preclinical small animal PET system. *Physics in Medicine and Biology* **54**, 2359-2376.

Kennedy Alyssa L, Morton Jennifer P, Manoharan I *et al.* (2011) Activation of the PIK3CA/AKT Pathway Suppresses Senescence Induced by an Activated RAS Oncogene to Promote Tumorigenesis. *Molecular Cell* **42**, 36-49.

Khan KH, Yap TA, Yan L *et al.* (2013) Targeting the PI3K-AKT-mTOR signaling network in cancer. *Chin J Cancer* **32**, 253-265.

Klein AP, Brune KA, Petersen GM *et al.* (2004) Prospective risk of pancreatic cancer in familial pancreatic cancer kindreds. *Cancer Res* **64**, 2634-2638.

Kuntner C, Stout DB (2014) Quantitative preclinical PET imaging: opportunities and challenges. *Frontiers in Physics* **2**.

Lamarca A, Asselin MC, Manoharan P *et al.* (2016) F-18-FLT PET imaging of cellular proliferation in pancreatic cancer. *Crit Rev Oncol/Hematol* **99**, 158-169.

Lamarca A, Manoharan P, Asselin MC *et al.* (2013) Pilot, proof-of-concept studies for determining the feasibility of the use of FLT-PET in patients with pancreatic adenocarcinoma. *J Clin Oncol* **31**, 1.

Lawrence MacDonald, J. Edwards, T. Lewellen, D. Haseley, J. Rogers, P. Kinahan (2009) Clinical Imaging Characteristics of the Positron Emission Mammography Camera: PEM Flex Solo II. *Journal of Nuclear Medicine* **50**, 1666-1675.

Loc WS, Smith JP, Matters G *et al.* (2014) Novel strategies for managing pancreatic cancer. *World J Gastroenterol* **20**, 14717-14725.

Loening AM, Gambhir SS (2003) AMIDE: a free software tool for multimodality medical image analysis. *Molecular imaging* **2**, 131-137.

Longley DB, Harkin DP, Johnston PG (2003) 5-fluorouracil: mechanisms of action and clinical strategies. *Nat Rev Cancer* **3**, 330-338.

Louvet C, Andre T, Artru P (2002) [Gemcitabine-based combinations in inoperable pancreatic cancers]. *Bulletin du cancer* **89 Spec No**, S96-101.

Luo WD, Anashkin E, Matthews CG (2010) Performance Evaluation of a PEM Scanner Using the NEMA NU 4-2008 Small Animal PET Standards. *Ieee Transactions on Nuclear Science* **57**, 94-103.

Magota K, Kubo N, Kuge Y *et al.* (2011) Performance characterization of the Inveon preclinical small-animal PET/SPECT/CT system for multimodality imaging. *European Journal of Nuclear Medicine and Molecular Imaging* **38**, 742-752.

Maitra A, Hruban RH (2008) Pancreatic cancer. In *Annual Review of Pathology-Mechanisms of Disease*, vol. 3, pp. 157-188. Palo Alto: Annual Reviews.

Mamon HJ, Killoran JH, Blake MA *et al.* (2009) Impact of F-18-Fluoro-3'-Deoxy-3'-L-Fluorothymidine (FLT) PET/CT on GTV Identification and Definition for Pancreatic Cancer. *Int J Radiat Oncol Biol Phys* **75**, S266-S266.

MediLumine (2016) Fenestra Optimal Usage Guide. Getting great results with Fenestra Nanoemulsions. <http://www.medilumine.com/application-notes-user-guides-product-brochures-poster-presentations/> (accessed 07-09-2016)

Michaud DS, Giovannucci E, Willett WC *et al.* (2001) Coffee and alcohol consumption and the risk of pancreatic cancer in two prospective United States cohorts. *Cancer Epidemiol Biomarkers Prev* **10**, 429-437.

Michl M, Haug AR, Jakobs TF *et al.* (2014) Radioembolization with Yttrium-90 microspheres (SIRT) in pancreatic cancer patients with liver metastases: efficacy, safety and prognostic factors. *Oncology* **86**, 24-32.

Moliner L, Gonzalez AJ, Soriano A *et al.* (2012) Design and evaluation of the MAMMI dedicated breast PET. *Med Phys* **39**, 5393-5404.

Morran DC, Wu J, Jamieson NB *et al.* (2014) Targeting mTOR dependency in pancreatic cancer. *Gut* **63**, 1481-1489.

Morton JP, Timpson P, Karim SA *et al.* (2010) Mutant p53 drives metastasis and overcomes growth arrest/senescence in pancreatic cancer. *Proceedings of the National Academy of Sciences of the United States of America* **107**, 246-251.

Mouse Sequencing Consortium (2010) Why Mouse Matters. Importance of Mouse Genome. <https://www.genome.gov/10001345/importance-of-mouse-genome/> (accessed 05-06-2016)

Moustakas A, Miyazawa K (2013) *TGF- β in Human Disease*: Springer Japan.

Muller I (2014) What is the value of "Out of date" review articles? Distortion of reality!: Mediso USA.

National Cancer Institute (2011) Chemotherapy Regimen Extends Survival in Advanced Pancreatic Cancer Patients. <http://www.cancer.gov/types/pancreatic/research/fofirinnox> (accessed 07-08-2016)

National Electrical Manufacturers Association (2008) NEMA Standards Publication NU4-2008. Performance Measurements of Small Animal Positron Emission Tomographs.: National Electrical Manufacturers Association.

National Electrical Manufacturers Association (2015) Medical Imaging Standards. <http://www.nema.org/Standards/Pages/All-Standards-by-Product.aspx?ProductId=6c490050-e74a-4366-bca5-f7e40fa714f6>

Neoptolemos JP, Stocken DD, Friess H *et al.* (2004) A randomized trial of chemoradiotherapy and chemotherapy after resection of pancreatic cancer. *New England Journal of Medicine* **350**, 1200-1210.

Neuzillet C, Tijeras-Raballand A, Cohen R *et al.* (2015) Targeting the TGF β pathway for cancer therapy. *Pharmacology & Therapeutics* **147**, 22-31.

Northern Ireland Cancer Registry (2015). <http://www.qub.ac.uk/research-centres/nicr/CancerInformation/> (accessed 12-12-2015)

Noto H, Tsujimoto T, Sasazuki T *et al.* (2011) Significantly Increased Risk of Cancer in Patients with Diabetes Mellitus: a Systematic Review and Meta-Analysis. *Endocr Pract* **17**, 616-628.

Office for National Statistics (2015). <http://www.ons.gov.uk/> (accessed 12-12-2015)

Pajak MZ, Volgyes D, Pimlott SL *et al.* (2016) NEMA NU4-2008 Performance Evaluation of Albira: A Two-Ring Small-Animal PET System Using Continuous LYSO Crystals. *Open Medicine Journal* **3**, 12-26.

Pancreatic Cancer UK (2014) Types of Pancreatic Cancer. *Facts About Pancreatic Cancer*. (accessed 27/08/2015)

Pancreatic Cancer UK (2015a) Irreversible electroporation (NanoKnife). <http://www.pancreaticcancer.org.uk/information-and-support/treatments-for-pancreatic-cancer/irreversible-electroporation-nanoknife/> (accessed 05-06-2016)

Pancreatic Cancer UK (2015b) Radiotherapy. <http://www.pancreaticcancer.org.uk/radiotherapy> (accessed 08-07-2016)

Parikh DA, Durbin-Johnson B, Urayama S (2014) Utility of serum CA19-9 levels in the diagnosis of pancreatic ductal adenocarcinoma in an endoscopic ultrasound referral population. *Journal of gastrointestinal cancer* **45**, 74-79.

Petersen GM, de Andrade M, Goggins M *et al.* (2006) Pancreatic cancer genetic epidemiology consortium. *Cancer Epidemiol Biomarkers Prev* **15**, 704-710.

Prasad R, Ay MR, Ratib O *et al.* (2011a) CT-Based Attenuation Correction on the FLEX Triumph Preclinical PET/CT Scanner. *IEEE Transactions on Nuclear Science* **58**, 66-75.

Prasad R, Ratib O, Zaidi H (2010) Performance Evaluation of the FLEX Triumph X-PET Scanner Using the National Electrical Manufacturers Association NU-4 Standards. *Journal of Nuclear Medicine* **51**, 1608-1615.

Prasad R, Ratib O, Zaidi H (2011b) NEMA NU-04-based performance characteristics of the LabPET-8TM small animal PET scanner. *Physics in Medicine and Biology* **56**, 6649-6664.

Principe DR, Doll JA, Bauer J *et al.* (2014) TGF-beta: Duality of Function Between Tumor Prevention and Carcinogenesis. *JNCI- Natl Cancer Inst* **106**.

Quon A, Chang ST, Chin F *et al.* (2008) Initial evaluation of F-18-fluorothymidine (FLT) PET/CT scanning for primary pancreatic cancer. *European Journal of Nuclear Medicine and Molecular Imaging* **35**, 527-531.

Rasband WS (1997-2016) ImageJ. Bethesda, Maryland, US: U. S. National Institutes of Health.

Ritchie ME, Phipson B, Wu D *et al.* (2015) limma powers differential expression analyses for RNA-sequencing and microarray studies. *Nucleic acids research* **43**, e47.

Rozengurt E, Soares HP, Sinnet-Smith J (2014) Suppression of feedback loops mediated by PI3K/mTOR induces multiple over-activation of compensatory pathways: an unintended consequence leading to drug resistance. *Mol Cancer Ther* **13**, 2477-2488.

Saha GB (2010) Performance Characteristics of PET Scanners. In *Basics of PET Imaging: Physics, Chemistry, and Regulations*, pp. 97-116. New York, NY: Springer New York.

Sanchez F, Moliner L, Correcher C *et al.* (2012) Small animal PET scanner based on monolithic LYSO crystals: Performance evaluation. *Med Phys* **39**, 643-653.

- Sanchez F, Orero A, Soriano A *et al.* (2013) ALBIRA: A small animal PET/SPECT/CT imaging system. *Med Phys* **40**.
- Schober O, Riemann B, SpringerLink (2013) *Molecular imaging in oncology*. vol. 187;187.;. Berlin;London;: Springer.
- Shields AF, Grierson JR, Dohmen BM *et al.* (1998) Imaging proliferation in vivo with F-18 FLT and positron emission tomography. *Nat Med* **4**, 1334-1336.
- Shreve PD (1998) Focal fluorine-18 fluorodeoxyglucose accumulation in inflammatory pancreatic disease. *European journal of nuclear medicine* **25**, 259-264.
- Simeone DM, Maitra A (2013) *Molecular Genetics of Pancreatic Cancer*. New York, NY: Springer New York.
- Smyth GK (2004) Linear models and empirical bayes methods for assessing differential expression in microarray experiments. *Statistical applications in genetics and molecular biology* **3**, Article3.
- Soriano A, Sanchez F, Carrilero V *et al.* (2013) Performance evaluation of the Dual Ring MAMMI breast PET. *2013 IEEE Nuclear Science Symposium and Medical Imaging Conference (Nss/Mic)*.
- Spinks TJ, Karia D, Leach MO *et al.* (2014) Quantitative PET and SPECT performance characteristics of the Albira Trimodal pre-clinical tomograph. *Physics in Medicine and Biology* **59**, 715.
- Suckow CE, Stout DB (2008) MicroCT liver contrast agent enhancement over time, dose, and mouse strain. *Molecular imaging and biology : MIB : the official publication of the Academy of Molecular Imaging* **10**, 114-120.
- Tanaka T, Sho M, Nishiofuku H *et al.* (2012) Unresectable pancreatic cancer: arterial embolization to achieve a single blood supply for intraarterial infusion of 5-fluorouracil and full-dose IV gemcitabine. *AJR American journal of roentgenology* **198**, 1445-1452.
- Ten Dijke PT, Goumans MJ, Itoh F *et al.* (2002) Regulation of cell proliferation by Smad proteins. *J Cell Physiol* **191**, 1-16.

Thielemans K, Mustafovic S, Tsoumpas C (2006) STIR: Software for Tomographic Image Reconstruction Release 2. In *2006 IEEE Nuclear Science Symposium Conference Record*, vol. 1-6, pp. 2174-2176. New York: IEEE.

Thorpe LM, Yuzugullu H, Zhao JJ (2015) PI3K in cancer: divergent roles of isoforms, modes of activation and therapeutic targeting. *Nat Rev Cancer* **15**, 7-24.

Visser EP, Disselhorst JA, Brom M *et al.* (2009) Spatial Resolution and Sensitivity of the Inveon Small-Animal PET Scanner. *Journal of Nuclear Medicine* **50**, 139-147.

Visser EP, Disselhorst JA, van Lier MGJTB *et al.* (2011) Characterization and optimization of image quality as a function of reconstruction algorithms and parameter settings in a Siemens Inveon small-animal PET scanner using the NEMA NU 4-2008 standards. *Nucl Instrum Methods* **629**, 357-367.

von Forstner C, Egberts JH, Ammerpohl O *et al.* (2008) Gene expression patterns and tumor uptake of F-18-FDG, F-18-FLT, and F-18-FEC in PET/MRI of an orthotopic mouse xenotransplantation model of pancreatic cancer. *Journal of Nuclear Medicine* **49**, 1362-1370.

Wathen CA, Foje N, van Avermaete T *et al.* (2013) In vivo X-Ray Computed Tomographic Imaging of Soft Tissue with Native, Intravenous, or Oral Contrast. *Sensors* **13**, 6957-6980.

Wei Q, Wang S, Ma T *et al.* (2015) Performance evaluation of a compact PET/SPECT/CT tri-modality system for small animal imaging applications. *Nuclear Instruments & Methods in Physics Research Section a-Accelerators Spectrometers Detectors and Associated Equipment* **786**, 147-154.

Welsh Cancer Intelligence and Surveillance Unit (2015).

<http://www.wcisu.wales.nhs.uk> (accessed 12-12-2015)

Whatcott CJ, Posner RG, Von Hoff DD *et al.* (2012) Desmoplasia and chemoresistance in pancreatic cancer. In *Pancreatic Cancer and Tumor Microenvironment* [PJ Grippo and HG Munshi, editors]. Trivandrum (India): Transworld Research Network

Transworld Research Network.

Willekens I, Buls N, Lahoutte T *et al.* (2010) Evaluation of the radiation dose in micro-CT with optimization of the scan protocol. *Contrast Media & Molecular Imaging* **5**, 201-207.

Yang YM, Tian XD, Zhuang Y *et al.* (2005) Risk factors of pancreatic leakage after pancreaticoduodenectomy. *World J Gastroenterol* **11**, 2456-2461.

Zhang PH, Chen ZW, Lv D *et al.* (2012) Increased risk of cancer in patients with type 2 diabetes mellitus: A retrospective cohort study in China. *BMC Public Health* **12**, 6.